Dissertation
submitted to the
Combined Faculties for the Natural Sciences and for Mathematics
of the Ruperto-Carola University of Heidelberg, Germany
for the degree of
Doctor of Natural Sciences

put forward by
Dipl.-Phys. Jana Schnieders
born in Bremerhaven

Date of oral exam: February, 6th 2015

Analyzing the footprints of turbulence producing mechanisms at the free water surface

Referees:

Priv.-Doz. Dr. Christoph S. Garbe

Prof. Dr. Kurt Roth

Abstract

At the free wind-sheared water surface, various turbulence producing mechanisms contribute significantly to enhanced transfer rates of heat and gas across the air-water boundary. As a result, surface convergence and divergence form and can be visualized in infrared images of the water surface. Within this work the footprints of turbulent processes in the surface temperature pattern are analyzed. Image processing techniques, such as motion estimation and classification, are adapted and applied to the infrared images of the water surface. Dense flow fields are estimated without the suppression of surface divergence and up- and down-welling sites are identified. Data from a range of laboratory facilities is evaluated with a focus on small spatial scales, low to moderate wind stress and the impact of surfactants on the surface dynamics. In this wind regime shear induced turbulence, small Langmuir circulations and microscale breaking waves are identified as the dominant processes that drive heat exchange. The turbulent cell size is suggested as a characteristic feature of shear and Langmuir turbulence and is related against friction velocity and wave field. Within this work, a novel method is suggested to assess the impact of individual processes on the overall heat transfer rate and tested on the measured laboratory data also with respect to the influence of increasing wind stress and surfactant coverage. The following key points are found: Shear induced turbulence is a major contributor to enhanced transfer rates at low wind stress. Its relevance increases if the surface is covered by surfactants as the onset of waves is delayed. Langmuir circulations play a major role at intermediate wind stress and cause a significant increase of transfer rates. Surfactants on the water surface delay the evolution of Langmuir circulation and intensity considerably. Microscale breaking is a dominant contributor at moderate wind stress and is responsible for approximately 50% and more of the transfer rate.

Zusammenfassung

Wind, der über eine freie Wasserfläche weht, verursacht eine Vielzahl miteinander wechselwirkender turbulenter Prozesse, die entscheidend dazu beitragen, dass sich der Austausch zwischen Wasser und Luft beschleunigt. Die enstandene Oberflächendivergenz und -konvergenz wird in Infrarotbildern sichtbar, bildet also die ursächlichen Prozesse ab. In dieser Arbeit werden die Temperaturmuster an der Wassermethode untersucht, mit Hilfe von Methoden aus der Bildverarbeitung wie Bewegungsschätzung aus optischem Fluss und der Klassifikation von Strukturen. Hierbei werden dichte Geschwindigkeitsfelder ermittelt, ohne vorhandene Divergenz zu dämpfen, weiterhin werden Auf- und Abtriebsgebiete detektiert. Daten aus verschiedenen Wind-Wellen-Kanälen werden ausgewertet, ein Schwerpunkt liegt auf niedrigen bis moderaten Windgeschwindigkeiten und dem Einfluss von oberflächenaktiven, filmbildenden Substanzen auf die Dynamik der Oberfläche. Unter diesen Bedingungen verursachen vor allem kohärente turbulente Strukturen durch Scherung der Wasseroberfläche, kleine Langmuir Zirkulationen und kleinskalig brechende Wellen erhöhte Austauschraten von Wärme oder Gasen. Die Größe turbulenter Zellen wird als allgemeines Kriterium vorgeschlagen, und charakterisiert besonders Scherturbulenz und Langmuir Zirkulationen relativ zu Schubspannungsgeschwindigkeit und Wellenfeld. In dieser Arbeit wird eine neue Methode vorgeschlagen, um den Einfluss einzelner turbulenter Prozesse auf die gesamte Wärmeaustauschrate zu quantifizieren in Abhängigkeit von Windgeschwindigkeit und Oberflächenfilm. Folgende Schlüsselerkenntnisse wurden festgestellt: Bei niedrigen Windgeschwindigkeiten ist Scherturbulenz hauptursächlich für beschleunigten Wär-metransfer, bei steigendem Wind und der Entstehung von Wellen sind es Langmuir Zirkulationen, die die Transferrate beträchtlich erhöhen. Ein Oberflächenfilm verzögert die Entstehung von Wellen und damit auch diejenige von Langmuir Zirkulationen. Deshalb nimmt in diesem Fall die Bedeutung von Schertubulenz für die Austauschrate zu, während Langmuir Zirkulationen gedämpft werden. Bei steigendem Wind dominieren kleinskalig brechende Wellen und tragen 50% und mehr zur Wärmeaustauschrate bei.

Contents

1. Introduction

"The atmospheric concentrations of carbon dioxide, methane, and nitrous oxide have increased to levels unprecedented in at least the last 800,000 years. Carbon dioxide concentrations have increased by 40% since pre-industrial times, primarily from fossil fuel emissions and secondarily from net land use change emissions. The ocean has absorbed about 30% of the emitted anthropogenic carbon dioxide, causing ocean acidification", [IPCC, 2013].

Within the last century the world's climate has been undergoing continuous change driven by the accumulation of greenhouse gases in the atmosphere. Carbon dioxide is one of the most extensively studied examples of a greenhouse gas and major contributor to raising temperatures. The total concentrations of climatically active gases is to a large extend determined by sinks and sources on land and ocean. As 70 % of the earth's surface are covered by ocean the transfer of mass and energy across the ocean atmosphere interface plays a crucial role in our climate system and determines the uptake of greenhouse gases and heat.

The estimated 30% of atmospheric carbon dioxide absorbed in the ocean determine the future climate evolution [Cox et al., 2000]. Consequently, the ocean is a major sink for emitted anthropogenic carbon dioxide [Le Quéré et al., 2014]. While this slows the greenhouse effect considerably and thereby global warming, it also leads to ocean acidification, which is a major threat to sea organisms depending on carbonate shells such as corals [Feely et al., 2004; Orr et al., 2005].

At the same time, this amount of absorbed carbon dioxide is a global average and subject to large spatial and inter-annual variations. The total flux from atmosphere to ocean depends strongly on the efficiency of the transfer process through the boundary layer, which is determined by the transfer velocity or transfer rate. Multiplied with the concentration gradient it gives the total flux. Therefore, coupled climate models aiming to predict the uptake of atmospheric carbon by the ocean, e.g., [Cox et al., 2000], depend on an accurate parameterization of gas transfer velocities [Garbe et al., 2014].

Within the field of air-sea interaction the optimal parameterization of exchange processes has been subject to extensive investigation for the past decades [Frew et al., 2004; Ho et al., 2011; Liss and Slater, 1974; Wanninkhof, 1992]. However, a good parameterization can only be based on the thorough understanding of the physical processes at the water surface causing the high variability of observed transfer velocities.

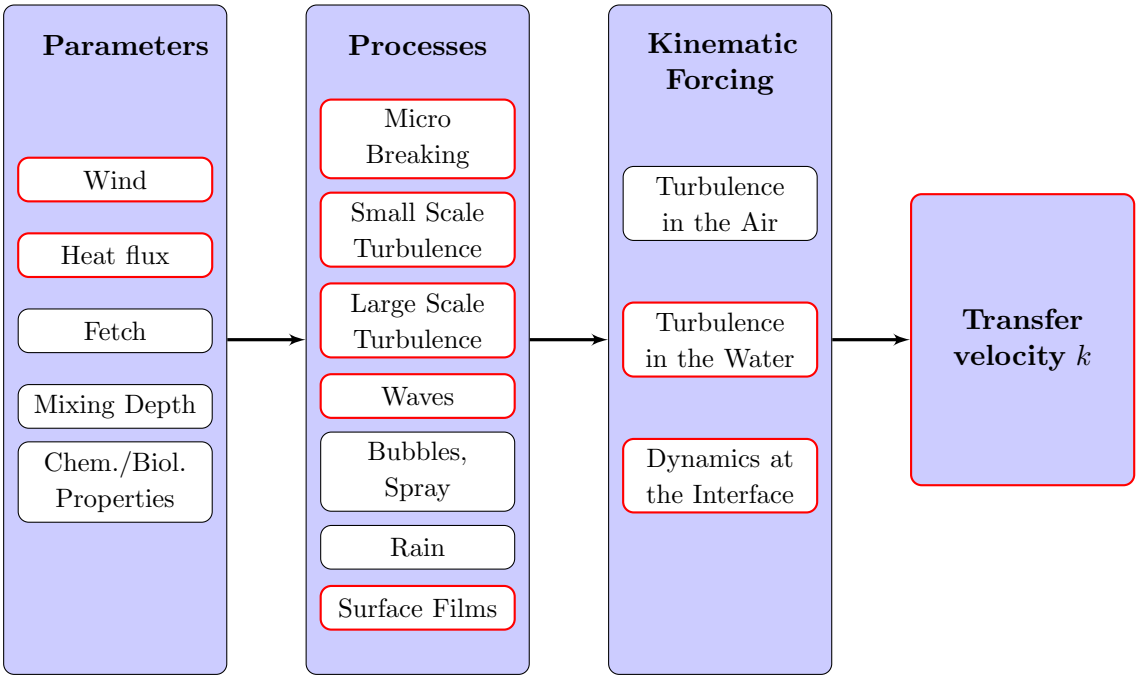

Figure 1.1.: Overview of parameters and processes influencing gas transfer, adapted from Garbe et al. [2014]. Various parameters such as wind or heat flux determine the evolution of connected processes, e.g., microscale breaking and turbulence on different scales. These turbulence producing processes in turn determine the dynamics at the interface and thus the transfer velocity, k. Red boxes indicate parameters and processes under investigation and discussion in this work.

Processes affecting air-sea interaction

Ultimately, the transfer velocity is determined by the fluid dynamics close to the water surface. Within a very thin layer at the surface, the mass boundary layer, the transfer process is governed by molecular diffusion. Below that, it is turbulent mixing that efficiently transfers water parcels from the bulk into the mass boundary layer and enhances transfer velocities [Soloviev and Schlüssel, 1994].

Figure 1.1 shows an overview of parameters and processes which influence gas transfer. Red boxes indicate parameters and processes under investigation in this work. Initially, all fluid flow in the upper ocean originates from the input of momentum through wind stress on the water surface. Further parameters include biological activity, heat flux and fetch, which describes the length on the water surface over which the wind has blown. Even though wind stress is the main source of momentum input into the water, turbulence producing processes such as shear stress, waves and resulting small and large scale turbulent structures are responsible for the kinematic forcing that finally leads to enhanced transfer rates. Along with thermodynamic forcing, this determines the total air-sea flux of sparingly soluble gases like CO_2.

As our climate system undergoes a continuous change, it becomes increasingly important to identify the driving forces of enhanced transfer velocities. A shift in the wind speed distribution has already led to reduced CO_2 uptake in the southern ocean [Le Quéré et al., 2007].

The frequency distribution of wind speeds over the ocean exhibits a peak at a relatively low wind speed of approximately $U_{10} = 5$ m/s [Wanninkhof, 1992]. However, weighted with their relevance to exchange processes, the peak of the distribution shifts to higher wind speeds. Highest influence on air-sea interaction is found at wind speeds of approximately 10 m/s [Wanninkhof, 1992]. Accordingly, a significant fraction of the global exchange of heat and gas across the air-sea interface is determined by wind speeds in the range $5 - 10$ m/s.

Key coupling processes at low to moderate wind stress are shear induced turbulence, waves, especially microscale breaking, as well as wave-shear coupled turbulence, e.g., Langmuir circulation. All these processes act on relatively small scales. Their common characteristic is the injection of turbulent kinetic energy close to the water surface. Exchange rates are closely linked to the intensity of near-surface turbulence [McKenna and McGillis, 2004]. Thus, CO_2 fluxes show stronger variability on smaller scales than climatology can directly predict [Wanninkhof et al., 2011].

Linking measured transfer rates, k, with a parameter such as wind speed, U, allows for a parameterization of gas exchange and, therefore, the prediction of transfer rates in dependency of the chosen parameter. Wind speed seems like an obvious choice as measurements are widely available and easy to obtain. Ho et al. [2011] found the parameterization with wind speed to correlate well with observational data measured within the duration of weeks. However, there is a large uncertainty within the k-U parameterization. Gas transfer rates measured at the same wind stress vary by a factor of two. This holds true especially in oceanic areas with surface active material on the water surface, i.e. caused by high biological activity in coastal areas. Surfactants form a thin, mono-molecular layer at the water surface and thereby reduce surface roughness. Transfer rates in affected areas are considerably lower than expected from the U_{10} parameterization, considering the prevailing wind stress [Frew et al., 2004].

Properties such as kinetic energy dissipation or surface divergence describe the dynamic state of the water surface much more closely than wind speed and have been successfully linked to transfer velocities (e.g., most recently [Banerjee et al., 2004; Zappa et al., 2007]). As these properties require in-situ measurements of the subsurface velocity field a universal parameterization based on these quantities is often not a viable option. Other parameterizations have been suggested, based on a statistical property of the wave field, the mean square slope (MSS), [Jähne et al., 1984] and provide good results [Frew et al., 2004; Krall, 2013]. This is due to two important processes: Langmuir circulation [Veron and Melville, 2001] and microscale breaking [Zappa et al., 2004]. Both are to a certain degree characterized by increasing MSS values. However, Kiefhaber [2014] pointed out that MSS provides generally a good parameterization, at low wind speeds and surfactants, however, its reliability decreases.

From a mechanistic point of view, neither a parameterization based solely on wind speed nor one based on wave properties, can explain the variation of transfer velocities exhaustively. Processes like shear turbulence depend strongly on wind stress. Microscale breaking is well described by mean square slope. Langmuir circulation, on the other hand, result from the

coupling of wind and waves. At identical wind stress surfactants can alter the wave field and therefore related surface processes considerably.

Scope of this work

In the scope of this thesis, processes enhancing air-sea transfer rates will be investigated with respect to their characteristic features and impact on exchange. A focus will be on low to moderate wind speeds because this is the range of wind speeds that occurs most frequently on the global ocean [Wanninkhof, 1992] and a considerable fraction of the global exchange of heat and gas is determined by moderate wind speeds. Another key aspect is the impact of surface active materials reducing surface roughness on near surface turbulence, a state that occurs frequently on the ocean [Wurl and Obbard, 2004]. None of the commonly employed parameterizations is able to explain varying gas transfer rates in these conditions exhaustively. The goals of this work are threefold:

1. Identification of dominant turbulent regimes depending on wind speed and surface conditions.

2. Definition of the characteristic features of these processes.

3. Assessment of the impact of individual processes on air-sea transfer under varying surface conditions.

The results help to explain why a parameterization is accurate under certain conditions only. To achieve these goals, new methods for the analysis of the interacting turbulent mechanism are developed and tested on the collected measurement data.

Thermographic techniques are ideal for surface measurements of interfacial turbulence [Garbe et al., 2004; Handler et al., 2001; Haussecker et al., 1995, 2002; Jessup et al., 1997; Schimpf et al., 1999b; Zappa et al., 2001]. Application of techniques from image processing such as motion estimation and classification of the surface heat pattern provide detailed information about the dynamic state of the water surface with a high spatial and temporal resolution provided by state-of-the-art infrared cameras [Schnieders et al., 2013]. The data is collected in the laboratory to be able to precisely adjust surface conditions. The controlled environment of the laboratory allows for a range of different wind wave conditions and the addition of surface active material. In principle, the same technique could be applied to the field.

Structure of this thesis

- In Chapters 2 and 3, a review of the fluid dynamics of the free wind sheared water surface is given with a focus on processes relevant to air-sea gas exchange. An overview of existing conceptual models of near surface turbulence presents current formulations of the gas transfer rate based on parameters describing turbulence.

- An overview of the experiments, from which data was analyzed in this thesis, is given in Chapter 4. Here, the experiments described in Section 4.1 were conducted within this work while the data from the experiments described in Sections 4.3 and 4.2 were kindly provided within a collaboration between Bill Peirson from the water research laboratory in Sydney, Cristopher Zappa from the Lamont-Doherty Institute, New York and Geoffrey Smith from the Rosenstiel School of Atmospheric and Ocean Sciences, Miami.

- In Chapters 5 and 6, techniques for the analysis of passive infrared images of the water surface are introduced. In Chapter 5 state-of-the-art global optic flow techniques are presented and subsequently, adapted for the analysis of the data in this thesis. A comparison of results from optical flow with results from active Thermography provides a means to determine errors of the velocity estimation. In Chapter 6 the classification procedure of the surface temperature pattern is described. This has in parts already been published in Schnieders et al. [2013].

- In Chapter 7, the dominant turbulent regimes are defined depending on wind speed and surface condition. Processes defining the dynamics of the water surface are discussed with respect to their impact on the surface velocity fields and their appearance in the infrared images.

- Chapter 8 is in large parts based on Schnieders et al. [2013]. Preliminary results have also been published in Schnieders [2011] and were extended and adapted. In this chapter the turbulent cell size is defined as a universal criterion to identify shear induced turbulence at a range of wind speeds and tests the spacing of observed wave-shear coupled turbulence against neutral stability theory applicable to Langmuir circulations.

- Chapters 9 and 10 derive the impact of shear induced turbulence and Langmuir circulations on heat exchange rates. First, an adaptation of the eddy renewal model is presented, which includes a concept of eddy superposition and a more robust approach to the estimation of heat transfer rates based on classified surface eddies. The result of this Chapter is the identification of a transition wind stress regime in which Langmuir circulations are responsible for a large fraction of total heat transfer.

- Finally, Chapters 11 and 12 summarize and discuss the results of the previous sections. An outlook is given, including planned experiments with an octocopter in cooperation with SeaNetworks e.V. at the Alfred-Wegener-Institute for Polar- and Marine Research.

2. Turbulent processes at the free water surface

2.1. Overview of relevant turbulent processes in the context of air-sea interaction

Turbulence is ubiquitous in every open water body on earth, from the small pond to the world's oceans. Turbulent motion occurs on a wide range of scales from global ocean circulation to microscopic dissipative eddies. One characteristic of turbulence is the transfer of momentum, heat and mass [Thorpe, 2007], either between scales or between different parts of the water body.

In the context of air-sea interaction especially those turbulent processes are of interest which facilitate the transfer of heat, energy and momentum between air and water, i.e. near surface aqueous turbulence. Figure 1.1 shows an overview of parameters and processes influencing gas transfer between atmosphere and ocean, adapted from Garbe et al. [2014]. An illustration of these processes can be found in Figure 2.1. Here, tubulence generating processes, e.g., wind and waves, are given in yellow, while turbulence suppressing processes, e.g. surfactants, are shown in orange. Various parameters such as wind or heat flux determine the evolution of several processes, e.g., microscale breaking and turbulence on different scales. These turbulence producing processes in turn determine the dynamics of the interface and thus the transfer velocity, k.

In this work, a focus will be on processes that evolve under low to moderate wind stress on relatively small scales and are indicated by red boxes in Figure 1.1. Shear induced turbulence, small Langmuir circulation and microscale breaking are the defining processes at low to moderate wind stress. Macroscale breaking, while exhibiting prominent white caps, injects turbulent kinetic energy to deep to cause more significant surface renewal and contributes mainly through the generation of bubble plumes. This process, though significant at higher wind speeds, does not play a major role at low to moderate wind stress. At low to moderate wind speeds the alteration of surfactants to the turbulent regimes of the water surface is most pronounced. It has been pointed out that soluble surfactants have the biggest effect by altering hydrodynamical properties of the water surface [Garbe et al., 2014; Liss, 1983]. The big challenge is the quantification of these processes in a way that allows for the prediction of transfer rates based on the physical understanding of surface dynamics.

The main generation mechanism of small scale turbulence at the water surface is wind stress [Asher, 1997; Kitaigorodskii, 1984]. Numerical simulations [Tsai et al., 2005] and laboratory studies [Rashidi and Banerjee, 1990] have shown that wind stress alone without surface waves is sufficient for coherent turbulent structures to evolve. Small scale surface turbulence is ubiquitous

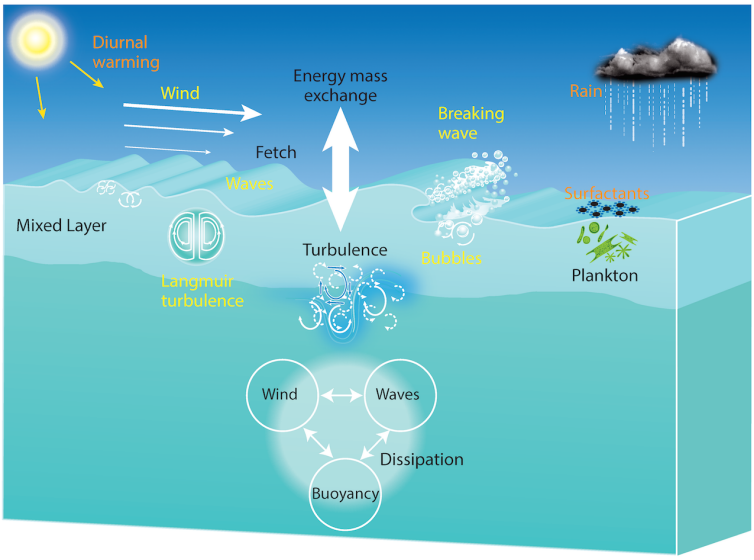

Figure 2.1.: Illustration of parameters and processes influencing the exchange of energy and mass from SOLAS Scientific Steering Committee [2015]. Tubulence generating processes, e.g., wind and waves, are given in yellow, while turbulence suppressing processes, e.g. surfactants, are shown in orange.

on all open water bodies but size and intensity strongly depend on environmental conditions. Therefore, shear induced turbulence is an important mechanism for controlling transfer rates at the air-sea interface [Asher, 1997; Salter et al., 2011; Wanninkhof et al., 2009].

In the presence of small gravity waves the characteristic temperature pattern at the water surface exhibits cold streaks with larger spacings and longer life time than shear induced turbulence [Caulliez, 1998; Melville et al., 1998; Schnieders et al., 2013; Veron and Melville, 2001]. Their characteristics have been shown to correspond very well with Langmuir circulation as described by Craik-Leibovich (CL) II mechanism [Leibovich and Paolucci, 1981]. Langmuir circulations are generally known as larger scale roll vortices that can be observed on the open ocean causing lines of foam in wind direction. On a smaller scale they have been observed in the field and laboratory [Caulliez, 1998; Melville et al., 1998; Veron and Melville, 2001] as soon as the first wind waves form at the water surface.

Microscale breaking [Banner and Phillips, 1974] denotes the breaking of small gravity waves in the process of which high levels of turbulent kinetic energies are reached in the spilling region of the wave [Jessup et al., 1997]. Microscale breaking waves have been shown to contribute significantly to enhanced transfer velocities at moderate wind speeds (up to 70% according to [Zappa et al., 2001] and 50 % to [Peirson et al., 2014]).

2.2. Observation of turbulent processes

In a turbulent flow the largest eddies have a characteristic scale and appear as coherent turbulence. In the study of exchange between ocean and atmosphere those eddies are of high interest because from their size and intensity information can be gained about the turbulent state of the

water surface. Near surface turbulence leads to upwelling of deeper water to the surface and is a main driver of surface divergence. Due to the cool skin of the ocean, heat can be used as a tracer to detect areas of surface convergence and divergence and thus gather information about size and intensity of a turbulent process.

The cool skin at the water surface develops if there is a negative heat flux between water and air. There are three main passage ways for the exchange of heat across the air-water interface: Latent heat flux because of the enthalpy of evaporation, sensible heat flux as a result of the first law of thermodynamics, and radiative heat flux according to Planck's Law.

$$j_{\text{tot}} = j_{\text{latent}} + j_{\text{sensible}} + j_{\text{radiative}} \tag{2.1}$$

The sensible heat flux is determined by the temperature difference of air and water. The latent heat flux is the result of the evaporation of water molecules which thus change their aggregate state leading to a cooling of the water surface because of the loss of evaporation heat. The latent heat flux depends on the saturation deficit of the air directly above the water which itself is determined by the humidity of the air and for example the wind speed. The exchange of heat between the ocean and the atmosphere leads to the development of a thin surface layer that is colder than the bulk water below.

2.2.1. The footprints of turbulence in infrared images

Velocities at the water surface are determined by underlying turbulence which causes horizontal and vertical velocity gradients. For an incompressible Newtonian Fluid (refer to Section 2.3.1), the continuity equation Equation 2.6 yields

$$-\left.\frac{\partial w}{\partial z}\right|_{z=0} = \left.\frac{\partial u}{\partial x}\right|_{z=0} + \left.\frac{\partial v}{\partial y}\right|_{z=0}, \tag{2.2}$$

with u and v being horizontal velocity components and w the vertical velocity component. As a consequence, small fluctuations in the vertical velocity component are caused by waves and coherent turbulent structures and induce horizontal velocities at the water surface. Zones of surface divergence and convergence evolve and disturb the cool skin of the water and lead to the development of a heat pattern on the water surface that visualizes the process that causes it.

The surface heat pattern thus exhibits footprints of the underlying turbulence which are characteristic of the turbulence generating processes involved. This means that taking infrared images of the water surface provides an ideal technique to observe surface turbulence. Especially since infrared cameras with high spatial and temporal resolution have become available, Thermography has been shown a valuable tool in the study of turbulent processes at the water surface [Handler et al., 2001; Haussecker et al., 1995, 2002; Jessup et al., 1997; Schimpf et al., 1999b; Zappa et al., 2001]. Garbe et al. [2002, 2004] and Schimpf et al. [2004] have presented techniques based on passive thermography to estimate the heat flux and relate the scale of sur-

face renewal events to wind speed and heat exchange. Thermographic techniques have also been used to investigate the features of near surface turbulence by [Handler et al., 2001, 2012; Handler and Smith, 2011; Melville et al., 1998; Scott et al., 2008; Veron and Melville, 2001; Veron et al., 2011].

Due to the high temporal resolution of infrared cameras not only the spatial features can be examined but also the dynamics of the water surface temperature pattern are captured and therefore also the time scales on which a process acts. In Figure 7.1 an example image is shown with annotations to illustrate the footprints of shear turbulence and small Langmuir circulations.

In the following sections the relevant turbulence producing mechanism will be discussed.

2.3. The free water surface

2.3.1. Conservation of mass and momentum

Continuity equation

The continuity equation in fluid mechanics expresses the principle of conservation of mass for fluids, i.e. changes in density of a fluid parcel of a certain volume must be caused by a flow of fluid into this volume. The continuity equation is given by

$$\frac{\partial \rho}{\partial t} + \nabla \cdot (\rho \mathbf{u}) = 0 \tag{2.3}$$

The divergence term can be rewritten [Kundu, 2008] as

$$\frac{\partial}{\partial x}(\rho u_i) = \rho \frac{\partial u_i}{\partial x_i} + u_i \frac{\partial \rho}{\partial x_i} \tag{2.4}$$

The continuity equation then becomes

$$\frac{1}{\rho}\frac{D\rho}{Dt} + \nabla \cdot \mathbf{u} = 0 \tag{2.5}$$

Here, $D\rho/Dt = \partial\rho/\partial t + (\mathbf{u} \cdot \nabla)$ is the material derivative of the density and represents the rate of change of density following a fluid particle on its path. Density changes in a fluid typically occur due to changes in pressure, temperature or salinity (for example in the ocean). Water is, like most fluids, nearly incompressible, i.e. its density does not change with pressure (or much less than the spatial variation of velocities). Together with the assumption of other constant properties as e.g. viscosity this is called the Boussinesq equation that holds for many applications involving fluids and certainly if considering the water surface on relatively small scales. This means that $D\rho/Dt = 0$ and the continuity equation simplifies to

$$\nabla \cdot \mathbf{u} = 0. \tag{2.6}$$

Navier-Stokes equation

The Navier-Stokes equations represent the conservation of Momentum required by Newtons Second Law:

$$\int \left[\rho \frac{Du_i}{Dt} - \rho g_i - \frac{\partial \tau_{ij}}{\partial x_j} \right] dV = 0 \tag{2.7}$$

Any acceleration and thus change of momentum is the result of body forces acting on the fluid. This holds for any volume V and therefore, the integrand in Equation 2.7 must vanish at every point [Kundu, 2008]. Here, ρg_i represents the body force per unit volume. The tensor τ_{ij} is the stress tensor and is given by

$$\tau_{ij} = -p\delta_{ij} + 2\mu e_{ij} \tag{2.8}$$

for incompressible fluids with $\nabla \cdot \mathbf{u} = 0$.

$$e_{ij} = \frac{1}{2} \left(\frac{\partial u_i}{\partial x_j} + \frac{\partial u_j}{\partial x_i} \right) \tag{2.9}$$

is the strain rate tensor. Here, it is assumed that the viscosity μ can only depend on the local thermodynamic state and is constant. This corresponds to Newtons definition of viscosity. Fluids obeying Equation 2.8 are thus called Newtonian fluid. Inserting Equation 2.8 into Equation 2.7 and switching to vector notation gives the Navier-Stokes equation for incompressible fluid:

$$\rho \frac{D\mathbf{u}}{Dt} = -\nabla p + \rho \mathbf{g} + \mu \nabla^2 \mathbf{u} \tag{2.10}$$

If the material derivative $D\mathbf{u}/Dt = \partial \mathbf{u}/\partial t + (\mathbf{u} \cdot \nabla)\mathbf{u}$ is expanded it becomes evident that the Navier-Stokes equation is quadratic in $\mathbf{u}$ and therefore a non-linear differential equation which means that analytic solutions only exist for very simple cases.

2.3.2. Description of turbulent flow

Reynolds number

The Navier-Stokes equation (Equation 2.10) also describes the balance between inertia forces, pressure and viscosity. The relationship between inertia and frictional force can be taken as a measure for turbulence in the flow and is represented by the Reynolds number. By scaling the velocity $\mathbf{u}$ in Equation 2.10 by the free-stream velocity U and distances by a representative length L, the Reynolds number can be derived via

$$Re = \frac{\text{Inertia force}}{\text{Viscous force}} = \frac{\rho U^2/L}{\mu U/L^2} = \frac{UL}{\nu} \tag{2.11}$$

with the kinematic viscosity $\nu = \mu/\rho$. Introducing non-dimesional variables $\mathbf{x}' = \mathbf{x}/L$, $\mathbf{u}' = \mathbf{u}/U$, $p' = (p - p_{\text{inf}})/(\rho U^2)$ the Navier-Stokes equation can be written as

$$\mathbf{u}' \cdot \nabla \mathbf{u}' = -\nabla p' + \frac{1}{Re} \nabla^2 \mathbf{u}'. \tag{2.12}$$

For high Reynolds numbers $1/Re$ becomes small and can be set to zero as a first approximation which results in the inviscid Euler equation. However, even at high Reynolds numbers, the viscous term cannot be neglected in boundary layers as viscosity determines the velocity gradient in the shear layer.

(Surface) Richardson number

In analogy to the Reynolds number, the Froude number describes the relation between Inertia forces and gravity forces, which is important when considering, for example, flow in an open channel or equally important when dealing with density-stratified fluids. In a density-stratified fluid the so called internal Froude number describes the relation of inertia and buoyancy force. However, in that case it is more common to define another non-dimensional number, the Richardson number [Kundu, 2008]

$$Ri = \frac{1}{Fr'^2} = \frac{(\rho_2 - \rho_1) g}{\rho_1 U^2 / L}^{1/2} = \frac{g' L}{U^2} \tag{2.13}$$

where $g' = g(\rho_2 - \rho_1)/\rho_1$ is the reduced gravity between the two layers of fluid with different densities.

At the free water surface a negative heat flux due to evaporation leads to free convection. The surface Richardson number describes the transition from convective instability to wind induced instability [Kudryavtsev and Soloviev, 1981; Soloviev and Schlüssel, 1994] and is given by

$$Rf_0 = -\alpha \; g \; q_0 \; \frac{\nu}{u^{*4}} \tag{2.14}$$

and holds within the surface shear layer. α is the coefficient of thermal expansion of water, $q_0 = -Q_0/(c_p \; \rho)$ and Q_0 is the total heat flux just below the sea surface, and u^* the friction velocity.

Estimates of a critical value of Rf_0 have been made by Kudryavtsev and Soloviev [1981] on the basis of the data on the cool skin of the ocean by Grassl [1976] and gave $Rf_{cr} = -1.5 \; 10^{-4}$. This means that based on this analysis the flow can be assumed to be mainly shear driven if $Rf_0 < Rf_{cr}$.

Reynolds averaged Navier-Stokes equations

At high Reynolds numbers, the flow is turbulent. Characteristic for turbulence is the development of eddies of a characteristic length scale which break subsequently down into smaller eddies and continue to do so until the minimum eddy size, the Kolmogorov scale [Kolmogorov, 1941],

is reached. The Navier-Stokes equation describes turbulent flow accurately but it is virtually impossible to solve a flow problem completely on all scales, including all velocity fluctuations.

Average quantities such as mean temperature or mean velocities can still be estimated without a tremendous effort. The so-called Reynolds decomposition treats every variable as a decomposition of a mean part and the deviation from the mean:

$$\tilde{u_i} = \overline{u}_i + u_i' \tag{2.15}$$

$$\tilde{p} = \overline{p} + p' \tag{2.16}$$

Mean quantities are indicated by an over line and fluctuating quantities by the dash, the mean of the fluctuating part is always zero, $\overline{u_i'} = 0$.

Inserting the Reynolds decomposition into the Navier-Stokes equations (Equation 2.10) and averaging over each term gives the Reynolds averaged Navier-Stokes equations:

$$\frac{\partial u_i}{\partial t} + u_j \frac{\partial u_i}{\partial x_j} = \frac{1}{\rho}\frac{\partial \overline{\tau}_{ij}}{\partial x_j} - \frac{g}{\rho}\overline{\rho}\delta_{i3} \tag{2.17}$$

where the stress is given by

$$\overline{\tau}_{ij} = \underbrace{-\overline{p}\delta_{ij} + \mu\left(\frac{\partial \overline{u_i}}{\partial x_j} + \frac{\partial \overline{u_j}}{\partial x_i}\right)}_{\tau_{ij}} \underbrace{- \rho\overline{u_i' u_j'}}_{\tau_{ij}'} \tag{2.18}$$

Comparing the Reynolds averaged Navier-Stokes equations with the original Navier-Stokes equations (2.10) it becomes evident that an additional term $\rho\overline{u_i' u_j'}$ appears in the stress tensor if the flow is turbulent. $\rho\overline{u_i' u_j'}$ is called Reynolds stress, represented by τ_{ij}', and is by orders of magnitude higher than viscous stress. Reynolds stress is of the order of $\rho\ l\ (\partial u/\partial y)^2$ where l is the mixing length [Prandtl, 1990]. In analogy to the viscous term a turbulent diffusivity can be introduced [Roedel, 2000]

$$\tau_{ij} = -\rho(\nu + \nu_e)\frac{\partial u_j}{\partial x_i} \tag{2.19}$$

in which the additional contribution of viscosity due to turbulence is represented by the eddy viscosity ν_e. From the Reynolds averaged momentum equation an equation for the kinetic energy of the average flow field can be derived [Kundu, 2008].

$$\underbrace{\frac{\partial \overline{E}}{\partial t} + \overline{u}_i \frac{\partial \overline{E}}{\partial x_j}}_{\substack{\text{Time rate of change} \\ \text{of } \overline{E} \text{ following} \\ \text{the mean flow}}} = \underbrace{\frac{\partial}{\partial x_j}\left(-\frac{\overline{u}_j\ \overline{p}}{\rho} + 2\nu\overline{u}_i\overline{E}_{ij} - \overline{u_i u_j}\ \overline{u}_i\right)}_{\text{transport}} \underbrace{- 2\nu\overline{E}_{ij}\ \overline{E}_{ij}}_{\substack{\text{viscous} \\ \text{dissipation}}} + \underbrace{\overline{u_i' u_j'}\frac{\partial \overline{u}_i}{\partial x_j}}_{\substack{\text{loss to} \\ \text{turbulence}}} - \underbrace{\frac{g}{\rho}\overline{\rho}\ \overline{u}_3}_{\substack{\text{loss to} \\ \text{potential energy}}} \tag{2.20}$$

with the mean strain rate $E_{ij} = 1/2\ (\partial \overline{u}_i/\partial x_j + \partial \overline{u}_j/\partial x_i)$. The interesting part here is the "loss to turbulence" term, which can also be seen as turbulence production term, $-\overline{u_i' u_j' \frac{\partial \overline{u}_i}{\partial x_j}}$. It

depends on the Reynold stress $\overline{u_i u_j}$ and the mean flow gradient $\frac{\partial \overline{u_i}}{\partial x_j}$. The fact that it is only affected by the symmetric part of the velocity-gradient tensor means that shear stress directly causes turbulence. Furthermore, turbulence production is only affected by the anisotropic part of the Reynolds stress tensor which means that only the departure from isotropy affects the production of turbulence.

2.4. Shear induced turbulence

2.4.1. Shear stress

When the wind starts blowing over a body of water, momentum is transported across the air-water interface via two observable processes: The development of a surface drift current and the onset of waves.

At the onset of wind over a smooth water surface the entire wind stress is transformed into tangential stress on the water surface and an upper shear layer develops. This layer reaches from the water surface to the depth in which the vertical velocity gradient becomes zero ($\partial u/\partial z \approx 0$) [Caulliez et al., 2007]. In the Navier-Stokes equation (2.10) the stress is represented by the expression

$$\tau_{ij} = -p\delta_{ij} + 2\mu e_{ij} \tag{2.21}$$

for the stress tensor with the strain rate:

$$e_{ij} = \frac{1}{2}\left(\frac{\partial u_i}{\partial x_j} + \frac{\partial u_j}{\partial x_i}\right). \tag{2.22}$$

The non-diagonal elements of Equation 2.21 relate the shear stress to the strain rate. The vertical momentum transport at the water surface due to wind stress blowing in one direction can be described by the entry of the tangential stress tensor τ_{xz}

$$\tau_{xz} = \mu \cdot \frac{\partial u_x}{\partial z} = \rho {u^*}^2, \tag{2.23}$$

where ρ is the density of water, μ the viscosity and $\partial u_x/\partial z$ is the velocity gradient in the surface layer. To characterize the shear stress, the so called friction velocity u^* is defined as $u^* = \sqrt{\tau_t/\rho}$, with τ_t being the tangential stress in wind direction. Based on these quantities a non-dimensional wall coordinate can be defined:

$$l^+ = \frac{l u^*}{\nu} \tag{2.24}$$

where l is the distance to the water surface and ν the kinematic viscosity. If the flow is turbulent, three regimes can be identified: the viscous shear layer, the logarithmic sublayer, and the outer layer. Very close to the water surface flow is determined by viscous forces. The layer in which the velocity decreases linearly is called the viscous sublayer. The thickness of this layer scales

with the kinematic viscosity ν.

With increasing wind stress the first surface waves appear and distort the water surface. As a result part of the wind stress is transformed into wave form drag (τ_{form}) enhancing the growth of the waves ($\tau = \tau_{\text{tang}} + \tau_{\text{form}}$). Banner and Peirson [1998] found that with increasing wind speed this fraction is growing while the fraction of the tangential component is even slightly decreasing.

2.4.2. Features of shear induced turbulence

From the Reynolds averaged equation for turbulent kinetic energy (Equation 2.20) we have learned that shear stress is the prime turbulence producing mechanism. This means that the main generation mechanism of small scale turbulence at the water surface is wind stress [Asher, 1997; Kitaigorodskii, 1984]. Numerical simulations [Tsai et al., 2005] and laboratory studies [Rashidi and Banerjee, 1990] have shown that wind stress alone without surface waves is sufficient for coherent turbulent structures to evolve.

Small scale surface turbulence is ubiquitous on all open water bodies but size and intensity strongly depend on environmental conditions. Therefore, shear induced turbulence is an important mechanism for controlling transfer rates at the air-sea interface [Asher, 1997; Salter et al., 2011; Wanninkhof et al., 2009].

Shear turbulence causes small scale surface convergence and divergence. As a result, the typical small scale heat pattern at the water surface consists of narrow cool bands and resembles fish scales [Handler et al., 2001]. It has been observed and described in infrared imagery by Handler et al. [2001, 2012]; Handler and Smith [2011]; Scott et al. [2008] and numerical simulations by Handler et al. [2001]; Tsai et al. [2005] but its exact nature has so far not been shown, though, a good deal is known about the universally observed fish scales.

The streaky pattern observed at the water surface is very similar to the pattern of low speed streaks near no-slip walls as described by Nakagawa and Nezu [1981] and Smith and Metzler [1983] and it has been suggested [Tsai et al., 2005] that low speed streaks near a no-slip wall and high speed streaks near the water surface originate from the same mechanism. Their spacing was found to be log-normally distributed with a mean dimensionless streak spacing of $l^+ = lu^*/\nu = 100$, where the mean streak spacing is given by l, the (water sided) friction velocity by u^* and the kinematic viscosity by ν. The factor u^*/ν by which l is non-dimensionalized is estimated to correspond to the thickness of the thermal boundary layer [Grassl, 1976].

The generally agreed scaling of $l^+ = lu^*/\nu = 100$ leads to the scaling of the streak spacing with the friction velocity u^*. Therefore, if the forcing mechanism is the same as that forcing the water surface, spacing of the streaks is supposed to decrease with increasing u^* in the regime of low wind speeds [Scott et al., 2008].

Another possible production process is that of convective cells elongated by shear stress. Soloviev and Schlüssel [1994] suggested a critical surface Richardson number $Rf_{cr} = -\alpha g\nu/{u^*}^4 = -1.510^{-4}$ with the thermal expansion coefficient α, the kinematic viscosity ν, the friction velocity

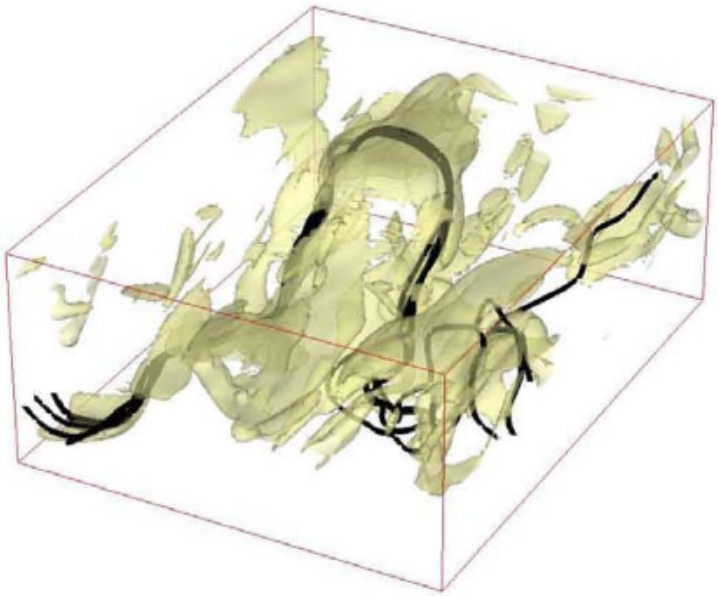

Figure 2.2.: Horse shoe vortex, bursting to the water surface. Image from Tsai [2007]

u^* and $q_0 = -Q_0/c_p\rho$ with the vertical total heat flux q_0, the specific heat c_p and the density ρ of water to describe the transition between free and forced convection.

The conclusion might be that these streaks are caused by shear induced turbulence, but still the question for the formation mechanism remains. Tsai et al. [2005] points out that one possible mechanism is that of horse shoe vortices that form in the turbulent shear layer by turning and stretching the span-wise vortices. These coherent turbulent structures move upward until their upper ends burst into the surface and therefore cause the upwelling of warmer and slower water at the surface. Chernyshenko and Baig [2005] suggest another mechanism for the formation of streaks. In this scheme, the lift-up of the mean profile in combination with shear stress and viscous diffusion together lead to the formation of the streaky pattern.

2.5. Wave-shear coupled turbulence

2.5.1. Waves on the water surface

As the wind stress increases, the water surface is shaped by the appearance of surface waves. Ocean surface waves are ubiquitous on the sea surface and appear as wind seas in a characteristic range of frequencies. Surface waves can travel across the ocean as sea swell before they break into a shore.

Linear waves

Deep water waves with a long wave length in irrotational, inviscid flow are in first approximation described by linear wave theory (detailed derivation e.g., in Dean [1991]; Kundu [2008]). The

dispersion relation of the wave frequency ω and wavenumber k is given by

$$\omega^2 = k\left(g + \frac{\sigma k^2}{\rho}\right)\tanh\left(kh\right). \tag{2.25}$$

where *sigma* is the surface tension. For water depths h larger than half a wavelength ($h > 0.5\lambda$) the dispersion relation simplifies to

$$\omega = \sqrt{k\left(g + \frac{\sigma k^2}{\rho}\right)} \tag{2.26}$$

because tanh $kh \approx 1$ for large kh. The phase velocity of a linear deep water wave is thus

$$c(k) = \frac{\omega}{k} = \sqrt{\frac{g}{k} + \frac{\sigma k}{\rho}} \tag{2.27}$$

For large waves the main restoring force is gravity which means that surface tension is negligible and the linear dispersion relation

$$\omega = \sqrt{gk} \Rightarrow \lambda_{dw} = \frac{gT^2}{2\pi}, \tag{2.28}$$

is a good approximation. Thus, the deep-water wavelength given by λ_{dw} can easily be estimated from the wave period T.

Capillary waves

Capillary waves are very small waves with wavelengths of not more than a few centimeters. On this length scale the effect of surface tension is non-negligible and Equation 2.26 holds. This means that at small wavelengths and large k the phase velocity is proportional to $\sqrt{k}$ while at larger wave lengths and small k the phase velocity is proportional to $\sqrt{1/k}$. In the transition range gravity and capillary waves have the same phase velocities. Moreover, energy is exchanged between both groups via non-linear interaction [Longuet-Higgins, 1963]. This means that groups of "parasitic capillaries" form on the leeward faces of gravity waves of a certain steepness and then travel with those waves because they have the same phase velocity.

Surfactants

Surfactants are "surface active agents", substances which form mono-molecular layers, surface slicks, on the water surface [Hühnerfuss, 2006]. They can result from biological activity in the ocean or be of anthropogenic origin such as oil slicks. There are soluble as well as insoluble surfactants but their common feature is that they consist of a hydrophobic part above the water surface and a hydrophilic part in the water. This leads to a viscoelastic force which acts in horizontal direction [Scott, 1974] and also enables the propagation of longitudinal waves along

the water surface [Alpers, 1989]. These waves are Marangoni waves and were first discovered by Lucassen [1968]. They cause high energy dissipation rates due to the strong viscous dampening.

Small capillary waves effectively act on the same length scales as Marangoni waves. An interaction between transversal capillaries and longitudinal Marangoni waves leads to a very efficient dampening of capillary waves while larger scale gravity waves are hardly affected.

As a results, surfactants lead to a considerably reduced surface roughness [Kiefhaber, 2014] and can lead to a very smooth water surface when at the same wind speed and clean water the surface would be covered with ripples.

Stokes waves

Most real waves are not well described by linear wave theory, e.g., microscale breaking waves but also capillary waves. Especially in wind driven seas, waves are considerably steeper than sinusoidal shapes. Stokes wave theory [Stokes, 1847] provides a means to consider more complex wave forms than the sinusoidal shape by considering higher order terms, but will not be outlined in detail in this thesis (refer to for example Kundu [2008]).

Below the surface, fluid parcels are set into circular motion. Their trajectories are closed ellipses in the case of linear (Airy) waves. In the case of non-linear (Stokes) waves the ellipses are now open and the water particles carry out spiral movements, thus, moving slowly forward. This additional wave drift is comparatively small and was found to be less than 1 % of the linear wave speed in the experiment at UNSW that will be discussed later in this study.

Microscale breaking waves

Microscale breaking of waves is commonly observed at the ocean and in the laboratory. Wind driven waves start breaking at wind velocities of approximately 5 m/s [Banner and Phillips, 1974]. Breaking waves can be characterized by a spilling region that is located directly behind the wave crest which is a strong divergence region. Behind the spilling region there is a clearer defined convergence region at the toes of the waves [Peirson and Banner, 2003]. The breaking of waves leads to a very high vorticity close to the surface at the toes of the spilling region [Peirson and Banner, 2003]. Microscale breaking leads to surface renewal and regions of surface divergence at the leeward faces of the waves and therefore to a considerable thinning of the mass boundary layer. Thus, microscale breaking leads to a clearly enhanced gas exchange [Csanady, 1990; Peirson et al., 2014; Zappa et al., 2001].

2.5.2. Langmuir circulation

In the presence of small gravity waves the characteristic temperature pattern at the water surface exhibits cold streaks with larger spacings and longer life time than shear induced turbulence (compare Figure 7.1 and [Caulliez, 1998; Melville et al., 1998; Schnieders et al., 2013; Veron and

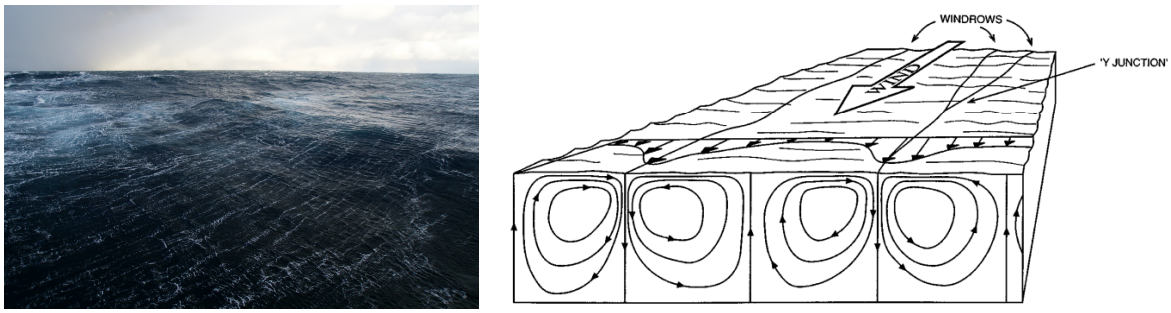

Figure 2.3.: Left: Strong wind at the South Pacific, white streaks of foam in wind direction are clearly visible at the water surface Right: Flow pattern below idealized Langmuir cells [Thorpe, 2004]

Melville, 2001]). Similar streaks of foam and seaweed and of far larger scales have been long known by sailors. They were first investigated (and named) by Langmuir [1938].

Langmuir circulations develop through a coupling of surface waves and wind shear and form an important pathway for the transfer of momentum from atmosphere to ocean [Thorpe, 2004]. They have first been described as large scale circulations with spacings of several meters [Leibovich, 1983] but later, cold streaks with spacings of only centi- and decimeters have been discovered [Caulliez, 1998; Melville et al., 1998; Veron and Melville, 2001]. Craik and Leibovich [1976] developed the Craik-Leibovich set of equations (CL II) to describe the underlying process:

$$\frac{\partial u}{\partial t} + v\frac{\partial u}{\partial t} + w\frac{\partial u}{\partial t} = La\ \nabla^2\ u \tag{2.29}$$

$$\frac{\partial \Omega}{\partial t} + v\frac{\partial \Omega}{\partial t} + w\frac{\partial \Omega}{\partial t} = La\ \nabla^2\ \Omega - \frac{du_s}{dz}\frac{\partial u}{\partial y} \tag{2.30}$$

with velocities u,v and w, the Langmuir number La, the vorticity Ω and the Stokes drift given by $u_s = 2S_0\ e^{2\beta z}$, S_0 and β empirical constants.

The flow is governed by the dimensionless Langmuir number [Leibovich and Paolucci, 1981] representing the quotient of viscous forces, e.g., the diffusion of downwind viscosity and inertial forces which produce the vorticity by vortex tilting and stretching by the effect of waves [Thorpe, 2004]. In the case of monochromatic waves with a fixed frequency f, wave number k and amplitude a, the Langmuir number can be defined as [Leibovich and Paolucci, 1981]

$$La = \left(\frac{\nu_t^3 k^2}{f a^2 u^{*2}}\right)^{1/2} \tag{2.31}$$

These equations show the coupling of two main features of transport of momentum across the air-sea interface: Langmuir circulations (LC) develop because of the interaction of surface stress (friction velocity u^*) and surface waves (Stokes drift u_s).

Langmuir circulations (LC) play a crucial role in air-sea interaction processes. Since the early work of Langmuir [1938] considerable progress has been made regarding the structure and fluid

dynamics of LCs [Craik and Leibovich, 1976]. In laboratory measurements as well as in field experiments, small scale Langmuir circulation has been observed and examined (for example by Caulliez [1998]; Gemmrich and Hasse [1992]; Melville et al. [1998]; Sanjou et al. [2011]; Veron and Melville [2001]). Gemmrich and Hasse [1992] showed the influence of LC on heat transfer rates in the baltic sea, that increased considerably in the presence of LC. Caulliez [1998] showed the appearance of Langmuir circulations on comparatively small scales in the laboratory and Melville et al. [1998]; Veron and Melville [2001] showed in an intensive study the onset of LCs and their impact on gas-exchange. It has been shown that LC induced cold streaks on the water surface do not appear before the onset of surface waves and only at critical Reynolds numbers. Melville et al. [1998] found that LCs scale with the depth of the shear layer and observed a span-wise scaling of $l_c = 5.42\,\mathrm{cm}$. Measurements conducted by Sanjou et al. [2011] indicate the significance of wind speed on the spacing of the Langmuir vortices. Mizuno [2011] observed Langmuir circulations in a linear wind wave channel that were destroyed by additional mechanical waves thereby contradicting CL II theory.

On larger scales, Langmuir circulations have been observed in airborne measurements leading to image sizes of up to several kilometers by Marmorino et al. [2005, 2007, 2009]; Zappa et al. [2004]. Here the information from cold streaks caused by Langmuir circulation have been used to estimate the depth of the surface mixed layer.

There have been no studies that cover both small scale structures and large scale structures within one study. A comparison of strength and occurrence of different sizes is therefore still missing.

3. Conceptual models of near surface turbulence

The transfer velocity or rate determines how fast heat and gas are exchanged between atmosphere and ocean, independent of the concentration difference. The transfer rate depends strongly on the turbulent state of the water surface and, therefore, varies considerably on relatively small scales [Wanninkhof et al., 2011]. However, the transfer rate is difficult to measure, especially in field conditions. Several methods exist on a range of scales, from small scale models to eddy covariance methods on intermediate time and spatial scales to mass-balance techniques, e.g., dual tracer methods, [Garbe et al., 2014] but all require in-situ measurements and the results are spatial and temporal averages.

Various conceptual models describe the transfer process based on observed turbulent processes. Estimates of transfer rates from these models of surface turbulence provide an alternative to in-situ measurements. Depending on the model, transfer rates can be estimated with high spatial and temporal resolution.

In the following section, three state-of-the-art models are presented which describe turbulent processes near the water surface and derive the transfer rate. Furthermore, the focus will be on heat transfer rates. There has been some discussion on whether heat transfer rates are directly transferable to gas transfer rates [Asher et al., 2004; Atmane et al., 2004; Nagel et al., 2014; Zappa et al., 2004], however, heat transfer rates have been shown to correlate closely with exchange rates of soluble gases [Garbe, 2001; Jähne and Haussecker, 1998; Jähne et al., 1989; Nagel et al., 2014; Popp, 2006; Schimpf, 2000].

3.1. Thin stagnant film model

The thin stagnant film model describes the water surface as a flat solid boundary with boundary layers on either side. It was first developed by Whitman [1923] and applied to the water surface by Liss and Slater [1974]. In the model assumption, diffusion is the only relevant transport process. Consequently, a diffusion layer of the thickness δ_c develops above a well mixed bulk. The diffusive flux F through the water surface is thus given by $F = -DdC/dz$ where D is the diffusion constant of the heat or mass in water and C the concentration. The transfer rate k is entirely defined by the diffusion constant and is given by $k = D/\delta_c$. Ultimately, the rate of transfer depends only on the diffusivity and the thickness of the thin film, the mass diffusion layer. In this framework turbulence can be incorporated by assuming that the thickness of the

boundary layer δ_c is reduced. However it is a very simple model that does not include turbulent mixing.

3.2. Surface renewal model

Another conceptual model to describe transfer processes at the air- sea interface was presented by Higbie [1935] and further developed by Danckwerts [1951]. In contrast to the thin film model, here, turbulent mixing is accounted for as a statistical process. Here, in a random renewal process water parcels from the well mixed bulk are instantaneously transfered to the water surface. In comparison to the film model it weakens the dependence on the molecular diffusion constants from a linear term to a $\sqrt{D}$ dependence. Depending on the description of the renewal events whether a single turbulence-dependent renewal rate [Higbie, 1935] is assumed or modulated by turbulent forcing [Danckwerts, 1951], the exact solution for the transfer rate k varies. However, all realizations of the conceptual model have the formulation

$$k \sim \sqrt{\frac{D}{\tau}} \tag{3.1}$$

where τ is the renewal timescale. Surface renewal models have been successfully applied to thermographic data of the water surface to estimate heat transfer rates from the distribution of surface temperatures (e.g. Garbe et al. [2004]). The following derivation of an expression for the heat transfer rate from infrared images was proposed by Garbe et al. [2004].

The transfer rate of heat is defined in by the net heat flux j and the difference between skin and bulk temperature ΔT. The expression for the transfer rate k_{heat} is then

$$k_{\text{heat}} = \frac{j}{\rho c_p \Delta T} \tag{3.2}$$

where the density is given by ρ, the specific heat by c_p. A water parcel at the surface will be continuously cooled under a constant heat flux across the air-sea boundary. Assuming that vertical transport of heat is the dominant renewal mechanism the cooling process at the water surface can be described by [Soloviev and Schlüssel, 1996]:

$$T_{\text{surface}}(t) = \alpha j \sqrt{t - t_0} + T_{\text{bulk}} \tag{3.3}$$

$$\alpha = \frac{2}{\sqrt{\pi\kappa} c_p \rho} \tag{3.4}$$

where t_0 is the time when the water parcel reaches the surface and κ is the thermal diffusivity of heat in water. $t - t_0$ defines the surface renewal time scale $\tau = t - t_0 = (T_{\text{surface}}(t) - T_{\text{bulk}})^2 / \alpha j$. Inserting equation 3.2 in equation 3.3 [Garbe et al., 2004] gives:

$$k = \frac{1}{2}\sqrt{\frac{\pi\kappa}{\tau}} \tag{3.5}$$

Differentiating equation 3.3 with respect to time and solving for j leads to:

$$j = \frac{2\sqrt{\tau}}{\alpha} \frac{dT_{\text{surface}}}{dt} \tag{3.6}$$

Inserting equation 3.6 into equation 3.3 and both into equation 3.5 results in a formulation for the heat transfer rate [Garbe et al., 2004]:

$$k = \sqrt{\frac{\pi\ \kappa}{2}} \cdot \sqrt{\frac{\dot{T}}{\Delta T}} \tag{3.7}$$

where k depends on the molecular diffusion constant κ, the total derivative of surface temperature dT/dt and the difference between skin and bulk temperature $\Delta T = T_{\text{bulk}} - T_{\text{surface}}$.

3.3. Surface divergence model

After the development of the first eddy renewal models, Banerjee et al. [1968] and Lamont and Scott [1970] related surface renewal to turbulent parameters of the bulk, e.g., viscous dissipation. But the remaining challenge to measure the mean time between renewal events proved very difficult [Komori et al., 1989; Rashidi and Banerjee, 1990; Rashidi et al., 1990]. McCready et al. [1986] therefore suggested a different approach based on the assumption that at a rough surface, only surface normal fluid motion is relevant for transfer across the interface. Due to the equation of continuity, surface normal velocity can be expressed by the surface divergence (compare Equation 2.2). The surface divergence model assumes the transfer rate k to be only determined by the root mean square of surface divergence β'

$$\overline{k} = -c\sqrt{D\beta'} \tag{3.8}$$

where c is a constant of proportionality and D the molecular diffusivity. This means that in comparison to the surface renewal model the surface renewal time scale has been replaced by the surface divergence. The surface divergence model has been tested on various flow conditions, most recently in particle image velocimetry (PIV) measurements by Herlina and Jirka [2008]; Siddiqui and Loewen [2007]; Xu et al. [2006]. The proportionality constants can theoretically be determined from a fit to the homogeneous isotropic energy spectrum [Banerjee, 1990] and should not be applied to shear driven flow [Turney and Banerjee, 2013]. However, Banerjee et al. [2004] still found a good agreement in experiments including wind shear.

Most recently, Turney and Banerjee [2013] extended of the surface divergence model to the application of wind driven flow, which contains a combination of the surface renewal model and the surface divergence model.

$$\overline{k} = \sqrt{\frac{D}{\overline{\tau}}}\ e^{\frac{1}{2\beta'\overline{\tau}}}\ \text{erfc}\left(\sqrt{\frac{1}{2\beta'\overline{\tau}}}\right) \tag{3.9}$$

where the root mean square surface divergence β' and surface renewal time scale τ are needed to define the transfer rate k. Furthermore, a criterion can be derived of the relevance of a steady divergent motion to air-sea interaction Turney and Banerjee [2013]. Only if $\beta\tau > 1$ is a process relevant to air sea interaction.

3.4. Eddy renewal model

Both models discussed in the previous section, the surface renewal model and the surface divergence model, are essentially one dimensional models of turbulent exchange processes. Looking at the temperature pattern at the water surface, however, shows defined two dimensional images of the three dimensional processes underneath. The eddy renewal model, proposed by Hara et al. [2007] takes this into account and models the footprints of surface eddies. The conceptual model assumes eddies at the water surface which are uniform in y and stationary in t and can therefore be described by the heat advection diffusion equation:

$$\frac{dT}{dt} = \frac{\partial T}{\partial t} + u\,\frac{\partial T}{\partial x} + v\,\frac{\partial T}{\partial y} + w\,\frac{\partial T}{\partial z} = \kappa\left(\frac{\partial^2}{\partial x^2} + \frac{\partial^2}{\partial y^2} + \frac{\partial^2}{\partial z^2}\right)T \tag{3.10}$$

Assuming the eddies are uniform in along wind direction and stationary in time this simplifies to:

$$u\,\frac{\partial T}{\partial x} + w\,\frac{\partial T}{\partial z} = \kappa\left(\frac{\partial^2}{\partial x^2} + \frac{\partial^2}{\partial z^2}\right)T \tag{3.11}$$

The surface velocity is assumed to be periodic with wavenumber $\tilde{k}$:

$$u = u_0\,\sin(\tilde{k}x), \qquad\qquad \tilde{z} = 0$$

As described in Hara et al. [2007] non-dimensionalizing leads to the following set of equations:

$$\sin\,\tilde{x}\frac{\partial \tilde{T}}{\partial \tilde{x}} - \tilde{z}\,\cos\,\tilde{x}\,\frac{\partial \tilde{T}}{\partial \tilde{z}} = \frac{\partial^2 \tilde{T}}{\partial \tilde{z}^2} + \mathcal{O}(\tilde{k}\delta), \tag{3.12}$$

With boundary conditions:

$$\frac{\partial \tilde{T}}{\partial \tilde{z}} = -1, \qquad \tilde{z} = 0, \qquad \tilde{T} = 0, \qquad \tilde{z} = -\infty$$

And non-dimensional variables:

$$\tilde{x} = \tilde{k}x, \qquad \tilde{z} = \frac{z}{\delta}, \qquad \delta^2 = \frac{\kappa}{\tilde{k}u_0}, \qquad \tilde{T} = \frac{(T - T_b)k}{\delta j}$$

The non-dimensional temperature $\tilde{T}$ contains both the total heat flux j and the bulk temperature T_b and thus determines the temperature distribution within the eddy. The equations are solved numerically and the solution is the surface temperature field within one surface eddy (see Figure

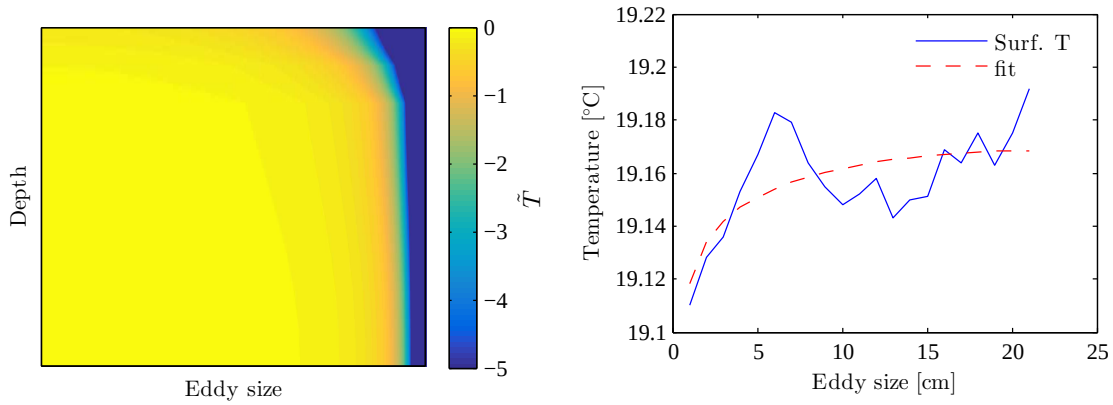

(a) (b)

Figure 3.1.: a) Numerical solution of eddy renewal model [Hara et al., 2007]. Theoretical temperature profile within a surface eddy, color represents non-dimensional temperature $\tilde{T}$. b) Fitted theoretical curve to surface temperature within eddy.

3.4 a)). To derive the heat flux, the modeled surface temperature is fitted to the measured surface temperature in an infrared image (see Figure 3.4 b)). This way the bulk temperature T_b and the total heat flux j are derived from each fit to a surface eddy.

This has been shown to provide accurate results by Hara et al. [2007] and Hung et al. [2011] on numerical and thermographic data. However, often the resolution of infrared images is relatively small and subject to high noise levels. The definition of surface eddies by temperature extrema does not always lead to the accurate localization of surface eddies [Schnieders et al., 2013]. Also the superposition of eddies of various sizes is a common feature of the water surface and not incorporated in the model. An adaptation of the eddy renewal model with extensions regarding a more robust estimate of the heat transfer rate will be presented in Chapter 9

4. Experiments

The data on which later analyses are based was measured in three facilities, the Aeolotron, Heidelberg, the Water Research Laboratory, Sydney and the Air Sea Interaction Saltwater Tank, Miami. Part of these measurements have already been described in Schnieders et al. [2013] and the Diploma thesis Schnieders [2011]. Later data was taken again in Aeolotron 2014 under a broader wind spectrum, a new infrared camera and additional external parameters. A comparison of data recorded in different tanks with different cameras is especially useful when examining the scales of the surface heat pattern in Section 8. In the following, these experiments are each described individually.

4.1. Aeolotron, University of Heidelberg

The experiments were conducted at the circular wind wave facility at the Institute for environmental Physics in Heidelberg (IUP).

The water depth was kept constant at (1.00 ± 0.01) m throughout the experiment. The diameter of the tank is 10 m with a perimeter of 29.2 m. The width and height of the channel are 61 cm and 2.30 m respectively. Two fans within the air space on opposite sites produce wind up to a wind speed of 12 m/s.

The channel can be operated with closed doors and a closed air space to minimize the latent heat flux (relative humidity of the air reaches $\sim 100\,\%$). The walls of the channel are insulated by a 9 cm layer of polystyrene to reduce sensible heat flux and the walls are covered with aluminum foil to minimize radiative heat flux. During the measurements with passive Thermography, for which the development of a cool surface layer is crucial, the channel was operated with an additional ventilation that circulated dry air from outside through the channel. Therefore, relative humidities were reduced to an approximately constant 60 %.

4.1.1. Experiments 2011

The wind speeds in this experiment ranged from 1 m/s up to 6 m/s one meter above the water surface. Mean square slope (MSS) values were obtained from the color imaging slope gauge (CISG) as described in Rocholz et al. [2011]. The water sided friction velocity was calculated from the momentum budget in the channel [Bopp, 2011]. For this purpose bulk water velocities were measured and the decay characteristics of the velocity of the water body after stopping the wind were determined from the spin-down time.

The measurements were repeated after adding 3 g Triton X-100. Triton X-100 is a surfactant that has a hydrophilic polyethylene oxide group which makes it soluble in water. By the reduction of surface tension it effectively suppresses capillary waves. To study the influence of capillary waves on the surface heat pattern all wind conditions were repeated with a surface slick. As as result Mean Square Slope values were close to zero for the low wind speed cases and the heat flux reduced in comparison to clean surface measurements.

The employed infrared camera is a Thermosensorik CMT 256 with a resolution of 256 x 256 Pixel(px) and a maximal frame rate of 880 Hz. The frame rate during the measurements was reduced to 60 Hz as a higher time resolution was not necessary. The temperature resolution of the camera amounts to 10 mK. The camera is sensitive to radiation in the range of $3.4\,\mu$m $-5.1\,\mu$m. The camera is mounted on top of the wave channel approximately 1.30 m above the water surface. To obtain a better spatial resolution a lens with a focal length of 50 mm was utilized. The spatial calibration with a target with a checkerboard pattern on the water surface yielded a spatial resolution of 0.1135 ± 0.0006 cm/px.

The temperature calibration of the camera was performed in the range of $15\,^{\circ}\mathrm{C} - 24\,^{\circ}\mathrm{C}$ in steps of $0.25\,^{\circ}\mathrm{C}$. For this purpose a reference calibration blackbody was set to the respective temperatures, an infrared image was recorded of each temperature and subsequently used for the calibration of the camera. Sequences with 1000 images ($\sim$ 16 s) each were recorded for 20 min, resulting in 50 sequences and 50000 infrared images.

Table 4.1.: Aeolotron, Measurements with the Thermosensorik CMT 256. U, u^*, MSS and Heat flux are the wind speed in m/s, the friction velocity in cm/s, the Mean Square Slope values and the total heat flux in $\mathrm{W/m^2}$ respectively. The measurement error of the friction velocity is 0.02 centimeters per second for low and intermediate wind speeds and 0.1 centimeters per second for the highest wind speed. The values for the heat flux are mean values for the respective wind speed.

	Clean water surface			Triton X-100		
U	u_*	MSS	Heat flux	u_*	MSS	Heat flux
1,8	0,20	0,014	170	0,18	0,005	142
2,4	0,33	0,017	170	0,25	0,005	142
2,7	0,34	0,024	181	0,40	0,008	158
4,6	0,77	0,049	219	0,64	0,010	169
6,4	1,36	0,082	246	1,35	0,045	186

4.1.2. Experiments 2012

The clean surface measurements were again repeated with a new IR camera, an IRCAM Velox 327k M, which has a resolution of 640x512 px. The spatial resolution amounts to 0.078 ± 0.001 cm/px during the experiment which is considerably higher than in the previous measurement.

Table 4.2.: Aeolotron, Measurements with the IRCAM Velox 327k M. U u^*, T_{bulk} and η are the wind speed in m/s as measured in the facility circa one meter above the water surface, the water-sided friction velocity in cm/s, the bulk temperature measured inside the channel in °C and the mean squared wave height, respectively. The measurement error of the friction velocity is 0.04 centimeters per second for low and intermediate wind speeds and 0.12 centimeters per second for the highest wind speed.

	Clean water surface			Triton X-100		
U	u_*	T_{bulk}	η	u_*	T_{bulk}	η
2.4	0.40	19.11	0.09	0.30	19.45	0.06
3.2	0.49	19.05	-	0.38	19.48	-
3.5	0.53	18.98	0.5	0.42	19.51	0.02
4.2	0.64	18.91	1.2	0.47	19.53	-
4.8	0.74	18.85	2.0	0.59	19.54	1.4
5.1	0.81	18.78	-	-	-	-
5.4	0.87	18.71	4.0	0.64	19.58	-
6.0	1.04	18.65	6.4	0.74	19.62	-
6.5	1.19	18.59	8.7	0.85	19.64	6.9
7.0	1.30	18.53	11.6	1.01	19.68	-
8.3	1.77	18.49	19.9	1.44	19.70	17.8

4.1.3. Experiments 2014

The experiment from 2011 was repeated with the IRCAM Velox 327k M and a higher number of different wind wave conditions especially in the area around a friction velocity $u^* = 1$ cm/s, which has been shown to be a regime in which the surface turbulence clearly changes its characteristics from dominating shear turbulence to the onset of waves and the appearance of small Langmuir circulations. The spatial resolution of the images is 0.071 ± 0.001 cm/px. The measurements were again repeated with 3 g of the surfactant Triton X-100.

Additional water height measurements with a high spatial and temporal resolution were provided by a permanently installed laser set up [Horn, 2013]. The laser light of a wave legth of 405 nm is absorbed by added pyranine in the water and emits fluorescent green light. The position of the laser sheet is recorded with a high speed camera and from the position of the sheet the water height is computed. The analysis of wave heights is described in Bopp [2014].

An air conditioning system was installed in the facility within this work that gives control over air temperature and humidity in the closed facility. On two heat exchangers which are connected via a heat pump the air is first cooled down and condensed water removed and subsequently heated up again to reduce relative humidity. Additional energy is stored in the bulk water which can be controlled by the flow rate of water through another heat exchanger.

Simultaneous active and passive thermographic measurements were made to allow for a direct comparison of the data. A carbon dioxide laser emitting infrared radiation at a wavelength of 10.6 μm with a Gaussian intensity profile was used to heat patches of approximately 1 cm of the water surface.

4.2. Water Research Laboratory, University of New South Wales

The wind channel used for the experiments is a linear channel. The tank is 8.955 m long, 0.245 m wide and 0.610 m high. A detailed description of the experiments can be found in Peirson et al. [2014]. All technical data and experimental conditions were taken from this study.

The water depth during the experiments was $0.247\,\mathrm{m} \pm 1\,\mathrm{mm}$. The wind was produced by a ventilator at one end of the tank. To ensure a uniform airflow, guide vanes were installed just behind the ventilator. The tank is located in an insulated room at constant temperature of $21.5 \pm 0.5\ ^{\circ}\mathrm{C}$ throughout the experiment.

As wind generated and surface conditions in a linear tank are fetch dependent, the wind and wave conditions were chosen so that constant wave energy levels were obtained for the entire fetch length. To avoid biological activity, the water was steadily circulated through an earth filter and UV sterilizer, when no experiments were performed.

Wind wave conditions: Mechanical waves were produced by a paddle at one end of the tank. During the experiments measurements were conducted under eight different wind wave conditions.

Two **Low wave cases** (F34U21AK18) and (F21U39AK10) were performed at a fetch of 4.55 m and 3.1 m and therefore different wave characteristics at $U_{10} = 2.1\,\mathrm{m/s}$ and $3.9\,\mathrm{m/s}$ respectively. The numbers F34U21AK18 and F21U39AK10 describe wave frequency, wind speed and the value of ak. Here F34U21AK18, for example, stands for a wave frequency of 3.4 Hz, a wind speed of 2.1 m/s and a value of $ak = 0.18$. The low gravity waves were mechanically produced with a length 135 and 350 mm. The steepness of the waves was low enough that no parasitic capillary waves could evolve.

Two **Incipient breaking cases** (F34U21AK27) and (F24U39AK24) were also performed at a fetch of 4.55 m and 3.1 m at wind speed of $U_{10} = 2.1\,\mathrm{m/s}$ and $3.9\,\mathrm{m/s}$. Incipient breaking refers to waves as steep as possible before the onset of microscale breaking. Here parasitic capillary waves were present.

Two **Microscale breaking cases** (F34U57AK32) and (F31U39AK28) were also performed at a fetch of 4.55 m and 3.1 m. Wind speeds were $U_{10} = 5.7\,\mathrm{m/s}$ and $3.9\,\mathrm{m/s}$ as microscale breaking could not be maintained for $U_{10} = 2.197\,\mathrm{m/s}$

The **Capillary ripple case** (F63U42AK00) were performed at a fetch of 3.1 m with freely propagating capillary waves present. The wind speed was $U_{10} = 4.2\,\mathrm{m/s}$, no gravity waves developed.

The **Flat water case** (F00U21AK0) was performed at a fetch of 4.55 m .The wind speed $U_{10} = 2.1\,\mathrm{m/s}$ was the highest possible wind speed without the formation of freely propagating waves.

A wave probe recorded the surface elevation at 1 kHz. Additionally PIV and LIF measurements were performed, the detailed description of which can be found in Peirson et al. [2014] and will not be further discussed in this study. The infrared camera was a cedip Jade 550, operated

at a frame rate of 100 Hz with a resolution of 320 x 240 Pixel. The camera was mounted on top of the channel looking down on the water surface with the wave probe visible. The spatial calibration using the wave probe as a target yielded a spatial resolution of 0.066 ± 0.002 cm/px. The data was recorded in two independent sequences of 4996 images for every experimental condition. The data presented here was measured in three facilities, the Aeolotron, Heidelberg, the Water Research Laboratory, Sydney and the Air Sea Interaction Saltwater Tank, Miami. Therefore, a comparison of surface heat patterns under very different experimental conditions and recorded with different imaging systems is possible.

Table 4.3.: Water Research Laboratory. U, u^* are the wind speed in m/s, the water-sided friction velocity in cm/s. The wave steepness and the wave frequency in 1/s are given by ak and f respectively.

U	u_*	ak	f
2,1	0,45	0,18	3,4
2,1	0,75	0,27	3,4
5,7	1,81	0,32	3,4
4,2	0,62		6,3
3,9	0,81	0,10	2,1
3,9	1,11	0,24	2,4
3,9	1,46	0,28	3,1

4.3. Air Sea Interaction Saltwater Tank, Rosenstiel School of Marine & Atmospheric Sciences

The experiments were performed at the Air-Sea Interaction Salt-water Tank (ASIST) located at the University of Miami (Rosenstiel School of Marine and Atmospheric Science) and are described in detail in Smith et al. [2007].

The linear tank is 15 m long, 1 m wide and 1 m high. The water depth during the experiment was 40 cm, leaving 60 cm for the wind. For all the cases presented here a water pump was used to maintain a small, constant current (approximately 3 cm/s) that enabled control of the water temperature. Water temperatures were varied to provide air-water temperature differences ranging from $-15\,\circ$C to $+15\,\circ$C. Wind speeds were varied from 0 m/s up to 10 m/s. All cases presented here are cool-skin cases e.g. the heat flux was directed out of the interface.

The infrared images were taken with an Indigo Systems Merlin Mid-Wave IR sensor with a resolution of 320 x 256 pixels. The spatial resolution of the images amounts to 0.0907 cm/pixel. The array is cooled to increase sensitivity to better than $0.02\,\circ$C. The imager is sensitive to radiation in the $3 - 5$ μm band. The maximum frame rate of the IR imager is 60 Hz, although the actual acquisition rate was varied based on the flow being imaged. All the imagery was taken looking down at the water surface at an angle of approximately 60 degrees from the horizontal through a hole in the top of the tunnel. This was done for two reasons: first, to reduce the occurrence of reflections of the camera itself appearing in the data, and second, to

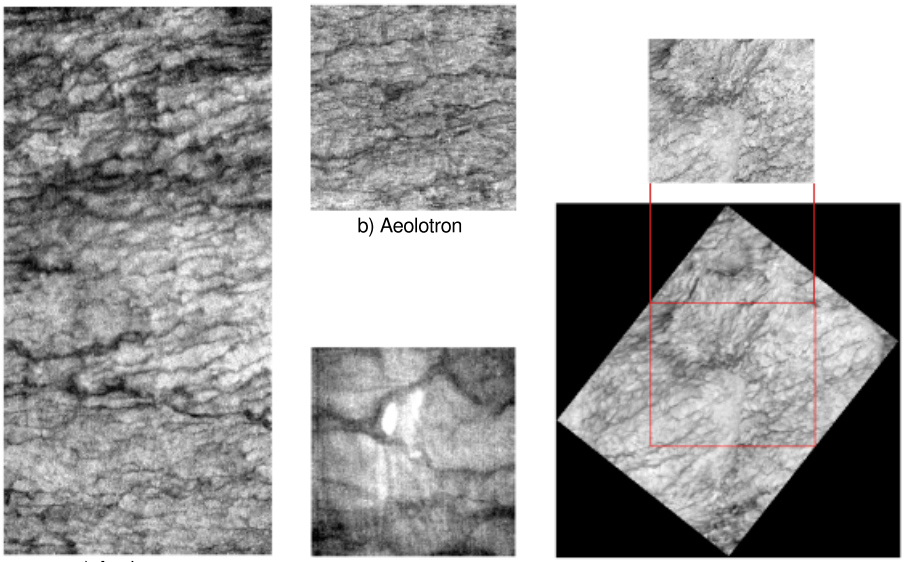

Figure 4.1.: Infrared images from several facilities. The images were recorded with different IR cameras and different spatial resolution (res): a) Aeolotron, Heidelberg, Thermosensorik CMT 256, $res = 0.11$ cm/px, $u^* = 0.8$ cm/s; b) Aeolotron, Heidelberg, Ircam Velox 327k M, $res = 0.07$ cm/px, $u^* = 0.8$ cm/s; c) WRL, Sydney, cedip Jade 550, $res = 0.07$ cm/px, $u^* = 1.1$ cm/s, a warm laser heated spot is clearly visible in this image; d) ASIST, Miami, Indigo Systems Merlin, $res = 0.09$ cm/px, $u^* = 0.9$ cm/s, the original image is rotated and a rectangular section cut for the analysis.

accommodate a second IR imager viewing through the same port in the roof of the wind-wave tunnel. Additionally the camera was oriented diagonally to the wind direction.

Table 4.4.: ASIST Facility. U, u^* are the wind speed in m/s, the water-sided friction velocity in cm/s. The heat flux is given in $\mathrm{W/m^2}$.

U	u_*	Heat flux
1,9	0,22	393
3,0	0,31	601
4,0	0,43	850
5,0	0,57	1144
7,0	0,93	1764
10,1	1,65	2592

4.4. Overview of infrared images

A range of laboratory facilities in Heidelberg, Sydney and Miami and infrared cameras was chosen for this analysis to avoid any bias due to the geometry of the channel or the resolution of the infrared camera and to thus, define a universal parameter.

A comparison of infrared images from the three different facilities is shown in Figure 4.1. The left image a) was taken in the Aeolotron, Heidelberg with a spatial resolution of $res = 0.11$ cm/px

and at a friction velocity of $u^* = 0.8$ cm/s. Image b) was taken under the same conditions in the same tank but with a spatial resolution of $res = 0.07$ cm/px. In Image c) an image from WRL, Sydney is shown, which was recorded with a spatial resolution of $res = 0.07$ cm/px at a friction velocity of $u^* = 1.1$ cm/s. In the image a laser heated spot is clearly visible but could easily be identified over its temperature and did therefore not further influence the analysis. Image c) is from the ASIST facility, Miami, the spatial resolution is $res = 0.09$ cm/px and the friction velocity is $u^* = 0.9$ cm/s. The camera was oriented diagonally to the wind direction. Therefore, the images are rotated in such a way that the fish scale structures lie in the horizontal axis and a rectangular window aligned with the structures was cut Figure 4.1 d) and e). This was necessary to avoid a suppression of larger scale spacings in the corners of the image.

5. Estimation of surface velocities from infrared images

The surface velocity field is a good indicator of the dynamics of the water surface and provides valuable information about the ongoing processes. Therefore, techniques for the estimation of flow fields from a sequence of images will be presented in the following sections. First, a review of existing state-of-the-art algorithms is given. In Section 5.2 an adapted algorithm especially suited for the analysis of infrared images is presented. An alternative approach via active Thermography is presented in Section 5.3 and a comparison between both approaches in Section 5.4 which is also used for the determination of errors.

5.1. Motion estimation

The estimation of motion from a sequence of images is one of the core research topics in computer vision. The goal is to estimate a flow field from the displacement of objects or gradients between two subsequent images in time. Several methods have been developed to deal with this task. Among others there are feature tracking based techniques [Buxton and Buxton, 1984; Wills et al., 2006], velocity estimation from cross correlation, area [Anandan, 1989] and phase [Fleet and Jepson, 1990] based techniques. A very important group of techniques are optic flow based techniques.

5.1.1. Optic Flow

The principal assumption of optical flow is brightness constancy, e.g., it is assumed that the brightness of a pixel (x, y) in one images stays constant if shifted to another position $(x+u, y+v)$ in the next time step:

$$I(x, y, t) = I(x + u, y + v, t + 1). \tag{5.1}$$

Here, I are the gray values of the pixels and u and v are the x- and y-components of the desired flow field. If the displacement is assumed to be small and the variation in space and time to be smooth a first order Taylor expansion gives:

$$I_x\ u + I_y\ v + I_t = 0 \tag{5.2}$$

where I_x, I_y, and I_t denote partial derivatives in spatial directions, x and y, and temporal coordinate, respectively. The velocities u and v denote the components of the velocity vector $\mathbf{v}$. Unfortunately, one equation is not sufficient to determine two unknown quantities u and v. This leads to the so-called aperture problem.

Aperture problem

The aperture problem is a common challenge among all optical flow based techniques. It describes the fact that for non-vanishing image gradients, it is only possible to determine the flow components in the direction of the gradient, i.e normal to image edges. A good illustration is the image of an illuminated spinning sphere which will appear to stand still because the light source remains at the same place.

There are two major ways to approach this problem. The first was introduced by Lucas and Kanade [1981] and solves the basic optical flow equation in a local neighborhood in which the flow is assumed to be constant. Because the flow is computed locally, it is called a local method. This method is still popular today and applied in wide variety of applications. However, in large image areas without gradients the result of the velocity estimation will be zero.

The second way to approach the aperture problem is based on variational methods. Here, a second constraint next to the brightness constancy constraint is applied, based on assumptions about the flow field. Therefore, dense flow fields can be computed even in areas with no or constant gradients based on the global assumption of the flow field, hence these methods are called global methods. The first example of a variational technique was introduced by Horn and Schunk [1981]. Because of the extremely good performance and the ability to compute dense flow fields of variational techniques, the following sections will concentrate on them.

5.1.2. Variational techniques

Variational methods are a powerful tool, give excellent results, and have been applied, tested and improved ever since the publication of the first approach of Horn and Schunk [1981]. As the global solution of the basic optical flow requires additional input a second term is introduced, the regularizer.

Horn and Schunck

In the first approach by Horn and Schunk [1981] the flow field is assumed to be smooth. Consequently, large spatial gradients in the flow field will be penalized. This additional term makes the equation naturally harder to solve but as the formulation can be treated as a variational problem this is easily possible. Thus, the problem takes the form of an energy functional that needs to be minimized [Horn and Schunk, 1981].

$$E(u,v) = \int_{\Omega} \left(\underbrace{(I_x u + I_y v + I_t)^2}_{\text{Data term}} + \alpha \underbrace{|\nabla u|^2 + |\nabla v|^2}_{\text{Smoothness term}} \right) dx \tag{5.3}$$

Here, the integral over Ω denotes the integral over the image space. The familiar brightness constancy equation is called the data term and the regularizer based on the smoothness assumption is called the smoothness term. The parameter α is the smoothness parameter that can be used to vary the weight of the penalizer function. As a consequence, the desired flow field must satisfy the Euler-Langrange equations:

$$(I_x u + I_y v + I_t) I_x - \alpha \Delta u = 0 \tag{5.4}$$

$$(I_x u + I_y v + I_t) I_y - \alpha \Delta v = 0 \tag{5.5}$$

Since the original Horn and Schunck equation, several alterations and improvements have been suggested, all based on the variational approach.

Non quadratic smoothness terms

Non quadratic smoothness terms have been suggested by several authors [Aubert et al., 1999; Brox, 2005; Mémin and Perez, 1996; Weickert, 1998; Weickert and Schnörr, 2001]. The quadratic penalizer, that is strongly influenced by outliers, can be replaced by a more robust function. One example is the non quadratic total variation regularizer $\Psi(s^2) = \sqrt{s^2}$, a variant of the L1 norm, utilized by Brox et al. [2004]. The new function allows for discontinuities in the estimated flow field and is a so called flow-driven regularizer. (By contrast image-driven regularizers also allow discontinuities but based on discontinuities in the image [Weickert and Schnörr, 2001] which does not always correspond to discontinuities in the flow field.)

Non quadratic data term

There are several reasons why the optic flow constraint in the data term is not fulfilled, i.e. due to occlusion, brightness change or noise. The extension of the non quadratic penalty function from the smoothness term to the data term can be a means to address these problems [Black and Jepson, 1996; Bruhn et al., 2005; Mémin and Perez, 1996].

Gradient constancy assumption

A gradient constancy equation was introduced by Brox et al. [2004]. The classic gray value constancy assumption does not hold if the illumination changes or changes in brightness occur. Therefore, a higher order data term was introduced and the constancy of gradients is assumed:

$$\nabla I(x,y,t) = \nabla I(x+u, y+v, t+1). \tag{5.6}$$

This data term is very robust against any changes in brightness but due to the higher order derivatives much more sensitive towards noise. It has thus been suggested to combine the gradient constancy assumption with the gray value constancy equation to one data term with a weighing parameter for the gradient constancy by Brox et al. [2004].

Multiscale approach

The basic assumption of Horn and Schunck works well for small displacements. But if the displacement is larger than one pixel per frame the minimization process often gets trapped within a local minimum. A solution to this problem is a multi-scale approach.

Very commonly used is the combination of a coarse to fine, gaussian pyramid-based [Jähne, 2005] estimation [Brox et al., 2004; Bruhn et al., 2005; Papenberg et al., 2006; Steinbrucker et al., 2009; Sun et al., 2010]. By smoothing and subsequent subsampling of pixels of an image, at every pyramid step the image size is reduced and simultaneously the noise level. The gaussian smoothing hereby prevents aliasing effects.

Starting from the top level of the pyramid with a coarse resolution on a smoothed image the first flow estimation is performed. One approach is to now use the estimated flow field as initialization for the next pyramid level. Alternatively, it has been suggested [Brox et al., 2004] to use the estimated velocity field to warp the images and reduce the displacement for the next pyramid level.

Median filtering

Median filtering has been shown to improve the result of the flow estimation considerably by Sun et al. [2010]. A 5 x 5 median filter in between each warping step especially avoids outliers. Sun et al. [2010] also showed that the application of a median filter is equivalent to the inclusion of a local term into the energy functional.

Learning-based optical flow

Learning-based optical flow is an extension of previous methods to deal with complex flow fields. Every flow field is treated as a linear combination of typical basis flows. It is called learning-based because the basic flow fields are learned from appropriate training data before applied to the new problem.

5.1.3. State of the art global optic flow

The employment of optic flow based velocity estimation to a wide variety of application has lead to numerous different alterations and suggestions for methods depending on the image data on which the velocity estimation is to be performed. Depending on noise level, illumination, kind of the movement (i.e. fluid flow, or camera movement along a scene) and expected discontinuities, different methods give better results. In the following, two algorithms are presented as examples

of extensions of the original optic flow algorithm by Horn and Schunk [1981] that give excellent results on different occasions.

Enhanced Horn and Schunck

This combination of methods in an optic flow based approach was first suggested by Brox et al. [2004] and has been used in different variants, i.e. Bruhn et al. [2005]; Liu et al. [2009]. It comprises a non quadratic smoothness and data term, a gradient constancy assumption and a multi-scale approach. In the following, bold symbols indicate vectors. The data term is given by

$$E_{\text{Data}}(\mathbf{v}) = \int_{\Omega} \Psi(|I(\mathbf{x}+\mathbf{v}) - I(\mathbf{x})|^2 + \gamma|\nabla I(\mathbf{x}+\mathbf{v}) - \nabla I(\mathbf{x})|^2)\mathbf{dx}, \tag{5.7}$$

and the smoothness term by

$$E_{\text{Smooth}}(\mathbf{v}) = \int_{\Omega} \Psi(|\nabla_3 u|^2 + |\nabla_3 v|^2)\mathbf{dx}. \tag{5.8}$$

The function $\Psi(s^2) = \sqrt{s^2+\epsilon}$ is a robust convex L^1 minimization function. ϵ is chosen to be 0.001 [Brox et al., 2004] and is a small constant that is introduced due to numerical reasons and keeps the function convex. The data term consist of a combination of gray value and gradient constancy. A piecewise smooth flow field is assumed, the gradient $\nabla_3 = (\partial_x, \partial_y, \partial_t)^T$ is a spatial-temporal gradient but can be replaced with just a spatial gradient if only two images are available. The total energy functional is then given by

$$E(\mathbf{v}) = E_{\text{Data}} + \alpha E_{\text{Smooth}} \tag{5.9}$$

with a smoothing parameter α.

5.1.4. Fluid flow estimation

Applications of image analysis in geo-sciences often concern fluid flows, either on global scales from satellite images or on smaller scales to study the flow of air or water in a specific environment. In this context, techniques based on correlation are widely used with good results [Fujita and Grandoso, 1968; Leese et al., 1971; Menzel, 2001]. A very commonly used technique is particle image velocimetry (PIV) in which the fluid flow is seeded with small particles and illuminated with a laser sheet. On this data cross correlation works extremely well and provides very accurate but sparse velocity fields. State of the art techniques are presented in, for example, [Raffel et al., 2007; Tropea et al., 2007]. Correlation techniques have also been applied to infrared images of the water surface with good results in Banerjee et al. [2004]; Chickadel et al. [2011]; Jessup and Phadnis [2005]. The right selection of the window size on which the correlation is

based is, however, of critical importance. This problem has been solved in part due to variable window sizes and gives good results on larger scales but remains limited for smaller scales.

Several attempts have been made to combine the advantages of a global optic flow scheme with the ability to capture fluid flows. [Arnaud et al., 2006; Cassisa, 2010; Corpetti et al., 2006, 2002; Fitzpatrick, 1988; Haussecker and Fleet, 2001; Heas et al., 2007] introduced data terms which are based more on the laws of fluid mechanics and are able to capture small scale movements and brightness changes due to changes of density (or any other quantity). But when estimating motion from fluid flows, all global methods deal with a common problem, which is surface divergence. All compressible flows will generate surface divergence in the image plane but also incompressible fluids, as water, will create two dimensional surface divergence at the water surface. Looking at the Euler-Lagrange equations of the traditional Horn and Schunck smoothness term (Equation 5.5) it becomes apparent that this is equivalent to minimising surface divergence (which would results in the same term $\alpha\Delta u$). As surface divergence is a crucial quantity in the description of a surface flow, this is a serious drawback.

A global optic flow approach to fluid motion

One viable global optic flow scheme to capture all features of fluid flow and estimate dense fluid flows was introduced by Corpetti et al. [2002]. To address the problems associated with the features of fluid flow a more physical based data term and a non divergence suppressing smoothing term were introduced. As fluid flows always obey the equation of continuity this is a good alternative for the data term [Corpetti et al., 2002]:

$$\frac{\partial E}{\partial t} + \operatorname{div}(E\mathbf{v}) = 0 \tag{5.10}$$

With $\operatorname{div}(E\ \mathbf{v}) = E \cdot \operatorname{div}\ \mathbf{v} + \nabla E \cdot v$ and $\frac{dE}{dt} = \frac{\partial E}{\partial t} + \nabla E \cdot v$ this becomes

$$\frac{dE}{dt} + E\ \operatorname{div}\ \mathbf{v} = 0. \tag{5.11}$$

To avoid penalizing divergence through the common smoothness term a so-called second order div curl regularizer [Suter, 1994] is employed.

$$\int_\Omega |\nabla \operatorname{div}\ \mathbf{v}|^2 + |\nabla \operatorname{curl}\ \mathbf{v}|^2 \tag{5.12}$$

where $\operatorname{div}\ \mathbf{v} = \partial u/\partial x + \partial v/\partial y$ and $\operatorname{curl}\ \mathbf{v} = \partial v/\partial x - \partial u/\partial y$. This regularizer is modified by replacing the quadratic penalizer and adding two more scalar field ξ and χ which are direct estimates of surface divergence and vorticity, respectively. The new regularizer is given by:

$$\int_\Omega |\operatorname{div}\ \mathbf{v} - \xi|^2 + \lambda f_2(|\nabla\xi|) + \int_\Omega |\operatorname{curl}\ \mathbf{v} - \zeta|^2 + \lambda f_2(|\nabla\zeta|) \tag{5.13}$$

5.2. Fluid flow estimation on infrared images of the water surface

The estimation of surface velocities from a sequence of infrared images of the water surface can be challenging. One reason is that infrared data is different in comparison to the images for which most commonly used algorithms are developed. Clearly, algorithms designed for the motion estimation of fluid flow are the right choice but most fluid flow applications are optimized for satellite images with a large resolution and low noise.

In the infrared images used in this thesis, velocities of different magnitudes occur. There can be large displacements, especially for high wind speeds but important for the characteristics of near surface turbulence are relatively small velocity variations especially in cross wind direction. The images have a low resolution but high noise levels. Variations of brightness occur, e.g if surfactants are present on the surface and also due to reflections from the roof of the channel.

The velocity estimation is thus required to deal with fine scale structures and accurately image surface divergence at the same time. This indicates that both, cross correlation and global optic flow approaches with a Horn and Schunck regularizer, are not suitable. Here, a global optic flow approach with a regularizer which is able to cope with surface divergence was chosen over an alternative Lucas-Kanade approach, because of advantages like robustness and the the ability to deal with the aperture problem.

5.2.1. A new regularizer

The chosen algorithm combines the advantages of a robust data term which is not sensitive towards changes in illumination taken from Brox et al. [2004] with a smoothing term which comprises a div curl regularizer taken from Corpetti et al. [2002]. This will be combined with the penelizer funtion $\Psi(s^2) = \sqrt{s^2 + \epsilon}$ which is also employed in [Brox et al., 2004]. The small constant $\epsilon = 0.001$ and ensures that $\Psi(s)$ is convex Brox et al. [2004]. The robust penelizer funtion Ψ allows discontinuities in the flow field.

The total expression is given as an energy functional which has to be minimised. In the following spatial coordinates are given by x and y and respective velocities of the vector field $\mathbf{v}$ are given by u and v and are scalar fields. Spatial derivatives are given by subscript indices, e.g., indices x and y denote partial derivatives in x- and y-direction, e.g., $u_x = \frac{\partial u}{\partial x}$ and $u_y = \frac{\partial u}{\partial y}$.

The integrands, split in data and smoothness terms, are given by

$$
\begin{aligned}
&L_{\text{Data}}(x, y, u, v, u_x, v_y) \\
&\quad = \Psi(|I^1(x+u, y+v) - I^0(x,y)|^2 + \gamma |\nabla I^1(x+u, y+v) - \nabla I^0(x,y)|^2) \\
&\quad \approx \Psi\left(((I_x u + I_y v + I_t))^2 + \gamma\left((\partial_x (I_x u + I_y v + I_t))^2 + ((\partial_y (I_x u + I_y v + I_t))^2\right)\right) \quad (5.14)
\end{aligned}
$$

and

$$\begin{aligned} &L_{\text{Smooth}}(u, v, u_x, v_y, \xi, \zeta, \xi_x, \zeta_y, \xi_y, \zeta_x) \\ &\quad = \Psi(|\text{div } \mathbf{v} - \xi|^2 + |\nabla\xi|^2 + |\text{curl } \mathbf{v} - \zeta|^2 + |\nabla\zeta|^2) \\ &\quad = \Psi\left((u_x + v_y - \xi)^2 + (v_x - u_y - \zeta)^2 + \xi_x^2 + \xi_y^2 + \zeta_x^2 + \zeta_y^2\right) \end{aligned} \tag{5.15}$$

Here the scalar field I denotes the image gray values, in this case the surface temperatures. I^1 and I^0 stand for the first and second image in a time sequence. The parameter λ is an additional parameter to scale the impact of the gradient constancy condition. The suggestion of two additional scalar fields was adopted from Corpetti et al. [2002] as it reduces the order of Euler-Lagrange equations from fourth to second. ξ and ζ are measures for the divergence and rotation field respectively, which becomes apparent if the terms div $\mathbf{v} - \xi$ and curl $\mathbf{v} - \zeta$ are set to zero. The total energy functional is then given by

$$E(x, y, u, v, u_x, v_y, \xi, \zeta, \xi_x, \zeta_y, \xi_y, \zeta_x) = \int_\Omega (L_{\text{Data}} + \alpha L_{\text{Smooth}}) dxdy \tag{5.16}$$

The minimization is implemented by the Euler-Lagrange equations. The four Euler-Lagrange equations in u, v, ξ and ζ are given by

$$\frac{\partial L}{\partial u} - \frac{\partial}{\partial x}\frac{\partial L}{\partial u_x} - \frac{\partial}{\partial y}\frac{\partial L}{\partial u_y} = 0 \tag{5.17}$$

$$\frac{\partial L}{\partial v} - \frac{\partial}{\partial x}\frac{\partial L}{\partial v_x} - \frac{\partial}{\partial y}\frac{\partial L}{\partial v_y} = 0 \tag{5.18}$$

$$\frac{\partial L}{\partial \xi} - \frac{\partial}{\partial x}\frac{\partial L}{\partial \xi_x} - \frac{\partial}{\partial y}\frac{\partial L}{\partial \xi_y} = 0 \tag{5.19}$$

$$\frac{\partial L}{\partial \zeta} - \frac{\partial}{\partial x}\frac{\partial L}{\partial \zeta_x} - \frac{\partial}{\partial y}\frac{\partial L}{\partial \zeta_y} = 0 \tag{5.20}$$

In the following the outer derivative of the Ψ function will be shortened to

$$\Psi'(...)_{\text{Data}} = \Psi'\left(((I_x u + I_y v + I_t))^2 + \gamma\left((\partial_x(I_x u + I_y v + I_t))^2 + ((\partial_y(I_x u + I_y v + I_t))^2\right)\right) \tag{5.21}$$

for the data term and to

$$\Psi'(...)_{\text{Smooth}} = \Psi'\left((u_x + v_y - \xi)^2 + (v_x - u_y - \xi)^2 + \xi_x^2 + \xi_y^2 + \zeta_x^2 + \zeta_y^2\right) \tag{5.22}$$

for the regularizer. This gives the four Euler-Lagrange equations, for u and v

$$\Psi'(...)_{\text{Data}} \left(I_x(I_x u + I_y v + I_t) + \gamma \left((\partial_{xy}(I_x u + I_y v + I_t))^2 + ((\partial_{xx}(I_x u + I_y v + I_t))^2\right)\right) + \alpha\ \Psi'(...)_{\text{Smooth}}(u_{xx} + u_{yy} - \xi_x - \zeta_y) = 0 \tag{5.23}$$

$$\Psi'(...)_{\text{Data}} \left(I_y(I_x u + I_y v + I_t) + \gamma \left((\partial_{xy}(I_x u + I_y v + I_t))^2 + ((\partial_{yy}(I_x u + I_y v + I_t))^2\right)\right) + \alpha\ \Psi'(...)_{\text{Smooth}}(v_{xx} + v_{yy} - \xi_y - \zeta_x) = 0 \tag{5.24}$$

and for ξ and ζ

$$-\ \Psi'(...)_{\text{Smooth}}\ (u_x + v_y - \xi) - \Psi'_x(...)_{\text{Smooth}}\ \xi_{xx} - \Psi'_y(...)_{\text{Smooth}}\ \xi_{yy} = 0 \tag{5.25}$$

$$-\ \Psi'(...)_{\text{Smooth}}\ (v_x - u_y - \zeta) - \Psi'_x(...)_{\text{Smooth}}\ \zeta_{xx} - \Psi'_y(...)_{\text{Smooth}}\ \zeta_{yy} = 0 \tag{5.26}$$

The derivatives are discretized using a second order gaussian derivative mask which yielded a stable convergence. The linearized equations are solved via successive over-relaxation (SOR). The relaxation parameter was chosen as 0.5 to stabilize the convergence process. The iteration scheme comprises three outer iterations and 35 inner iterations, in which u and v are computed first and subsequently the auxiliary scalar fields ξ and ψ. This makes the convergence process relatively slow (approximately 60 seconds per image pair).

5.2.2. A robust two step algorithm

Large displacements and high noise levels are problematic if only a second order regularizer is employed. One solution is to combine two different regularizers, one for large translational movements and in a second step small scale divergent and rotational movements. This approach takes advantage of the theory of affine motion models [Haussecker and Spies, 1999]. The principal procedure is described in Figure 5.2.2.

Starting from two subsequent infrared images, an optic flow approach according to Equations 5.7 to 5.9 is performed on five steps of the gaussian pyramid with a scaling factor of 0.9 and a warping step in between. Due to high noise levels the lowest level on which the velocities are computed is approximately half the original image size. Above this scale any flow estimation is considerably perturbed due to noise. As suggested by Sun et al. [2008] a median filter with a filter size of [5,5] is applied between each warping step.

The result is a very smooth flow field and represents the translational component only, as divergence and rotation are reduced to nearly zero. Based on this translational motion another warping step is performed. This means that nearly all differences between the warped image and the original image is caused by small scale divergent and rotational flow.

This last flow estimation is performed by the algorithm suggested in the previous section as it takes full advantage the second order div curl regularizer. In a final step both components

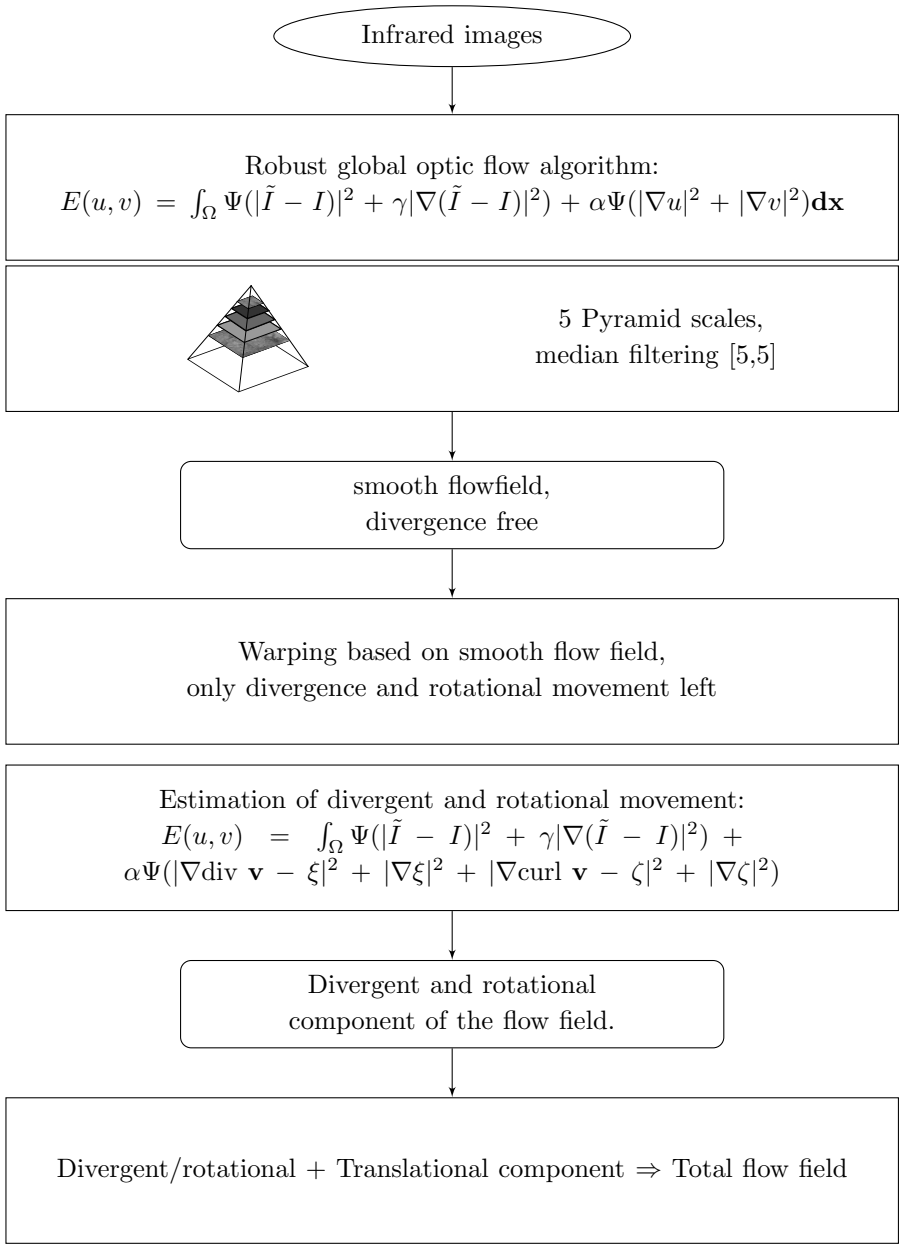

Figure 5.1.: Flowchart of the procedure of the fluid flow estimation from infrared images of the water surface. The two main steps are first, the estimation of a smooth flow field, the translatorial component, based on a traditional smoothing function and second, the application of the div-curl regularizer to determine the divergent and rotational components.

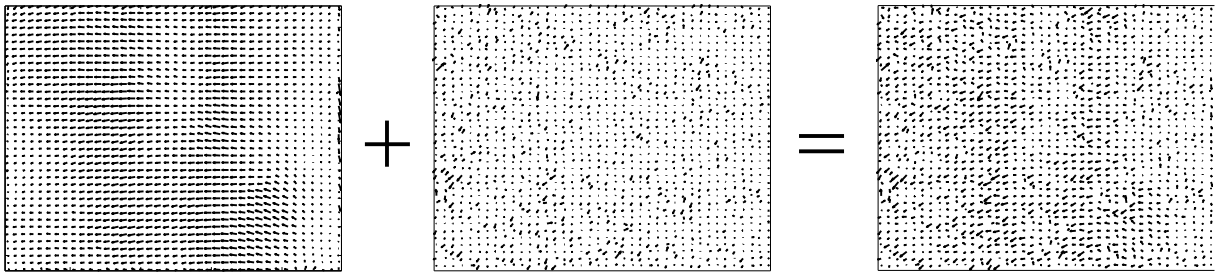

Figure 5.2.: Estimation of the total flow field as a composition of the translational component estimated with a large smoothing parameter and the surface divergent and rotational component in a second step. Together they form the total estimated flow field.

are added to the total flow field that exhibits clearly a translational component but also highly divergent elements.

This is shown in Figure 5.2. The left figure shows the translational component estimated with a large smoothing parameter, in the middle the surface divergent and rotational component is shown and finally on the right the total estimated flow field.

5.2.3. Parameter estimation and performance comparison

All global optic flow approaches depend heavily on the right choice of parameters. Also, the optimal choice of a parameter can vary considerably depending on the image sequence [Brox, 2005].

As a measure for the quality of the estimated velocity field, the second image is warped based on the estimated velocities. In the case of a perfect result the difference between the warped image and the first image should be close to zero (zero without any noise). Therefore, the root mean square of the difference between warped and original image was chosen as a quality controlling parameter.

In the robust algorithm by Brox et al. [2004], also employed in the first step of the velocity estimation, two parameters, the smoothness parameter α and the gradient constancy controlling parameter γ, have to be determined. The minimum was determined in the two dimensional parameter space and is $\alpha = 9.4$ and $\gamma = 24.2$, compare Table 5.1.

In the combined approach shown in Figure 5.2.2 a higher value of α gave better results and also supports the division into the translational part and a divergent and rotational part better. The error for the smoothing parameter $\alpha_{\mathrm{div-curl}}$ increases rapidly for increasing values of alpha. A minimum is found at the rather low value of $\alpha = 0.0001$. This may seem low but also ensures that the estimation in large parts is based on the data term and therefore on the temperature field and no distortion of the velocity field is caused due to the regularizer itself.

A comparison of the root mean square error between the classical regularizer and the two step algorithm that includes surface divergence shows a considerable improvement for the div-curl regularizer. Not surprisingly, as surface divergence is a major feature of the flow.

Table 5.1.: Comparison of the results of the velocity estimation from the standard Horn and Schunck smoothness regularizer and the second order div curl regularizer. The rms error is the root mean square of the original image and the warped image based on the estimated velocity field. α is the smoothness parameter for the conventional smoothing term, $\alpha_{\mathrm{div\ curl}}$ is the smoothness parameter for the div-curl regularizer.

Regularizer	rms error	α	γ	$\alpha_{\mathrm{div-curl}}$
$\lvert\nabla\mathbf{u}\rvert^2 + \lvert\nabla\mathbf{v}\rvert^2$	5.5	9.4	24.2	
div-curl	4.4	32	24.2	0.0001

5.3. Active Thermography as a solution to the aperture problem associated with optical flow

A heated area on the water surface that can be clearly seen in the infrared data can be used as a tracer for the drift velocity. This technique was chosen as a complementary technique to validate surface velocities determined from the optical flow based scheme, described in the previous section. The aperture problem prevents the accurate velocity estimation across the smallest of surface eddies. The reason is that the temperature gradient within the eddy appears static even though it is caused by the continuous cooling of water parcels flowing in cross wind direction. The great advantage of the active technique is that it follows a very different principle and provides very accurate but sparse information of the velocity at a certain position. The technique is already described in my Diploma thesis Schnieders [2011].

The detection of the heat patch is performed by setting a temperature threshold. The threshold is selected from the variance of the mean water temperature, a three σ interval is chosen. This ensures that the total area of the heated patch is detected but also leads to the wrong detection of single warm pixels. A straight forward solution is to discard of all areas of less than five pixels. After this step the heat patch is the only remaining object and can easily be tracked. The position of the center of mass of each sheared and advected structure on the water surface is tracked for every time frame.

False detections occur if a warm reflection, usually the camera itself, happens to be to close to the position of the real structure. As these reflections often move in wind direction due to traveling waves one means to separate them from the heat patch is by their velocity which corresponds rather to the phase velocity of the wave than the water velocity of the heat patch. This happens most often at low wind speeds and leads to wrong velocities. Those can clearly be seen as outliers in the determined velocities. These outliers resulting from wrong detections are identified by their deviation from the mean by more than three sigma (standard deviation) and are thus removed.

The velocities in x- and y- direction are determined via a third order accuracy derivation of the x- and y- positions respectively.

5.4. Validation of estimated velocities from simultaneous active and passive measurements

Validating the estimated velocities is crucial for the further analysis that in part builds up on the velocity estimation but difficult due to the missing ground truth. The comparison of two independent methods is one way to still be able to test the accuracy of velocity estimation. The simultaneous measurement of active and passive Thermography sequences provides the opportunity to test both methods and especially the optical flow based velocities, as active tracking has been shown to provide very accurate (though sparse) velocity values [Gutsche, 2014; Schnieders, 2011].

Due to the different nature of both techniques, velocities are not directly comparable, as active tracking gives a velocity of the center of mass of a heat patch while optical flow provides a pixel wise estimation of a dense flow field. Also, even though the measurements are taken simultaneously, the results of the optical flow estimation are inaccurate at the position of the heat patch due to diffusion and, more important, not representative for the otherwise employed standard passive Thermography. Therefore, to allow the direct comparison an area was chosen close to and of the same size as the heated patch shifted in cross wind direction. The mean over this area is roughly comparable to the velocity of the center of mass of the heat patch, especially if the velocity field is modulated by distinct surface waves.

5.4.1. Comparison of active and passive methods

Figure 5.3 shows surface velocities estimated from active tracking (red) and optical flow with a div curl regularizer (blue) and the standard smoothness term (black). Horizontal, along wind, velocities are shown on the y-axis, the x-axis denotes time. Along wind surface velocities are clearly shaped by surface waves (compare Peirson et al. [2014]; Schnieders [2011]), with highest velocities at the wave crest and lowest in the trough. This spatial and temporal velocity variation is especially difficult for standard optical flow algorithms because the characteristic feature of waves is the production of surface divergence.

The standard smoothness assumption clearly leads to a considerable underestimation of the peak wave velocities. While scattering is a little higher for the div curl regularizer due to the weakness of the applied constraint, it clearly captures the wave modulation of surface velocities better than the commonly used smoothness assumption. This is a good example in which the standard regularizer $|\nabla \mathbf{u}|^2 + |\nabla \mathbf{v}|^2$ fails to estimate accurate flow fields. The reason is the spatial and temporal variation of surface velocities and the associated surface divergence in the trough area of the wave violates the smoothness assumption and is therefore dampened in the minimization process. The div curl regularizer is thus far better suited to deal with the highly divergent flow field.

In comparison to the active technique passive velocities estimated with a div curl regularizer exhibit substantial noise. However, the advantage of the optical flow field is the estimation of

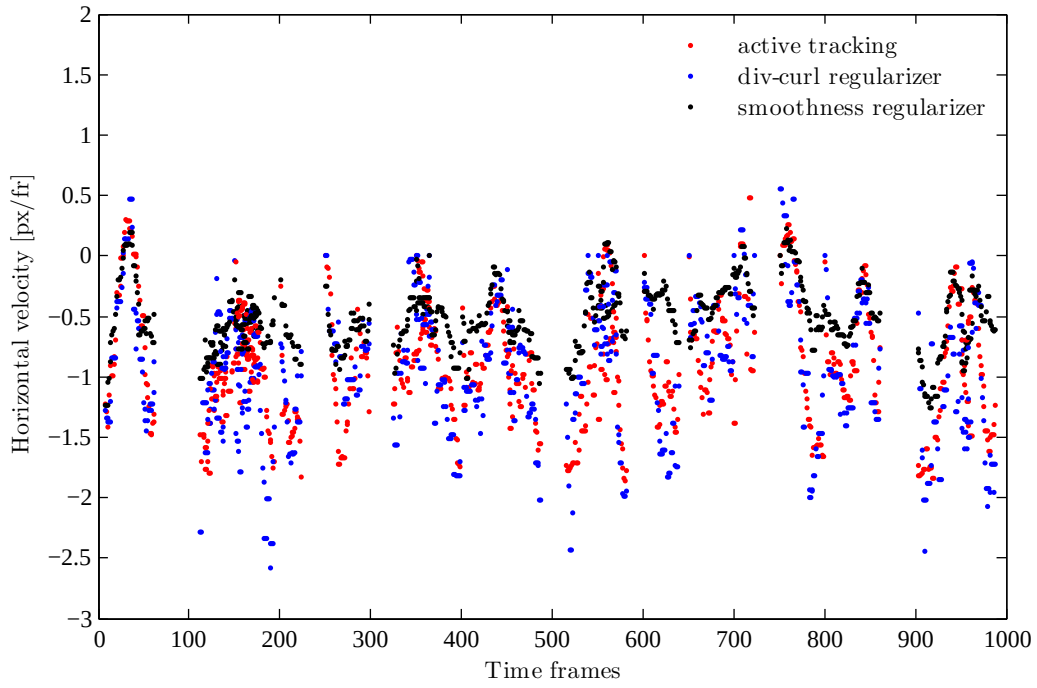

Figure 5.3.: Surface velocities estimated from active tracking (red) and optical flow with a div-curl regularizer (blue) and the standard smoothness term (black). The standard smoothness assumption clearly leads to a considerable underestimation of the peak wave velocities.

dense flow field so scattering could be considerably reduced by averaging in time and space.

5.4.2. Error estimation

To be able to give an upper bound of the expected error of the velocity estimation, the root mean square difference between both techniques is calculated frame by frame and subsequently averaged. This measure is used as an approximate error estimation of the surface velocity results and is represented in the error bars in Figure 5.4.

In Figure 5.4 the results of the comparison of averaged velocities for every wind condition are shown. Open circles in blue and red show velocities estimated via the Brox-Corpetti combined algorithm in cross wind (blue) and along wind (red) direction. For comparison, small dots represent velocities estimated from the Brox algorithm. Cross wind velocities seem to be more accurately estimated by the optical flow algorithm than along wind velocities. This is in a way surprising because due to the aperture problem fluid movement within the small scale streaks cannot be resolved. A possible explanationis that the larger scale dynamics of the surface dominates over small scales. As a result the small scale structure act as tracers in the larger scale flow. This indicates that the errors of the flow estimation from optic flow due to the aperture problem are relatively small and velocities estimated via this method provide reliable estimates.

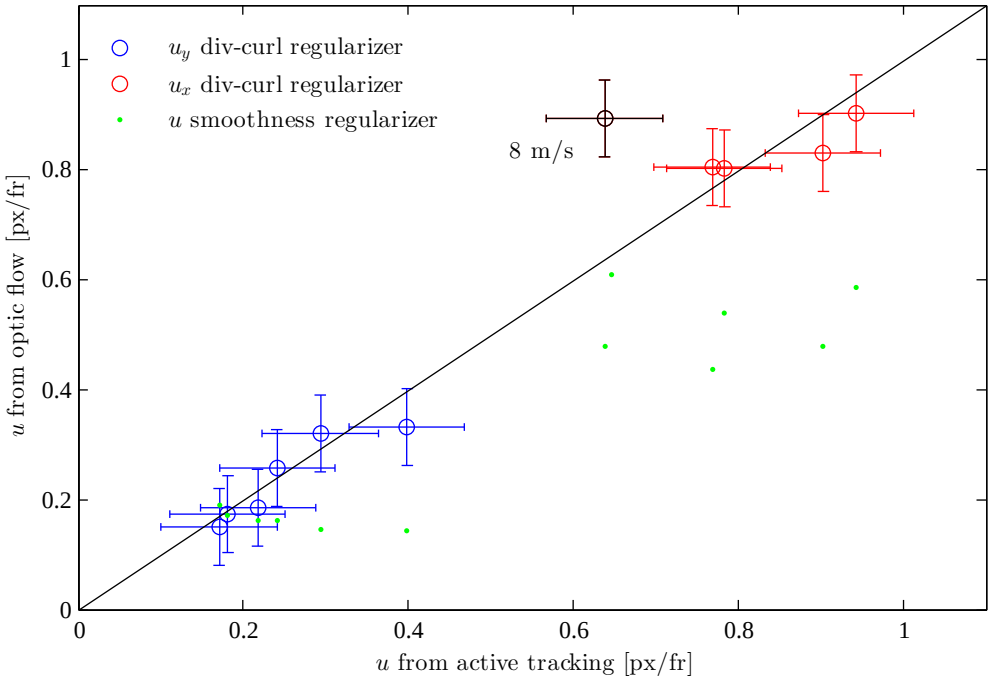

Figure 5.4.: Comparison of velocity estimates from optical flow (y-axis) and active tracking (x-axis). Open circles in blue and red show velocities estimated via the Brox-Corpetti combined algorithm in cross wind (blue) and along wind (red) direction. For comparison, small, green dots represent velocities estimated from the Brox algorithm, with a standard smoothness constraint.

The along wind velocities are inaccurate especially in one case, which is the highest wind speed condition. At high wind speeds and frequent microscale breaking, large parts of the surface temperature pattern are frequently wiped out which makes velocity estimation relatively inaccurate. This equally affects optical flow by the removal of small scale "tracer" structures and active tracking based techniques due to the removal of the heat patch.

At the low wind speeds and in the presence of surfactants, few surface waves are present. As a result, reflections of the opening in the channel roof through which the camera and the laser are looking appear on the water surface. These reflections, if not broken up entirely by the sloped surface, travel with the velocity of capillary waves. This is considerably faster than the water surface. This means that in the flow field estimation from optical flow the impact of those small waves may be overestimated and the averaged velocities would consequently be too high. In the passive thermographic measurements on which the following analyses are based, special care was taken to insulate the channel openings and reflections are avoided.

6. Classification of the surface temperature pattern

The classification of objects is one of the core topics in image processing and finds applications in a wide variety of fields, from the segmentation of cells in neurobiology to identifying pedestrians in driving assistance systems. Here, the footprints of different turbulent processes in infrared images are analyzed. A classification of connected areas of up- and down-welling, allows for the further analysis of a specific kind of process, e.g., the analysis of the turbulent cell size. In the following, suitable techniques for the segmentation of the surface temperature pattern will be described.

6.1. Analysis of the spatial scales of the footprints of near surface turbulence

The goal is to achieve a full segmentation of the surface heat pattern, e.g., classifying each pixel as part of a (cold surface) "streak" or "no streak". Therefore, a classification method is needed based on features of the image. The easiest method would be a simple temperature threshold, classifying pixels colder than this threshold value as "streak" and those warmer as "no streak". Due to temperature variations on several scales a simple temperature threshold is not sufficient to achieve a segmentation of the surface heat pattern (see Figure 6.2). The same applies to any other feature such as gradients or orientation. This means a classification can only work if based on several different features.

6.1.1. Pixel based segmentation

Our approach to this challenge is a machine learning based algorithm which uses a random forest classifier, as implemented in the software package Ilastik by [Sommer et al., 2011]. The classification does not rely on one feature (for example temperature) but several features which is a big advantage in the case of the highly variable surface heat pattern. The second advantage is the high flexibility of this semi automated segmentation. A classifier is "taught" by the user which combination of features most probably describes a class ("streak" or "no streak") and later uses this training data to classify pixels. This means a small number of structures are labeled manually and then large amounts of data are processed automatically.

The first step of the analysis is to choose appropriate features that describe the observed heat pattern, obviously such as gray value, edge and orientation. Then, the corresponding scale on which the filters operate is chosen and these are the features on which the random forest classifier is based. M is the number of features which are chosen to describe the given problem. This means that for every image there are M images that contain the values of the selected features at every pixel.

Random forest

A random forest [Breimann, 2001; Criminisi et al., 2012; Hastie et al., 2009] is a classifier that consists of an ensemble of decision trees. A decision tree is created by Ilastik after the end of the training session. During the training session, the user manually labels a set of N pixels. To every labeled pixel belongs a number of feature values. This is called a feature vector, that contains the values of the previously selected features at the location of the labeled pixel. The growth of a decision tree can be described by the following steps:

- During the training a certain number N of feature vectors has been created. From these feature vectors now $n << N$ samples are chosen randomly (with replacement) and represent the so called bootstrap sample.
- Now, a number of features $m << M$, where M is the total number of features, is randomly selected to divide the bootstrap sample into two subsets.

  The next step is to select randomly m features ($m << M$ and M the total number of features). These m features are used to divide the tree into two sections, the first knot is created.
- The tree continues to grow by repeating this step over and over again until all the pixel in one branch belong to one class.

The so-called random forest consists of a number of decision trees and their average "vote" is decisive for the classification of a pixel. Once the random forest is generated from the training images it can be used to classify all other (unlabeled) images. So every image follows the structure of the constructed random forest.

The result is a pixel-wise classification of the surface heat pattern. Therefore, no spatial patterns or global correlations are accounted for in the probability maps.

As a measure of variable importance the maximum mean Gini increase was used, which is a measure of the importance a variable has on the decision in each node of a decision tree. The comparison of Gini gains for low wind speeds yields the feature "orientation" based on the the structure tensor and entries of the Hessian matrix on a scale of $\sigma = 3.5$ as the most important variable. Followed by edges, which is based on eigenvalues of the structure tensor and Hessian matrix as well as gradient filters such as Difference of Gaussians and Laplacian of Gaussian. Finally, the gray value intensity, which is based on a first smoothing on scales of $\sigma = 0.3$ to

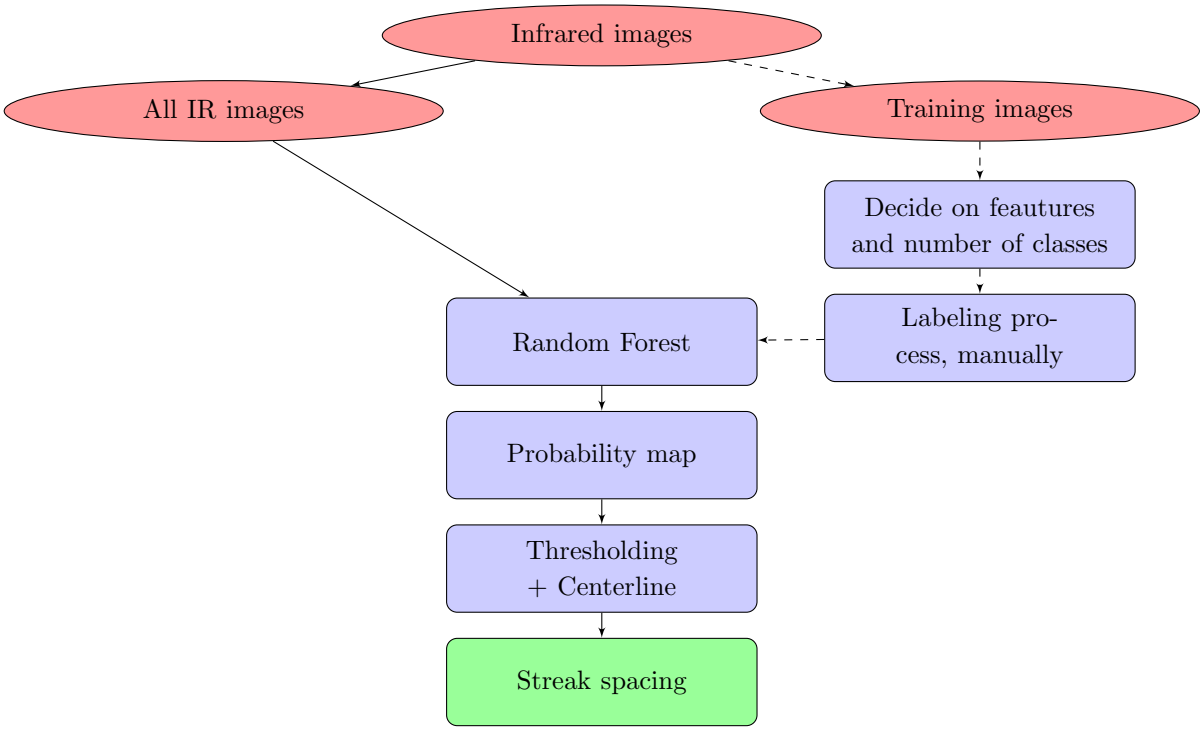

Figure 6.1.: Flowchart of the classification algorithm. The original data set is split into two subsets: statistically independent images for the labeling process and all remaining images. Once a random forest is created, all remaining images can be analyzed.

$\sigma = 3.5$. For higher wind speeds features remain the same but there is a shift to smaller filter scales which corresponds to the visible change of the surface heat pattern to smaller structures.

Data analysis

Four statistically independent images from each recorded condition present the basis of the following training and classification process and were labeled manually. The algorithm was trained independently on the data of the different measurements and subdivided into wind speeds. Cases of clean water and surfactant covered water surface were treated as one condition.

Three distinct classes, “streak”, “warm plume” and “reflexion” (resulting from the cold camera chip surrounded by the camera window), are chosen to describe the surface heat pattern. The result of the classification is a probably map which shows the calculated probability for a pixel of being a “streak” or not (Figure 6.2, column 3).

The quality of the resulting classification has been carefully surveyed. Unfortunately, there is no “ground truth” to which the classification results could be compared. Therefore, cold surface streaks were marked manually and this result was compared to the result obtained during the data analysis for this specific images. This approach showed good agreement and leads to an error of 6.4% wrongly classified pixels at low wind speeds to 15% at high wind speeds. Additionally an optimal probability map of one image was generated by using a very high number of manually

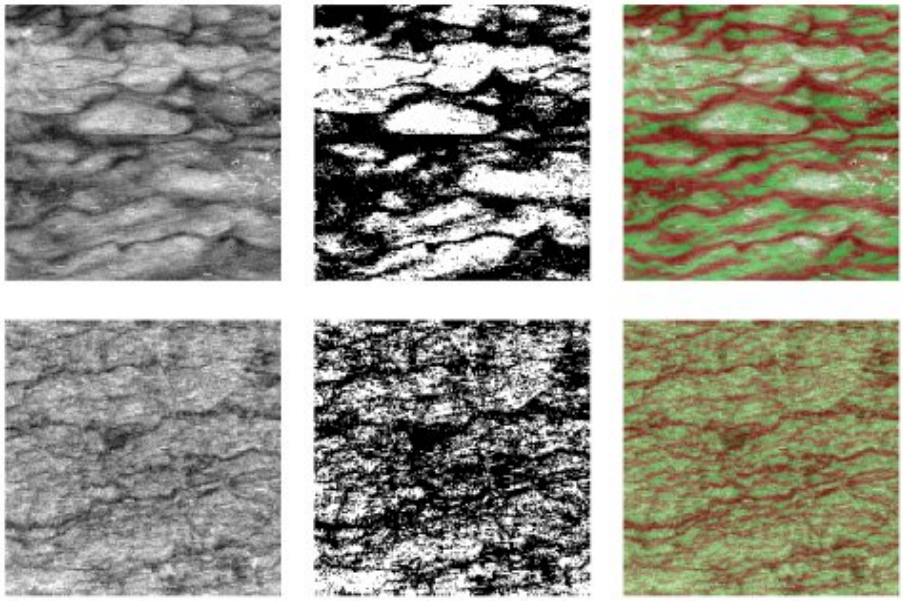

Figure 6.2.: Left column: Infrared images (Aeolotron) of the water surface at two different wind speeds; Middle column: Simple temperature threshold; Right column: Result of the classification process, red: "streak", green: "no streak"

marked pixels and subsequently compared to a classification of the same image with the standard random forest. This leads to an error of 7% wrongly classified pixels at low wind speeds and 10% at high wind speeds. Here, mainly the boundary areas of the streaks cause the error but not the center which determines the spacing. Another source of errors is the variable environment of the water surface and depends strongly on measurement conditions. Under certain conditions (see Section 4.2) microscale breaking waves are present.

6.1.2. Analysis of the streak spacing

Small scale temperature pattern

For the last step of the analysis, e.g., the extraction of the streak spacing, we chose statistically independent probability maps. The streak spacing is determined from the center of one streak to the center of the next on a line in cross wind direction. To ensure that the measured spacings are not spatially correlated as they would be if the spacing was determined from two successive lines, only two lines with a sufficient distance of each of the selected probability maps were picked. The determination of the centerline of the streak is accurate on pixel level and based on the segmented image.

A log normal distribution describes the histograms of measured streak spacings very well. Therefore a log normal function is fitted to the data and its features form important parameters to compare the results for different wind speeds and surface conditions.

In the regime of small streak spacings, irregular edges of the segmented images and wrong detections due to overlapping classes lead to a slightly higher number of very small streak

spacings than expected. Streak spacings of such a small scale have not been observed in the images and are therefore not considered physical. The error is comparatively small and does not disturb the log-normal fit.

In the spilling region of a microscale breaking wave the surface heat pattern is wiped out as surface renewal takes place. In this region no streak spacings are detected. This does not influence the distribution of spacing as incoherent turbulence does not lead to any structures that could accidentally be taken for streaks. However, it leads to gaps that lead to a slight overestimation of very large spacings. For these reasons, the position of the mode was selected as the most reliably feature of the distribution to characterize the streak spacing.

Large scale temperature pattern

Larger scale streaks appear in the infrared images at higher wind stress and are caused by another production mechanism, Langmuir circulation. Therefore, it is important for the analysis to separate the footprints of the two different processes. Larger scale streaks are considerably more stable and have life times of several seconds or more. In a cross section of an image stack, a time space image (see Figure 7.1), those streaks are easily detectable, due to their persistence. Therefore, to analyze the spacing of Langmuir induced streaks the same analysis as for the small scale temperature pattern is performed on time space images of the water surface. Dominant features remain the same, only the scale needs to be adjusted. The streak spacing is determined with the same procedure as described above.

7. Mechanisms defining the dynamic state and thermal pattern of the water surface

Processes relevant in the context of air-sea interaction determine the dynamics of the water surface. In the surface temperature pattern an integrated version of dynamical processes is visualized with an emphasis on locally stable processes. Also the surface flow field provides information about kind and strength of a turbulent process. As a result, the momentary velocity field and the integrated divergence visible in infrared images provide two different views on the characteristic mechanisms. Processes like Langmuir circulation and shear turbulence, for example, act on different timescales than, for example surface gravity waves or turbulence associated with microscale breaking. Therefore, it also depends on the observation method which process appears most pronounced. A comparison between the results of the high temporal resolution surface velocity estimates with infrared images which better represent spatially more stable processes highlights different mechanisms and points towards the respective time scale.

At increasing wind stress and depending on whether surfactants are present or not the water surface is dominated by varying mechanism. In this chapter different turbulent regimes are derived from the surface temperature pattern and the estimated velocity fields. While shear turbulence is clearly visible in infrared images its impact on the surface velocity field cannot be resolved due to the aperture problem. Langmuir circulations and microscale breaking affect both the temperature pattern and the velocity field but are more pronounced in the infrared images while the short timescales let surface waves clearly affect the velocity field but are too short to leave their footprints in the surface temperature pattern.

In Figure 7.1 an example infrared image of 40x40 cm is shown with annotations to illustrate the footprints of shear turbulence and small Langmuir circulations that will be discussed in the following sections. A range of structural scales is visible. Clearly visible small-scale structures are superimposed by larger-scale temperature variations. These larger-scale structures are persistent as shown in the right image of Figure 7.1. The infrared image on the left is a representative sample from a sequence of 1000 infrared images. The right panel in Figure 7.1 shows the temporal development at a set line in the image stack highlighting the larger-scale cold surface streaks that persist throughout the sequence for approximately 16 s.

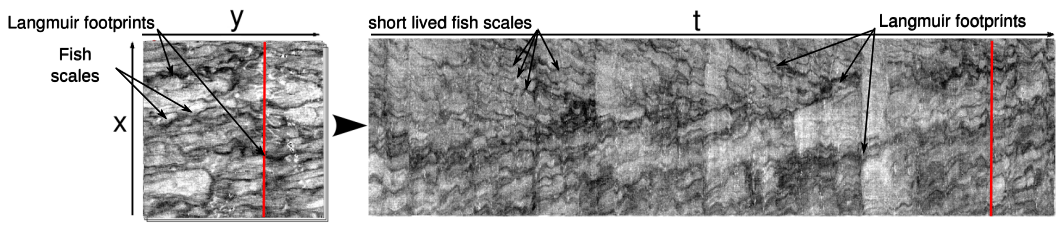

Figure 7.1.: Image from Schnieders et al. [2013]. A stack of infrared images on the left side, taken in the Aeolotron, Heidelberg at a friction velocity of $u^* = 0.34\,\mathrm{cm/s}$, is transformed into the right representation in which the temporal development of structures at a set position is described. Small scale structures in the temperature pattern are called fish scales and are caused by shear turbulence. Larger scale cold streaks are better visible in the time space image and represent the footprints of small Langmuir circulations.

7.1. Dominant turbulent processes at varying wind wave conditions

Representative infrared images of the water surface, taken during the experiments at Aeolotron, 2014, with and without surfactants, are shown in Figure 7.2. The surfactant Triton X-100 lowers surface tension and therefore effectively suppresses capillary waves. The overall roughness of the water surface is considerably reduced, compare Table 4.2. Especially at low wind speeds the slick covered water surface remains entirely smooth with Mean Square Slope (MSS) values below 0.1. With increasing wind speed the gap in MSS values between clean and surfactant covered surface gradually decreases but MSS values stay generally lower (about 20 % at higher wind speeds) [Bopp, 2014]. Thus, the onset of gravity waves occurs at higher wind stress if a surfactant is present.

In Figure 7.2 left column images show a clean water surface while the right column shows surfactant covered images. Wind stress increases from a) to e). The surface temperature is color coded with light areas being warmer than dark areas. The temperature difference in the images is ~ 0.25 K and ~ 0.14 K in the lower and higher wind speed images respectively. The three rows of infrared images are chosen as references to different regimes of the water surface (see Table 4.2).

Starting from low shear and a relatively smooth water surface the wave field progresses to a more developed state in the clean surface conditions but a very smooth surface in the surfactant case. The second row shows images of the water surface under higher shear stress with surface waves clearly present in the clean water case but considerably weaker in the surfactant case. Finally, the third row shows two images with similar wave height values in both the clean surface and the surfactant case and frequent microscale breaking.

In Figure 7.3 time-space infrared images of the water surface are shown, that were taken during the experiments at Aeolotron, Heidelberg. The temporal depiction shows a time slice of the image stack, with time on the x-axes and cross-wind direction on the y-axis. Left images show clean surface conditions, right images show surfactant covered surface conditions. The first row refers to friction velocities of $u^* = 0.7$ cm/s, second row to $u^* = 1.3$ cm/s.

Characteristic cold streaks, the footprints of Langmuir circulations, are visible in all images

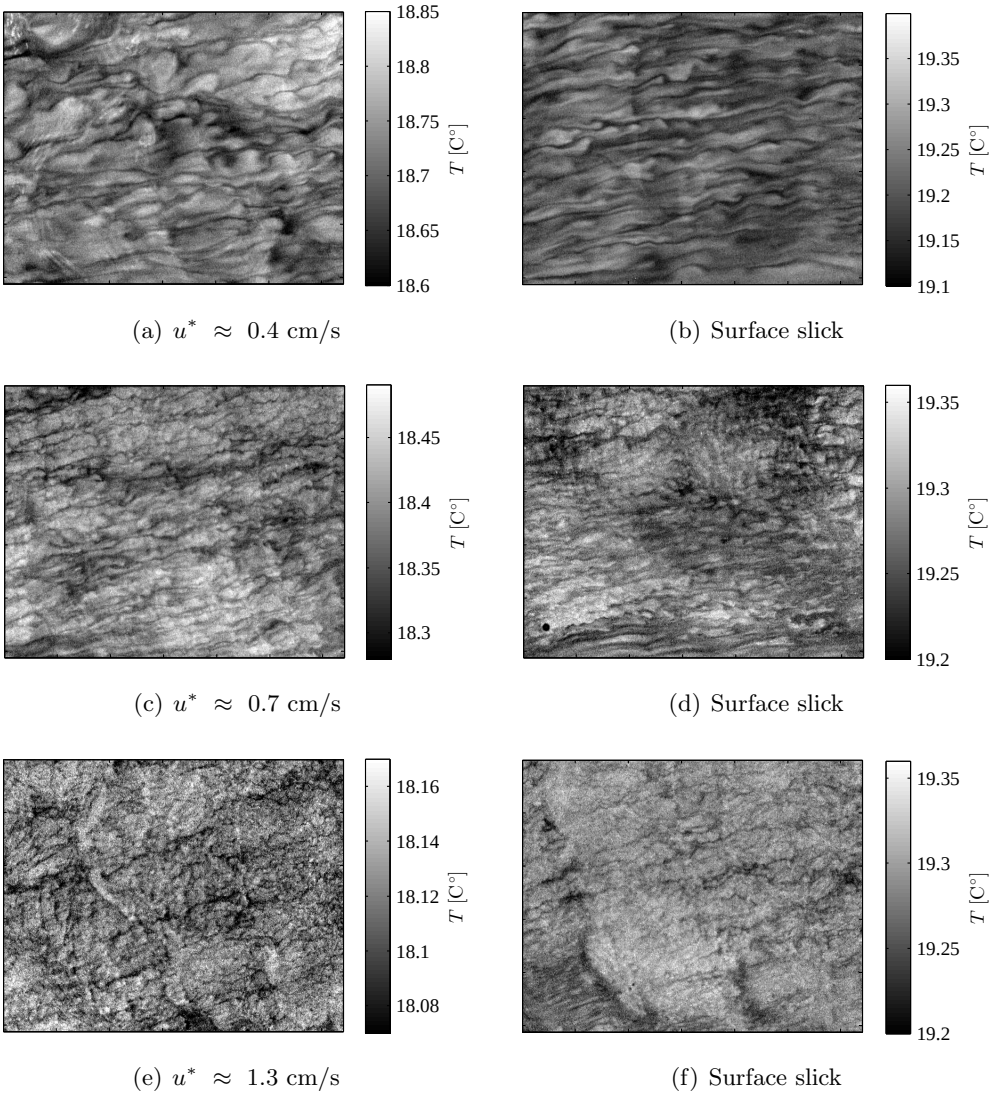

(a) $u^* \approx 0.4$ cm/s (b) Surface slick

(c) $u^* \approx 0.7$ cm/s (d) Surface slick

(e) $u^* \approx 1.3$ cm/s (f) Surface slick

Figure 7.2.: Infrared images of the water surface taken during the experiments at Aeolotron, Heidelberg. Shown is a comparison of infrared images of a clean water surface (left column) and a surface covered by surfactant Triton X-100 (right column). The three rows refer to three different wind speeds. In the first row, no waves were present, in the second row gravity waves were present and in the third row frequent microscale breaking had set in.

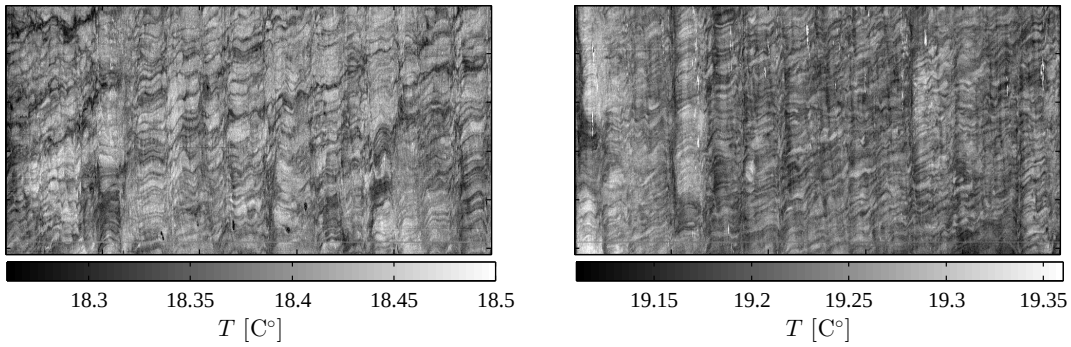

(a) Time space image, clean surface, $u^* = 0.7$ cm/s (b) Time space image, Surface slick, $u^* = 0.7$ cm/s

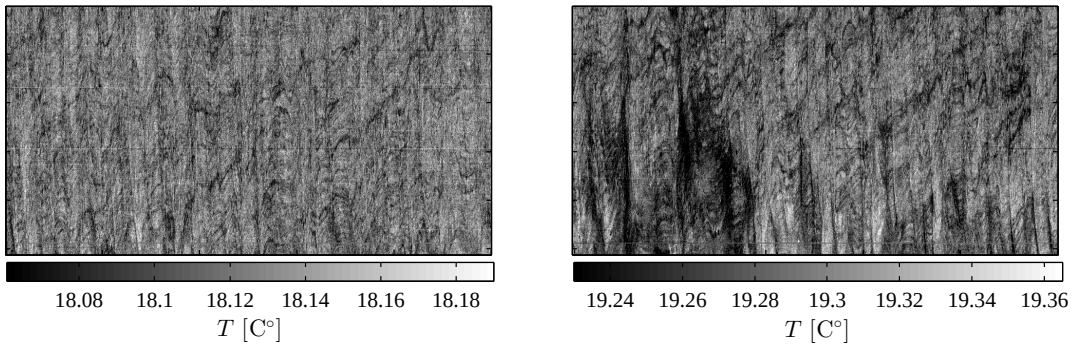

(c) Time space image, clean surface, $u^* = 1.3$ cm/s (d) Time space image, Surface slick, $u^* = 1.3$ cm/s

Figure 7.3.: Time-space infrared images of the water surface taken during the experiments at Aeolotron, Heidelberg. The temporal depiction shows a time slice of the image stack, with time on the x-axes and cross-wind direction on the y-axis. Left images show clean surface conditions, right images show surfactant covered surface conditions. The first row refers to friction velocities of $u^* = 0.7$ cm/s, second row to $u^* = 1.3$ cm/s. In the upper right image no Langmuir footprints are visible in all others characteristic streaks appear. Dark patches arise from accumulation of surfactants at higher wind stress.

but the top right image, Figure 7.3 b). Here, surfactants delayed the development of surface waves. As a result, there is a considerable difference between clean surface and surfactant covered surface in this wind speed regime.

7.1.1. Shear dominated regime

With increasing wind speed, the structures in the temperature pattern clearly change to smaller sizes, which has been described earlier by Handler et al. [2001]; Schimpf et al. [2004]; Schnieders et al. [2013]; Scott et al. [2008]; Tsai et al. [2005]. The characteristic pattern in the images exhibits small structures termed fish-scales by Handler et al. [2001] and Tsai et al. [2005]. In earlier work by [Asher, 1997; Kitaigorodskii, 1984] and recently by [Schnieders et al., 2014; Tsai et al., 2005] it has been suggested that shear stress alone is sufficient for their appearance and it has thus been concluded that those small scale structures are presumably the footprints of

shear induced turbulence [Schnieders et al., 2013; Tsai et al., 2005].

Comparing the left column (clean surface) with the right column (Triton X-100) in Figure 7.2 it becomes evident that the turbulence at the water surface looks relatively similar at low and high wind stress, first and third row, but different in the transition zone in between.

In the first row, at low wind speeds, shear induced turbulence clearly dominates, neither wave breaking nor wave shear coupled turbulence is visible. Both images look very similar and this has been reported previously in Schnieders et al. [2013] where an analysis of the spacing of small scale cold streaks showed that the presence of surfactants did not alter the size of turbulent cells. The similarity of the small scale structures at a clean and and slick covered surface can be seen throughout the range of wind speeds. Given that the prime effect of soluble surfactants is to dampen capillary waves and decrease surface roughness this means that small scale shear induced turbulence is relatively insensitive to surface waves [Tsai et al., 2005] and wind stress alone is the driving force [Asher, 1997; Kitaigorodskii, 1984].

7.1.2. Langmuir Circulation dominated regime

Clearly wave related larger scale streaks appear, Figure 7.2 c), e) and f), just after the onset of the first gravity waves between $u^* = 0.5$ cm/s and $u^* = 0.7$ cm/s in the clean water case and u^* between 0.8 cm/s and 1 cm/s when the water surface is covered by the surfactant Triton X-100.

At an intermediate wind speed range, starting from approximately $u^* = 0.5$ cm/s in the clean water surface cases and approximately $u^* = 1$ cm/s in the surfactant covered water surface cases, the surface temperature pattern is dominated by larger scale cold streaks. They are responsible for the strongest temperature gradients and are clearly wave related as they only appear after the onset of surface waves, i.e. increasing MSS values and surface elevation, compare Tables 4.2 and 4.1. It has been shown [Caulliez, 1998; Melville et al., 1998; Veron and Melville, 2001] that small Langmuir circulation exist under similar conditions. A comparison of the spacing of these streaks to the spacing of Langmuir Circulation as predicted by the CL II mechanism [Leibovich and Paolucci, 1981] will be discussed later but was done in [Schnieders et al., 2013] and shows a quite good agreement.

At an intermediate wind speed range, e.g., in images c) and d) in Figure 7.2, there is a clear difference between infrared images of a clean surface and Triton X-100 covered surface. This becomes more evident when looking at the respective time space images in Figure 7.3 a) and b). These images highlight the life time of a surface structure and exhibit clearly visible stable streaks in Figure a) but not in Figure b). The infrared image of the surfactant covered surface exhibits only the characteristic fish scale patter but shows no signs of any larger scale circulation. This distinct discrepancy between a clean surface and a surface covered by a surfactant layer points towards the generation mechanism of those streaks. Combined with still very low MSS values in the surface slick case this is consistent with the CL II mechanism which describes Langmuir Circulation that evolve through an interaction of shear stress and waves Craik and Leibovich [1976]. At higher wind stress ($u^* \approx 1.3$ cm/s) Langmuir footprints are clearly visible

in the infrared images in Figure 7.2 e) and f) and in the time space representation in Figure 7.3 c) and d).

7.1.3. Microscale breaking dominated regime

At high wind speeds, Figure 7.2 e) and f), again the heat pattern of clean and slick covered surface does look relatively similar even though very different from the first two images. At these wind speeds microscale wave breaking is a dominant process [Zappa et al., 2004]. Mean square slope (MSS) of the surfactant covered water surface have reached similar values to the clean water surface and microscale wave breaking occurs frequently also at the surfactant covered water surface.

At increasing wind speeds these larger scale streaks with a spacing of approximately eight to twelve centimeters become more and more pronounced. For higher wind speeds the circular geometry of the wave channel Aeolotron causes a deflection of the orientation, the cold surface streaks run slightly diagonally.

7.2. Processes shaping the surface dynamics

Surface flow fields provide crucial information about the dynamics of the surface. The surface heat pattern is ultimately an image of surface divergence and convergence. Knowledge of the surface velocity field, thus, provides a very accurate image of the surface state, highlighting processes like gravity waves that do not appear in the infrared images. Infrared imagery with a high time resolution offers the possibility to estimate surface velocities by a non invasive technique and with a high spatial resolution.

However, due to the aperture problem the velocity estimation via optical flow based techniques does not estimate surface flow but changes of temperature gradients in the surface heat pattern. Therefore, any technique based on infrared images will not be able to capture the smallest scale movements. Consequently, the development of the fish scale pattern, clearly created from surface water movement, cannot be resolved, as movements along the eddies are invisible in the IR image. However, it has been shown in Section 5.4.2 that the velocity estimation from optical flow provides reliable results. Larger scale movements are captured well, as will be shown in the following section also because the small scale pattern acts as a tracer.

Surface divergence is an extremely important feature of the the water surface. It provides a link between surface dynamics and its actual impact on transport. All analyses of infrared imagery are based on the visualization of surface convergence and divergence. Surface velocity fields have been determined with a very high temporal resolution. Therefore, surface divergence information has the same temporal resolution and provides a snap-shot of the ongoing processes, in contrast to infrared imagery which always shows an integrated divergence, or rather the time a water parcel has spend at the surface.

Surface divergence has been shown to directly correlate with exchange rates by Banerjee et al. [2004]; Turney and Banerjee [2013]; Turney et al. [2005]. In Veron et al. [2008] surface divergence is shown to closely correlate with the wave field.

Another source of errors in the velocity estimation are the distortions in the infrared images due to wave height which may have a negligible influence on surface velocities but may lead to an over estimation of surface divergence. Furthermore, divergence is derived from the derivatives of surface velocity which means that error propagation increases the error associated with divergence values considerably.

Results of the surface velocity fields

The qualitative results of the velocity estimation via the Brox-Corpetti algorithm are shown in figure 7.2. Rows correspond to increasing wind speeds with friction velocities of $u^* = 0.4$ cm/s, $u^* = 0.74$ cm/s, and $u^* = 1.30$ cm/s in the top, middle, and bottom row, respectively. The left column shows absolute velocities, the middle column shows flow fields, and in the right column the corresponding infrared image is shown. Again the three cases were chosen as representatives of three different regimes, a relatively smooth water surface with capillary ripples, mainly small gravity waves and frequent microscale breaking, that develop with increasing wind stress.

Results of the surface divergence

In figure 7.2 divergence estimates on the same three infrared images as in Figure 7.2 are shown. Wind stress increases from left to right, friction velocities are $u^* = 0.4$ cm/s, $u^* = 0.74$ cm/s, and $u^* = 1.30$ cm/s respectively. Additionally, Figure 7.2 shows from left to right a surface divergence estimate based on one frame of estimated surface velocities. The middle image shows an average over 20 frames of surface divergence which correspond to approximately 0.2 s. The image in the right shows the corresponding average over 20 infrared images. The comparison of the first and third row highlight processes of very different spatial and temporal stabilities.

7.2.1. Non-breaking waves

A comparison of Figure 7.2 to Figures 7.2 and 7.2 shows that in the previously named “Shear dominated” and “Langmuir Circulation dominated” regimes, different processes dominate in the infrared images compared to surface flow fields and correspondingly surface divergence estimates.

Starting from the lowest wind speed case, small wave crests appear in the absolute velocities but not in the infrared image. Clearly visible is also a larger scale streak of higher velocities at the position where a cold large scale streak seems to be in formation in the infrared image.

Looking at the next row, it becomes evident, that in this regime waves are clearly the dominant feature in the velocity image. Comparing this with the infrared image on the other hand shows that here, cold streaks are far more pronounced than the barely visible gravity waves. Comparing

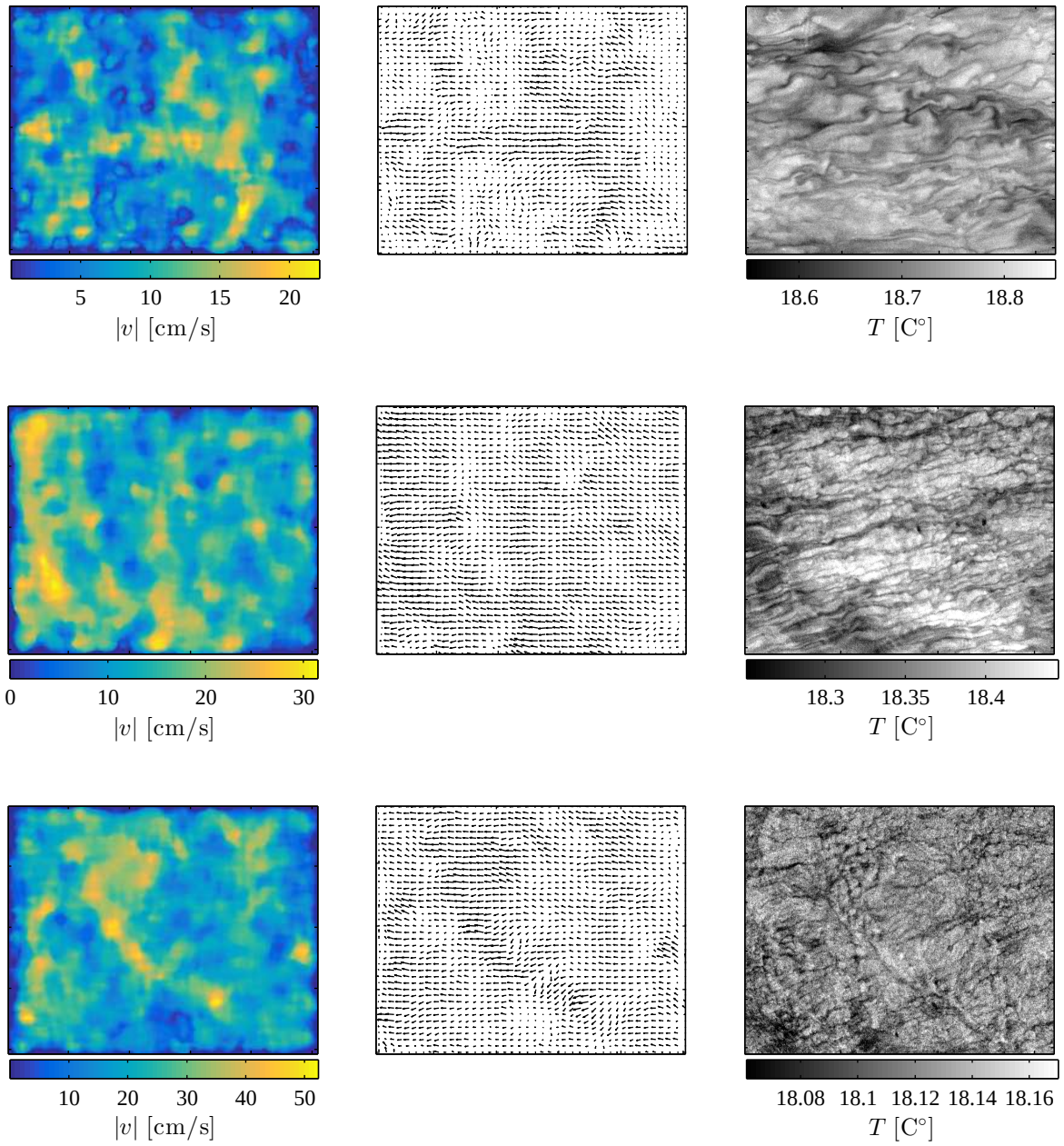

Figure 7.4.: Qualitative results of the velocity estimation, Brox-Corpetti algorithm; Upper row: $u^* = 0.4$ cm/s, Middle row: $u^* = 0.74$ cm/s, Lower row: $u^* = 1.30$ cm/s. Left column shows absolute velocity fields, Middle column shows flow fields, and Right column shows the original infrared image.

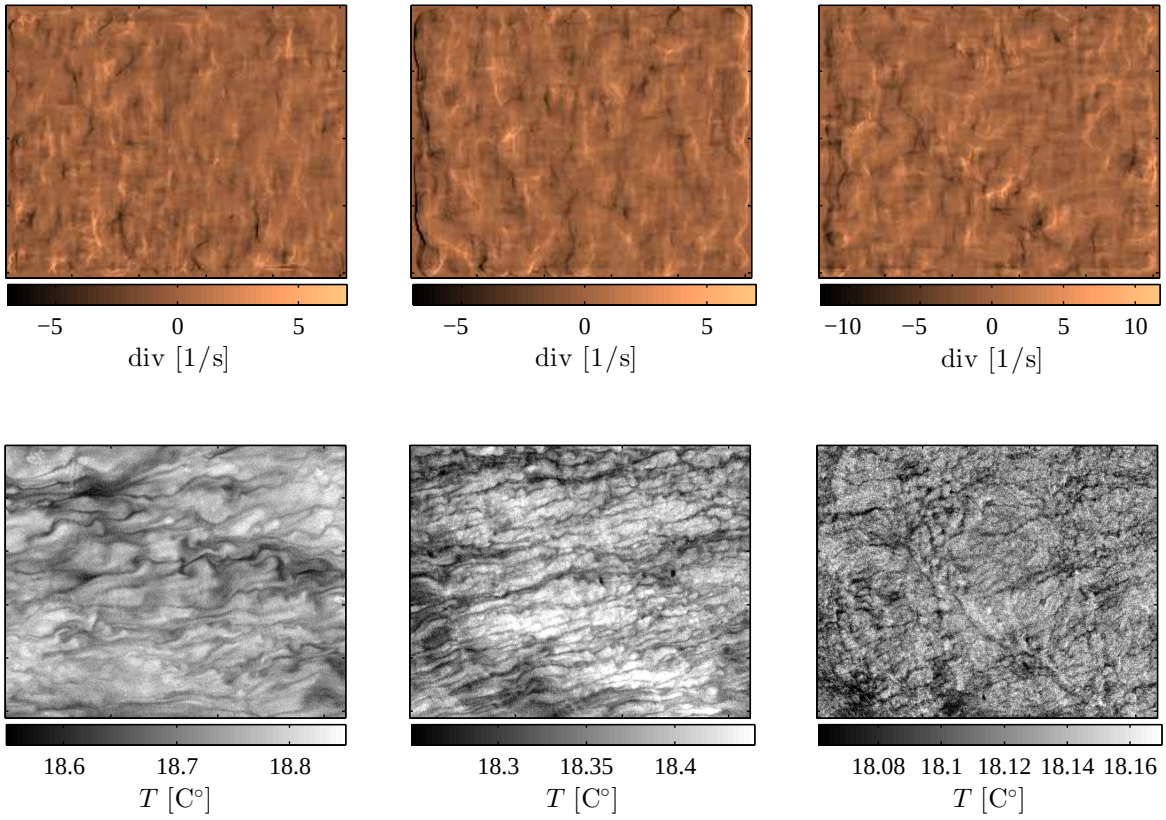

Figure 7.5.: Surface divergence estimates at friction velocities from left to right: $u^* = 0.4$ cm/s, $u^* = 0.74$ cm/s, and $u^* = 1.30$ cm/s. Original IR images are the same as in Figure 7.2. Small waves dominate in the first two images, at low to intermediate friction velocities. In the third image a microscale breaking wave is clearly visible with a spilling region and roll vortices

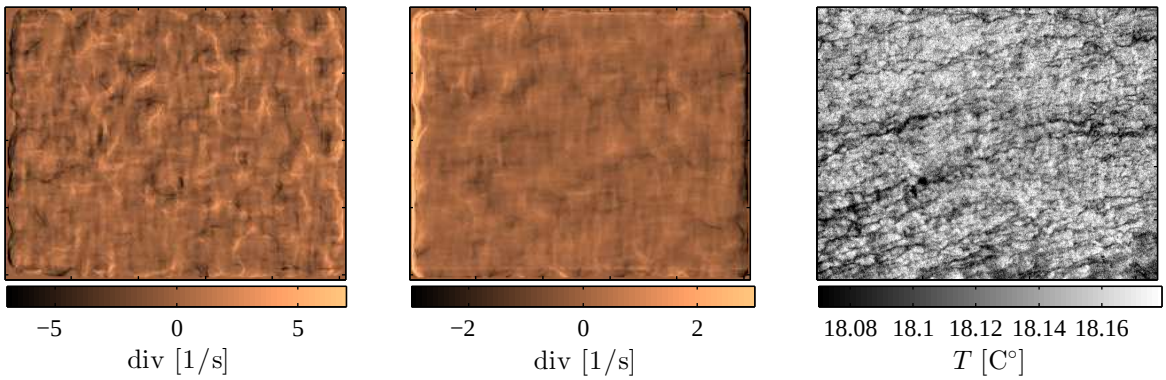

Figure 7.6.: From left to right: Surface divergence estimate at a friction velocity $u^* = 1.0$ cm/s. Same sequence but divergence is averaged over 20 images, 0.2 s. Average of infrared images, in correspondence to divergence sequence. A striking difference in the dominant structures is visible between first and second image, while in the first image small waves are the dominant feature, in the time wise averaged image surface streaks become visible, though on a much smaller divergence scale.

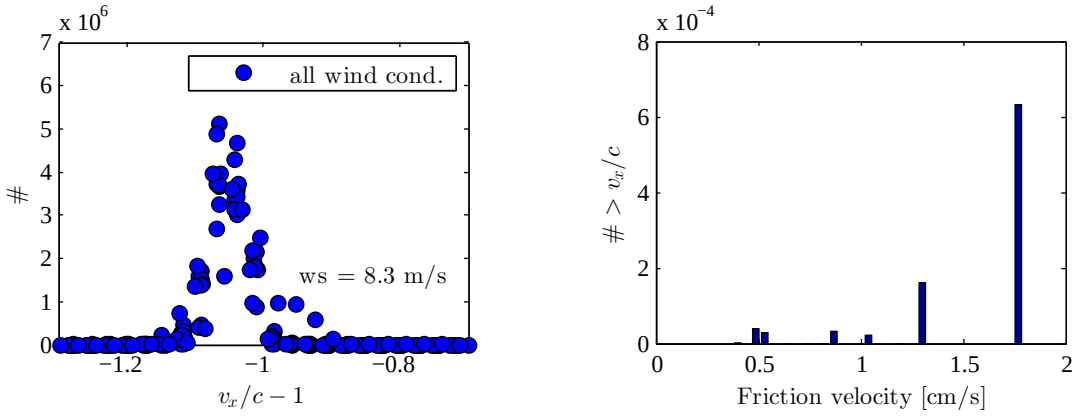

Figure 7.7.: Left: Histograms of with all measured wind speeds overlaid. On the x-axis is $v_x/c - 1$, with v_x being the along wind velocity component and c the estimated phase speed from linear wave theory. Right: Fraction of measured along wind speed velocities that exceed estimated phase speed, $v_x/c - 1 > 0$.

the IR image and the velocity image in more detail shows higher velocities along the position of the cold streaks in the IR image.

The reason for the different characteristic processes in the velocity and the infrared images is that gravity waves are fast moving while infrared images show spatially stable, persistent cross currents that are caused by Langmuir rolls. The question has recently been raised to what extend (personal communication Wu-Ting Tsai) the timescale on which a process acts is an important factor of the impact of the process on exchange rates.

In the two lower wind speed cases (left and middle image in the top row of Figure 7.2) small gravity / gravity capillary waves clearly dominate. This corresponds to the velocity variation already visible in the velocity images. The close correlation of surface waves and divergence has been described by Veron et al. [2008].

Surface waves naturally play a major role in the modulation of surface water velocity in wind direction. In Figure 7.7 the velocity variation due to gravity wave is shown. The relation between wave phase speed and surface velocities is a common characteristic to describe the interaction of waves and surface velocities.

The dominant wave period is determined from the height data via the Fourier transform. Linear wave theory is applied to estimate wave phase velocity. In the left plot in Figure 7.7 histograms of all measured wind speeds are shown over along wind surface velocity normalized by wave phase speed, $v_x/c - 1$. $v_x/c - 1$ is a measure for the acceleration of surface velocity relative to wave phase speed. Nearly all wind speeds exhibit the same behavior, only the highest wind speed case shows higher surface velocities relative to the wave speed. This is very likely related to microscale breaking and will be discussed in Section 7.2.3.

7.2.2. Langmuir convergence and high speed streaks

Langmuir circulations are a defining feature of infrared images of the water surface at low to moderate wind speeds, in the "Langmuir Circulation dominated regime", but do not at first sight appear in the estimated velocity fields.

It is therefore highly interesting to compare the footprints of Langmuir circulations in infrared images to their impact on the surface velocity field. At first glance hardly any trace of any larger scale streak like structures are found, neither in the velocity images in Figure 7.2 nor divergence estimates in Figure 7.2. However, as mentioned earlier, surface divergence and infrared imagery highlight processes on different time scales. Averaged surface divergence estimates in Figure 7.2 try to resolve this conflict by averaging estimated surface divergence rates over 20 frames, 0.2 s. The left image shows the classical surface divergence at a friction velocity of 0.9 cm/s. Small waves clearly dominate. The right image shows an averaged surface divergence sequence starting from the same frame. Now, not surface waves are the dominant feature anymore but clearly visible streaks. This puts even more emphasis on the importance of the time scale of a process and the impact it seems to have or not to have. It also proves that infrared images indeed provide an accurate images of spatially more stable convergence causing processes.

Taking a closer look at the correlation between surface temperature and velocity, Figure 7.8 shows the correlation of along wind surface velocity with surface temperature. In figure 7.8 the bin averaged surface velocity is plotted against surface temperature, open circles show the along wind component, crosses the cross wind component of the velocity field. Friction velocities are from top left to bottom image 0.4 cm/s, 0.74 cm/s, and 1.3 cm/s, respectively. As the here presented data is bin averaged, error bars are larger towards the boundaries of the temperature interval.

Even though surface temperature is a relatively rough indication of surface convergence (compare 7.2) there seems to be a clear correlation between surface velocity and temperature in all cases. Cold surface areas thereby move considerably faster in wind direction than warm areas. This can be observed at a range of wind speeds and confirms (for example Melville et al. [1998]) that cold streaks are indeed high speed streaks. This relationship is most pronounced in the lower wind speed case. This supports the findings in section 7.1.1 and 7.2 that in this regime cold streaks are the dominant process and small surface waves play a smaller role both in the transfer of heat and also, correspondingly, in the surface velocity field. However, as wind speed increases, noise levels also increase but along wind velocities continue to be clearly higher in cold, convergence areas.

The opposite trend, though very weak, can be observed in the cross wind velocity component. Here, highest velocities appear at the highest temperature values. In correspondence with the eddy renewal model this indicates that high cross wind drift velocities appear just after the upwelling process.

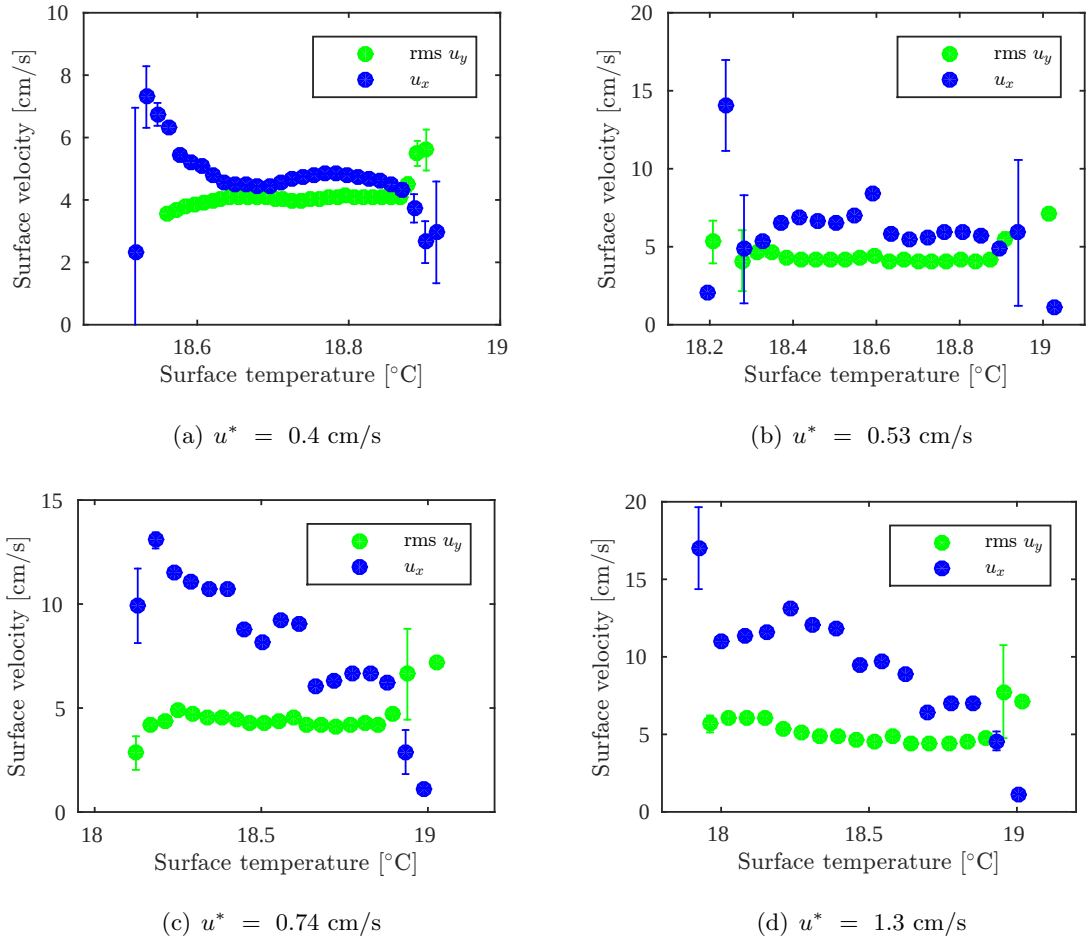

Figure 7.8.: Bin averaged surface velocities over surface temperature. Open circles show along wind velocity components, stars show root mean square of cross wind velocities. Friction velocities are 0.4 cm/s, 0.74 cm/s, and 1.3 cm/s.

7.2.3. Breaking waves and roll vortices

Microscale breaking is a process which is equally dominant in infrared and velocity images. In the bottom row in Figure 7.2 at high wind speeds and clearly visible micro scale breaking in the IR image, also the velocity image is dominated by the breaking wave. The crest area is clearly visualized in the velocity image as an area of accelerated surface water which corresponds to the characteristics of a breaking waves [Banner and Peirson, 1998; Peirson, 1997].

Also the surface divergence (top right image in Figure 7.2) shows all characteristics of a microscale breaking wave. The microscale breaking event in the third image is clearly captured with a subduction area and the adjacent spilling zone of the wave. Interestingly, surface streaks in the spilling region of the wave are also clearly visible. It is not quite clear whether these are of the same kind a the persistent cold streaks that have been referred to as "large scale streaks" or small Langmuir circulations earlier. Handler and Zhang [2013] describes similar streaks on microscale breaking waves and it has been suggested Handler and Zhang [2013] that

wave breaking alone creates this kind of roll vortices. However, they seem to create surface divergence of the same magnitude as that of the wave breaking itself, thereby indicating that both processes (microscale breaking and roll vortices) act on a similar scale in terms of impact on transfer processes but also on a similar time scale.

Microscale breaking waves have the indisputably highest influence on heat and gas transfer at moderate wind speeds Peirson et al. [2014]; Zappa et al. [2004]. One important feature of microscale breaking is the spilling region at the wave crest which causes surface renewal of a relatively large area and thereby enhances transport. The spilling region of a microscale breaking wave is accelerated until surface velocities reach the traveling speed of the micro scale breaking wave.

The right plot in Figure 7.7 shows the number of pixels in the velocity images for which $v_x/c - 1 > 0$. Microscale breaking waves have been shown [Peirson et al., 2014; Schnieders, 2011] to accelerate surface fluid to the phase velocity of the microscale breaking wave. As a result $v_x/c - 1$ would be equal or larger than zero. The histogram in Figure 7.7 now shows that an increasing number of pixel reaches that value in the two highest wind stress conditions. This indicates that microscale breaking is frequently occurring at friction velocities of 1.3 cm/s and higher. This might be an explanation of the higher surface velocities in relation to the phase speed in the left figure only at the highest wind speed case The omnipresence of microscale breaking that was seen in the infrared images and the associated exhilaration of the surface fluid might cause generally higher velocities. On the other hand, the estimation of wave phase speed from linear wave theory is not very accurate, especially for microscale breaking waves. So it might also well be that the frequent microscale breaking causes a stronger deviation of the actual phase speed from the estimated one than in the other cases. However, the extreme exhilaration of surface fluid is in any case a clear indication of ongoing microscale breaking.

7.2.4. Comparison of the impact of surface processes on surface temperature and surface divergence

A comparison between the impact of surface processes on surface temperature and surface divergence is shown in Figure 7.9. Surface divergence over surface temperature is shown at four different friction velocities from top left to lower right images, 0.4 cm/s, 0.53 cm/s, 0.74 cm/s, and 1.3 cm/s. Gray symbols denote individual data points of 100 infrared images and corresponding velocity estimates. Black circles represent bin averages of this data, hence averaged surface divergence values on the right axis are considerably smaller than the total range on the left axis. Therefore, error bars become large towards the ends of the distribution because the mean is calculated from fewer data points.

At low wind stress, $u^* = 0.4$ cm/s no significant correlation between surface divergence and surface temperature is visible. Even though Figure 7.8 showed, that high speed streaks are in formation at the wind speed, this results corresponds to the fact that neither the infrared images nor in the surface divergence images showed any distinct footprints of Langmuir circulations or

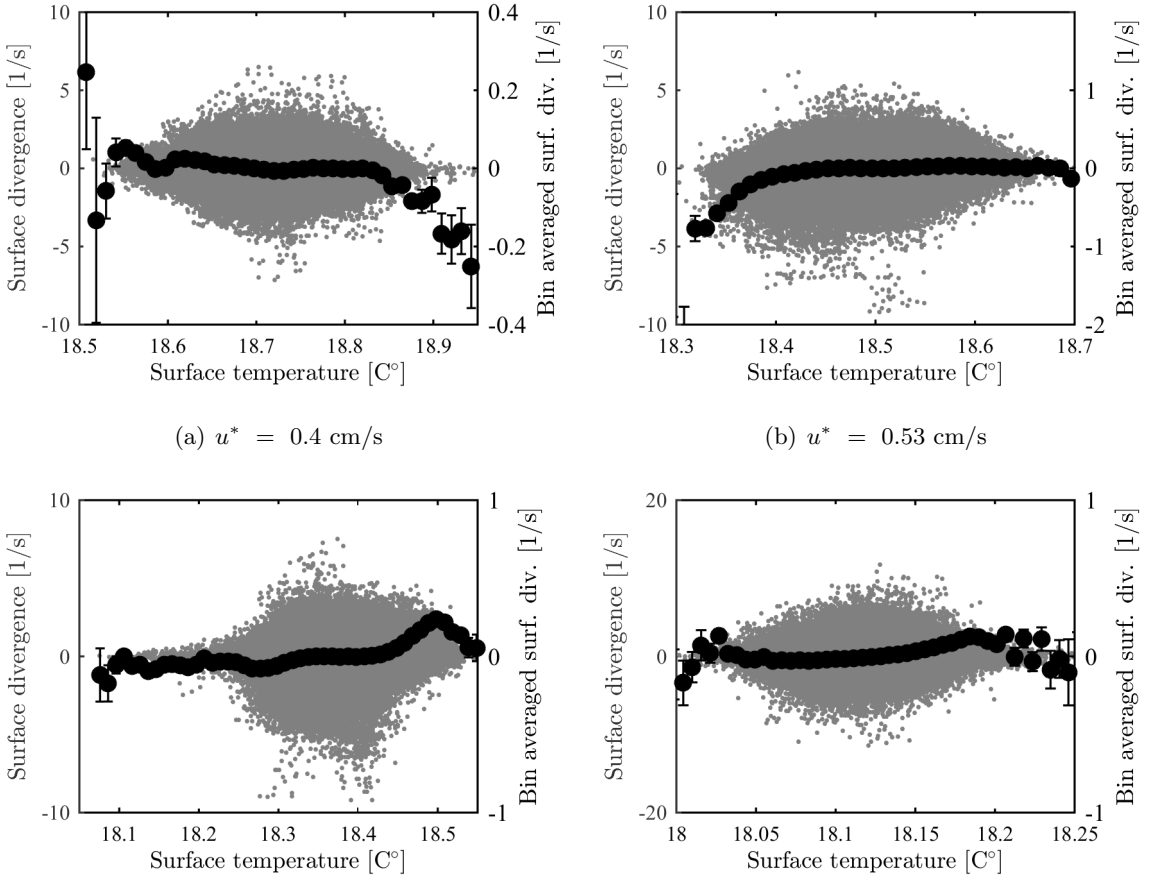

(a) $u^* = 0.4$ cm/s

(b) $u^* = 0.53$ cm/s

(c) $u^* = 0.74$ cm/s

(d) $u^* = 1.3$ cm/s

Figure 7.9.: Surface divergence over surface temperature at friction velocities from top left to lower right images, 0.4 cm/s, 0.53 cm/s, 0.74 cm/s, and 1.3 cm/s.. Gray symbols denote individual data points of 100 infrared images and corresponding velocity estimates. Black circles represent bin averages of this data, hence averaged surface divergence values on the right axis are considerably smaller than the total range on the left axis. Generally a correlation between surface divergence and surface temperature is visible. Langmuir circulations lead to significant convergence and coincides with distinctly colder temperature, microscale breaking causes localized surface divergence and therefore coincides with higher surface velocities.

microscale breaking waves.

In the second image of Figure 7.9, however, a very prominent correlation between surface temperature and surface divergence is visible. Here, significantly higher convergence coincides with relatively cold surface temperatures. This indicates the presence of Langmuir circulation which cause high localized convergence within the streak area, and explains the very pronounced footprints of Langmuir circulations in the infrared images that appear as cold distinct streaks. A comparison with Figure 7.8 shows that the corresponding velocity versus temperature plots did not show any strong correlation. Low gradients within the relatively narrow streaks might lead to an underestimation of velocities in along wind direction due to the aperture problem while convergence is caused mainly by the cross wind velocity direction.

In the third images in Figure 7.9 the correlation between convergence and surface temperature is less pronounced than before, instead high divergence coincides with high surface temperatures. One very possible explanation is microscale breaking that has been shown to form at this wind speed. Microscale breaking causes localized upwelling and thus increased surface temperature which than correlate to high surface divergence caused by the upwelling.

At high wind stress this mechanism is enhanced and thus the correlation between surface divergence and higher surface temperature is more pronounced. This corresponds to Figure 7.7 that showed that microscale breaking is very frequent at this wind stress.

7.3. Absolute surface divergence with increasing wind stress

7.3.1. Surface velocities

Figure 7.10 shows the frequency distribution of surface velocities at $u^* \approx 0.3$ cm/s and at $u^* \approx 1$ cm/s. The left image shows cross wind surface velocities, u_y, for two different wind speeds, 2 m/s and 7 m/s, with and without surfactants. Higher wind speed is represented by dark blue symbols, lower wind speed by light blue. Clean surface is indicated by dots, surfactants by crosses. In the right image, along wind surface velocities are shown for the same wind speeds. Again, darker symbols denote higher wind speed condition. Lines show Gaussian distributions to indicate the deviation of the velocities from a Gaussian shape. With increasing wind stress the distributions broaden, clearly related to the surface dynamics becoming more and more complex as different processes evolve, especially surface waves. This stands in contrast to the histograms of surface temperature frequencies (compare figure 7.13) which show clearly smaller variance at higher wind stress indicating the more homogeneous temperature pattern. The different behavior of temperature and velocity distributions has been pointed out earlier by Veron et al. [2008].

For higher wind speed cases the velocity distribution in cross wind direction seems just slightly asymmetric which is a clear indication of secondary currents in the facility that have been described in detail by Bopp [2014]. However, this effect is relatively small and well overlapped by the impact of waves and turbulence. The general shape of the velocity distribution clearly

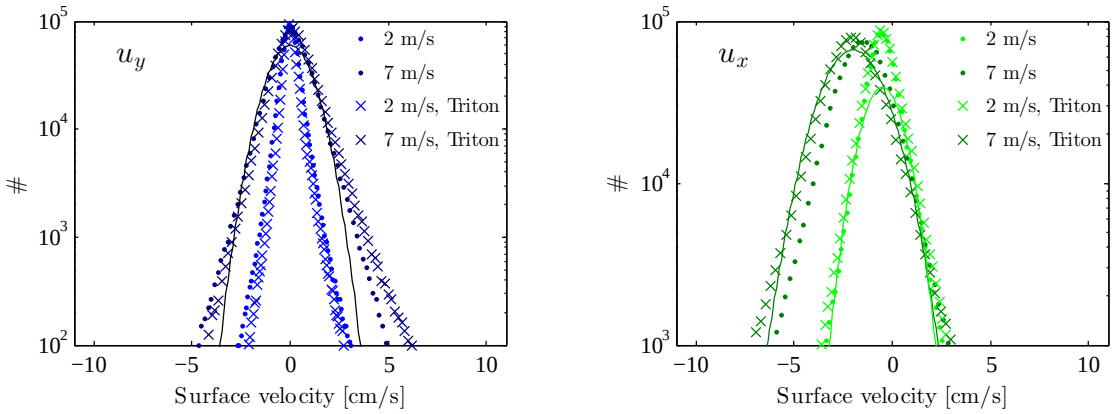

Figure 7.10.: Left: Cross wind surface velocities, u_y, for two different wind speeds, 2 m/s and 7 m/s, with and without surfactants. Higher wind speed is represented by dark blue symbols, Lower wind speed by light blue. Clean surface is indicated by dots, surfactants by crosses. Right: Along wind surface velocities. Lines show Gaussian distributions to indicate deviation from Gaussian shape.

deviates from the Gaussian (straight lines in figure 7.10) at lower as well as at higher wind speed. The deviation from the Gaussian distribution clearly shows that the generation of velocities is not a random process. Veron et al. [2008] reported the deviation from the Gaussian to be increasing with higher wind stress. However, this cannot be confirmed here, as the velocity distribution at low wind speeds is already clearly non-Gaussian.

Comparing the velocity distributions of a clean and slick covered surface, the slick covered surface exhibits clearly higher along wind velocities for high wind speeds. This again shows the impact of surface slicks on the wave field and therewith on the partitioning of wind stress. Presumably, the tangential fraction of wind stress is considerably higher in the surfactant case, and therefore exhilaration of the fluid is higher, too. At lower wind speeds and also at lower wind stress the difference between clean and surfactant covered wind stress is very small.

Mean velocities

The velocity estimation via the Brox-Corpetti algorithm was performed on a subset of the data, of five sequences of twenty subsequent images in an interval of 1.6 seconds each. Spatial and temporal averages over this subset can be seen in figure 7.11. On the left, the increase of mean surface velocities is shown over friction velocity, on the right against wind speed. Along wind velocities are shown in green, cross wind velocities components in blue. Results from the clean surface measurements are indicated by circles while surfactant measurements are indicated by crosses. Cross wind velocities are root mean square values, as the average velocity is always approximately zero, compare Figure 7.10. Error bars are derived from the deviation of mean velocities estimated from optical flow and those from active tracking (compare Figure 5.4). However, the scattering of the data is clearly larger than the size of the error bars can explain, especially if plotted against friction velocity u^*. In both representations the cross wind velocity

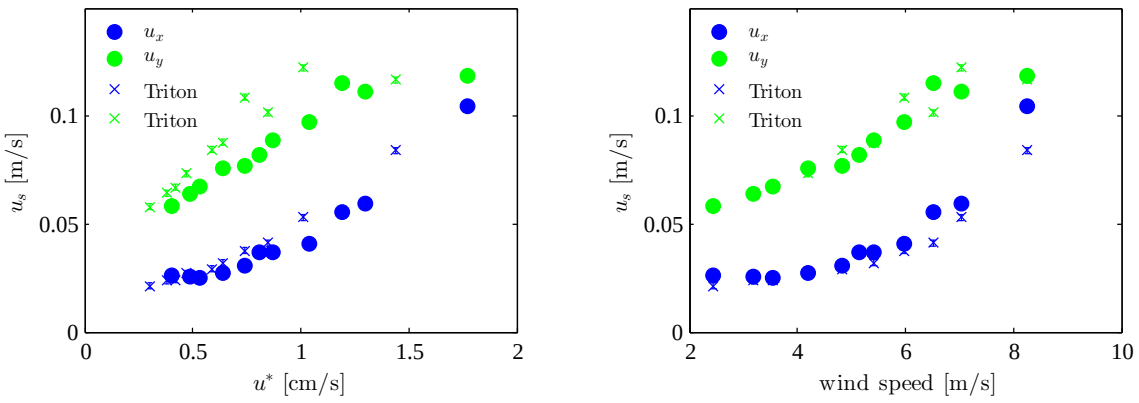

Figure 7.11.: Averaged surface velocities against friction velocity with and without surfactant Triton X-100 and along wind and cross wind components.

component is considerably lower than along wind velocities. For low wind speed cross wind velocity is approximately 35% of the along wind component. The along wind velocity exhibits a linear increase while the cross wind velocity component is best described by a polynomial function.

There is a striking difference between both representations regarding the comparison of results from clean surface measurements and Triton X-100 measurements. In the left figure in which surface velocity is plotted against friction velocity surface velocities in the surfactant cases are generally higher than the clean surface velocities. Plotted against wind speed this effect reverses and surface velocities in the surfactant case tend to be lower (though not by much). Friction velocity is a measure of shear stress and therefore momentum transport from wind to water. It is a known effect that with increasing surface roughness the fraction of shear stress that goes into wave form drag increases Banner and Peirson [1998]; Peirson [1997]. The measured friction velocity comprises the tangential component of shear stress as well as wave form drag. If surfactants are present the surface roughness is considerably reduced and so is wave form drag. Surface velocities however, are determined by the tangential fraction of shear stress, which is extremely difficult to measure independently. As a result friction velocities in the surfactant cases are considerably lower than in the clean water cases even though the tangential stress is very similar and the tangential surface velocities appear too high.

Possible errors: At higher wind speeds the distortion of the surface due to growing waves causes errors in the velocity estimation these errors can be up to 20 % in the highest wind speed. Averaging cancels this effect as the surface deviation takes a Gaussian distribution. Secondary currents in cross wind direction exist in the facility [Bopp, 2014] and though smaller than local velocity variation do contribute to cross wind velocities.

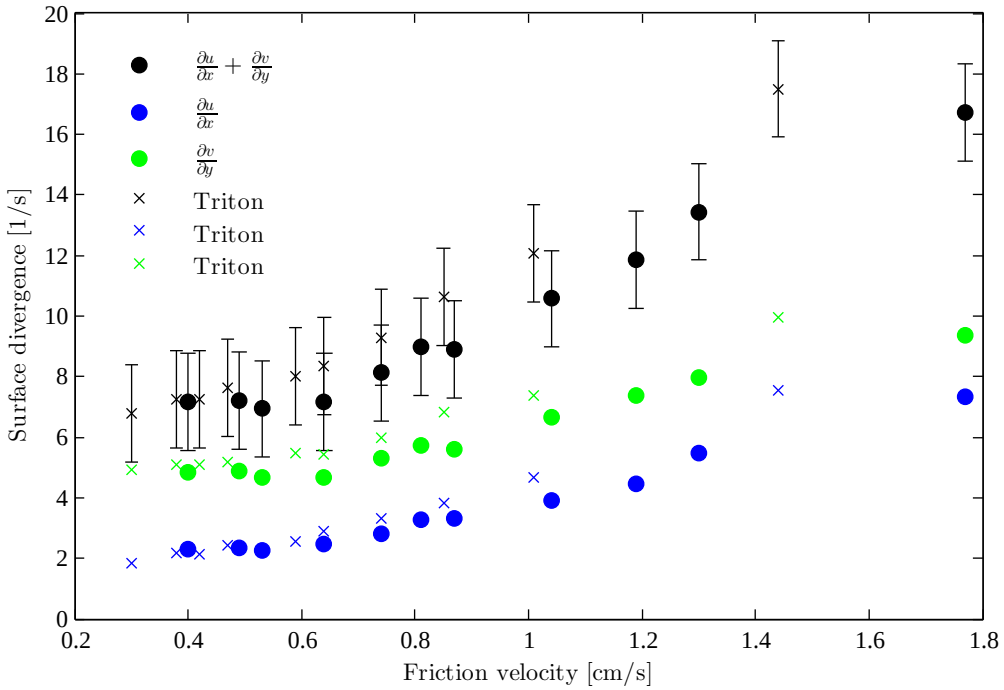

Figure 7.12.: Averaged surface divergence, indicated by by open circles is plotted against u^*. Results from clean surface and surface slick measurements are shown in blue and cyan, respectively. Additionally, along wind (crosses) and cross wind (triangles) velocities are shown

7.3.2. Surface divergence

Figure 7.12 shows root mean square values of surface divergence averaged over five independent sequences of 20 images each. The behavior of the curves are very similar to the curves of averaged surface velocities. The total divergence is split up into an along wind component, which is shown in green and the cross wind component, which is shown in blue. Clean surface and surfactants are indicated by circles and crosses, respectively.

Heat transfer rates are estimated from the surface divergence model, fist suggested by McCready et al. [1986] and further tested by for example Turney and Banerjee [2013]. Estimated heat transfer rates span a relatively small interval, with very high values at low wind speeds and comparably low values at high wind stress. This may in parts be due to erroneous velocity estimates. Especially at high wind speeds velocity estimates are a little inconsistent with lower estimates. However, the (simple) surface divergence model has been previously shown to not perform well if the surface movement is dominated by shear stress and waves Turney and Banerjee [2013] who suggested another approach to relate heat transfer rates to surface divergence based on measurements with particle image velocimetry.

7.4. Estimation of bulk temperatures based on the eddy renewal model

The estimation of bulk temperatures, e.g., the estimation of temperatures just below the water surface, is one of the crucial quantities in air-sea interaction studies. With the upcoming of high resolution satellite infrared data the temperature difference across the surface thermal layer has become of great general interest. Bulk temperature is a critical value in most models that estimate heat transfer rates.

However, in many applications it is highly desirable to estimate bulk temperature from remote sensing data to avoid in situ measurements. Various techniques can achieve this task but every bulk temperature estimate from surface temperatures is based on a conceptual model assumption. At the same time the value and/or distribution of bulk temperatures based on a specific conceptual model is an interesting feature and allows conclusions about the impact of a process on surface upwelling (or down-welling) strength.

In the following section, bulk temperature estimates from surface divergence and eddy renewal models are evaluated and compared to measured bulk temperatures. This can also be interpreted as a test to which model describes surface processes more accurately and remaining challenges.

7.4.1. Comparison of results from surface renewal and eddy renewal model

Several methods exist for the estimation of bulk temperatures. Here, bulk temperature estimates based on the surface renewal model will be compared to estimates from the eddy renewal model, both are methods that have been successfully test on infrared data of the water surface [Garbe et al., 2004; Hara et al., 2007; Hung et al., 2011].

In Figure 7.13 four histograms are shown. The upper two show histograms of surface temperature at two different wind speeds. With increasing wind stress the variance of surface temperatures decreases. This is associated with shorter renewal times and constant surface renewal so the duration a particle stays on the surface becomes shorter and so does the cooling time. Fitted is the theoretical log-normal distribution of surface temperatures derived from the surface renewal model [Garbe et al., 2004] which describes the measured temperature distribution very well. The red line indicates the bulk temperature determined from this fit. The green line shows the surface bulk temperature that was measured during the experiment.

In the upper row, histograms of bulk temperatures are shown which derive from the eddy renewal model. Here, the distribution becomes rather wider with increasing wind stress instead of narrower. Fitted is a Gaussian distribution whose peak marks the average estimated bulk temperature.

Comparing the results of the bulk temperature estimates for both methods, it becomes evident, that the eddy renewal model gives a result very close to the measured temperature, while the surface renewal model seems to underestimate bulk temperature.

The two different models stand for two different concepts and approaches to the renewal

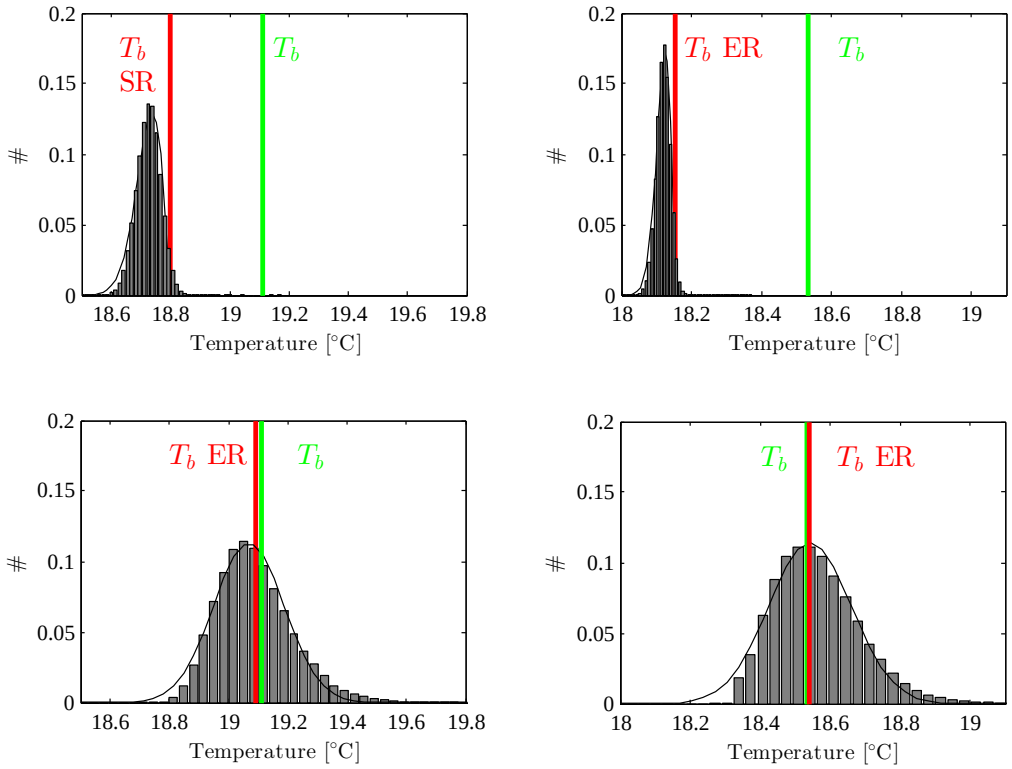

Figure 7.13.: Histograms of estimated bulk temperatures. Upper row: Estimates from eddy renewal model. Lower row: Estimates from surface renewal model. Left and right column $u^* = 0.4$ cm/s and $u^* = 1.3$ cm/s, respectively. Red lines indicate bulk temperature estimates by the respective method and green lines indicate measured bulk temperatures.

process at the water surface. The surface renewal model assumes random renewal events that transport water parcels instantaneously to the water surface. By contrast, the eddy renewal model depicts the water surface as densely packed circular eddies. The main difference lies firstly in the difference between a random distribution of surface temperatures and a more organized one that consists of coherent structures. The second big difference regards the transport of a parcel from below the thermal layer onto the surface. In the instantaneous renewal process suggested by the surface renewal model the water parcel does not cool on the way to the surface while in the eddy renewal model it does. Therefore, the temperature estimates of the surface renewal model are lower. The surface renewal model has been shown to produce accurate results. However, if the image size is too small and or the time span too short and no renewal event in the analyzed sequence, no accurate estimate can be made. Also, the assumption of instantaneous renewal is probably less accurate at low wind speeds and in the case of surfactants.

While the surface renewal produces one estimate of bulk temperature the eddy renewal assumes individual bulk temperatures for every surface eddy. This may seem confusing but the mean of the estimated bulk temperature is very near the measured temperature. The explanation may lay in the vertical structure of the water column. Just below the surface the bulk

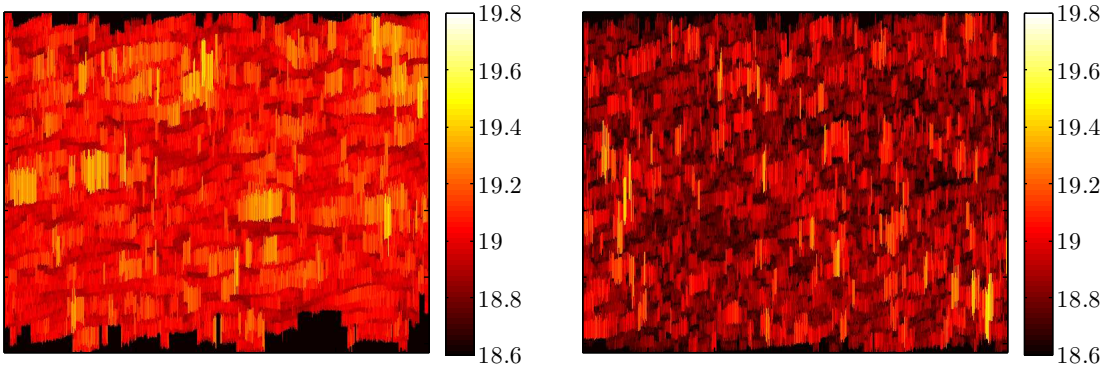

Figure 7.14.: Bulk temperature estimates for every detected surface eddy. Left and right images are from the dataset with a friction velocity of $u^* = 0.4$ cm/s and $u^* = 0.74$ cm/s, respectively. Horizontal axis corresponds to wind direction. Spatial variation of bulk temperatures clearly exhibits elongated streaks.

water is still influenced by the up and down-welling of cold water from the surface. Further down where the temperature sensor was placed the water is well mixed. As the actual heat transport is exclusively controlled within the surface layer the temperature gradient mainly shows the turbulent properties of the fluid but does not alter the mean temperature.

7.4.2. Spatial variation of bulk temperatures

In Figure 7.14 two images of the spatial variation of bulk temperatures at two different wind speeds ($u^* = 0.52$ cm/s and $u^* = 0.74$ cm/s) are shown. The temperature pattern is clearly composed of small surface streaks but also the larger scale temperature variation is captured well. While eddy size as well as surface temperature are important quantities also surface velocity plays a role. Therefore, though the temperature pattern in the right figure, at higher wind stress, seems to be less organized than in the right image, at lower wind stress, the variation of bulk temperatures still increases, as shown in Figure 7.13.

7.5. Summary

In this chapter the impact of surface turbulence on the surface temperature pattern, the surface dynamics and the subsurface temperature variation has been examined. Three turbulent regimes have been identified from the first analysis of the data, based on the respective dominant turbulence producing process. All processes discussed in this chapter have been associated with increasing transfer between air and water and all processes are clearly linked to wind stress and surface waves. However, so far no unifying model incorporates all processes.

One reason might be that it seems like the dominant turbulent features vary, depending on the chosen method of observation, i.e. surface waves seem to influence the velocity field and therefore surface divergence far stronger than it might be expected from the surface heat pattern but both

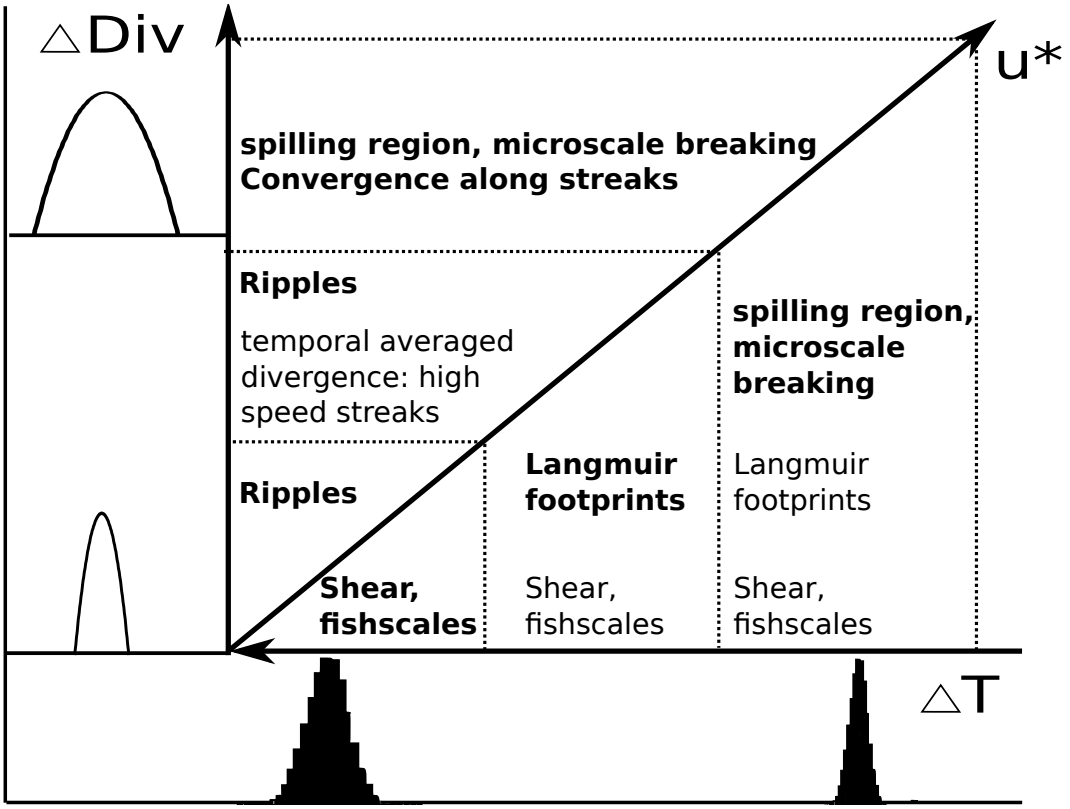

Figure 7.15.: Summary of Chapter 7. Comparison of characteristic features of near surface turbulence visible in infrared images and surface divergence from momentary velocity field, at increasing friction velocity u^*. Variation of surface temperatures decreases with increasing u^* while variance of surface divergence increases. Dominant features of the respective regime are printed bold.

quantities have been equally associated as measures for transfer rates. So how can those different observations be put in a broader perspective and give a consistent explanation and assess the impact of the different turbulent processes?

7.5.1. Characteristic features of the water surface

In Figure 7.15 a comparison is shown of characteristic features of near surface turbulence which are visible in infrared images and surface divergence from momentary velocity field at increasing friction velocity u^* . The variation of surface temperatures decreases with increasing u^* while variance of surface divergence increases. Dominant features of the respective regime are printed bold and indicate discrepancies between both observational methods.

Starting at low wind stress in infrared images, the fish scale pattern characteristic for shear induced turbulence is clearly the dominant feature while in the velocity field and thus divergence, capillary ripple cause far higher variations. This progresses at increasing wind stress, surface waves still dominate the velocity field while in the infrared image the first stable roll vortices, as characteristic for small Langmuir cells, appear. Finally, at higher wind stress both, the temperature field and the surface velocity field is dominated by microscale breaking, especially

the spilling region in infrared images and the characteristic subduction with following divergence at the tows of microscale breaking waves in the divergence images. Also visible in both methods are characteristic roll vortices on the back side of microscale breaking waves.

Thus, it seems that at low wind stress quite different processes dominate in the velocity field and the temperature pattern while at higher stress this contradiction is resolved and microscale breaking as well as streak like structures leave their traces in the infrared images as well as in the surface velocity field.

The key to this discrepancy is of course the time scale. The time scale on which a process progresses and the time scale of the measuring technique often differ, as in the case of non breaking waves. But even more importantly the question has been raised [Tsai et al., 2013; Turney and Banerjee, 2013] on which timescales are actually relevant in the scope of transfer between air and water.

As the surface divergence is based on the velocity estimation with a high temporal resolution, here, processes like fast traveling waves appear. Infrared images on the other hand show in a certain way a time wise averaged divergence and thus, highlight processes with a slower time scale and higher spatial stability. However, if the divergence is averaged over time, as shown in Figure 7.12, suddenly more stable structures like the Langmuir footprint in Figure 7.12 become visible.

Turney and Banerjee [2013] suggested a criterion based on the combination of timescale and divergence to determine whether a process acts on a time scale relevant to air-sea transfer or not: A process is only relevant if the term $e^{\int_0^t \beta(t')dt'} > 1$ which becomes $\tau\beta$ for a constant divergence β with a characteristic renewal time τ. However, previously discussed turbulent processes all fulfill this criterion if tested with renewal times calculated in Chapter 10.

So, what is the impact of the current results on the study of near surface turbulence and especially its impact on transfer rates? Firstly, relevant turbulent processes are highlighted and identified that play a role in air sea gas exchange, such as shear turbulence, wave shear coupled turbulence and microscale breaking. Secondly, it confirms that infrared images are the best suited tool to investigate coherent surface turbulence as it acts on relatively slow time scales. Finally, the complexity but also consistency of surface dynamics is shown by the interlocking of different processes that act on different timescales.

However, the question of the relative and total impact on heat transfer of a turbulent process can not yet be answered. To answer this central question the single findings of this section will need to be focused in a conceptual model to enable a more quantitative analysis.

8. Defining characteristic turbulent scales

The study of infrared images of the water surface reveals the footprints of near surface aqueous turbulence in the surface temperature pattern. In the previous section, shear turbulence, small Langmuir circulations and microscale breaking waves have been identified to greatly impact surface temperature pattern and surface velocity field. Shear induced turbulence and small Langmuir circulation both cause elongated cold streaks that differ in size and stability (compare Figure 7.2). In the following section the impact of increasing wind stress and surfactants on the two processes will be investigated. The streak spacing is chosen as a practical feature to describe the size of turbulent structures and it also provides a means to distinguish both processes. The results of the streak spacing analysis are shown against friction velocity for shear turbulence, and wave properties for small Langmuir circulations. The streak spacing is determined independently for small scale, shear induced, and large scale, wind wave coupled, turbulence as described in section 6.

Down-welling areas are indicated by cold surface streaks which are identified by the machine learning based approach within the software package Ilastik [Sommer et al., 2011]. The identification has been performed in two independent steps. First, on the infrared images, where cold streaks caused by small fish scale structures are segmented, compare Figure 6.2. In a second step, cold streaks are detected in the time-space images, e.g., shown in Figure 7.3. This ensures a separation of short lived fish scale structures and more stable Langmuir circulations and prevents wrong classifications. After the cold streak has been identified, the streak spacing is defined as the spacing between the center of one streak to the center of the next.

8.1. Small scale turbulence induced streak spacing

In this Section, the results of the streak spacing analysis of shear turbulence will be discussed.

The analysis of the fish scale pattern yields a logarithmic distribution of streak spacings. In Figure 8.1 the obtained distributions are shown at four different wind speeds and a clean water surface. With increasing wind speeds, the mean spacings are clearly shifted to smaller values and the standard deviation σ decreases (see Table 8.1). A log-normal distribution evolves, if the random forces that act on the random variable are proportionally to the variable. This indicates that forces that cause the formation of the streaks are in some way proportional to the streak spacing [Smith and Metzler, 1983]. The observed logarithmic distribution of streak spacing has previously been described by Tsai et al. [2005] obtained from the numerical simulation of a flat

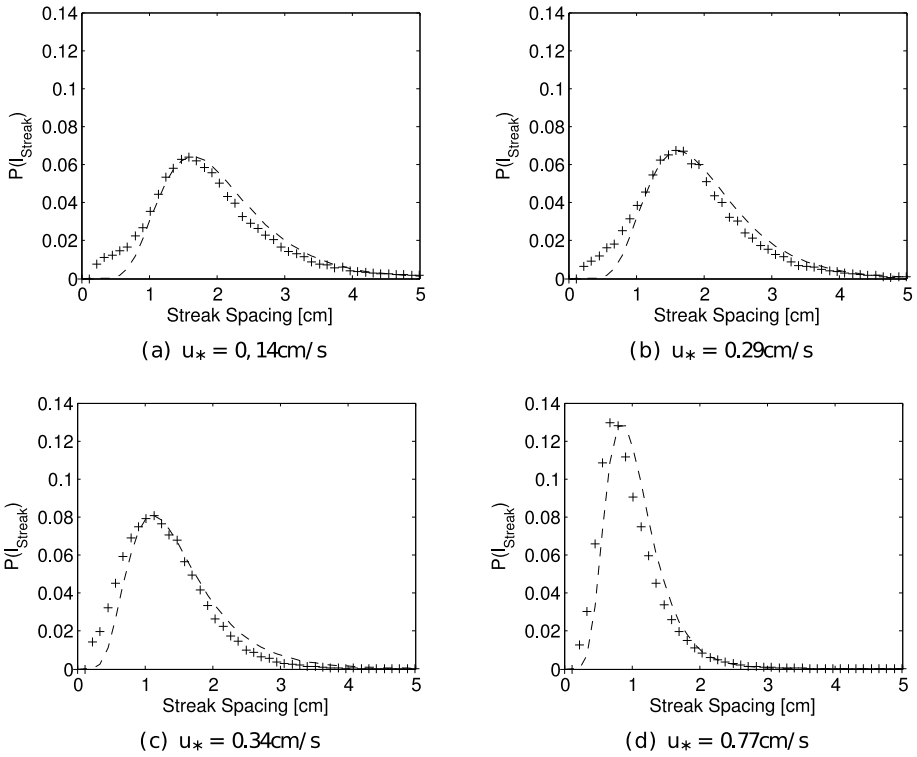

Figure 8.1.: Histograms of obtained streak spacings at four different friction velocities with a log-normal fit on the data, Aeolotron, Heidelberg, clean surface conditions. Figure from Schnieders et al. [2013]

water surface and the spacing of low speed streaks near a no-slip wall measured by Smith and Metzler [1983] indicating the similarity of the process. This is qualitatively consistent with the description of the features of the fish scale pattern described by Tsai et al. [2005].

Figure 8.2 shows a comparison of the obtained mean spacings and the theoretical values for flow near a no-slip wall. Blue columns represent mean spacing but are derived from the peaks of the distributions in Figure 8.1 and therefore lower than expected average spacing. Theoretical spacing l^+ is derived from $l^+ = (l\ u^*)/\nu = 100$. Because the peak spacing is considerably smaller than the average spacing, the value $l^+ = 50$ is chosen to visualize the theoretical trend. Red bars thus represent $(50\ u^*)/\nu$. At intermediate wind speeds, both values are approximately the same which indicates a similar turbulence production process even though the physical conditions are different (no-slip vs. free-slip boundary conditions). However, for low wind speeds the observed spacings are significantly smaller. In those cases the surface Richardson number is below the critical value suggested by Soloviev and Schlüssel [1994]. This indicates that at the lowest wind speeds in this study, at friction velocities of below 0.2 cm/s, free convection is the dominant process. For higher wind speeds a transition takes place and the turbulent cell size matches that of shear induced turbulence. However, for friction velocities above $u^* = 0.7$ cm/s observed spacings are significantly higher than the continuously decreasing theoretical values for shear induced turbulence (see Figure 8.3). This points towards a substantial change in the production at high wind stress.

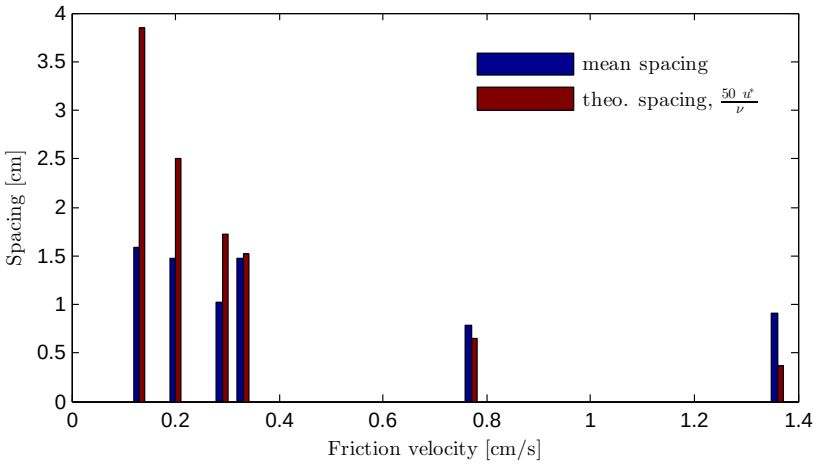

Figure 8.2.: Comparison of mean measured spacings l to theory of streaks near a no-slip wall. Blue columns represent mean spacing but are derived from the peaks of the distributions in Figure 8.1 and therefore lower than expected average spacing. Theoretical spacing l^+ is derived from $l^+ = \frac{l\ u^*}{\nu} = 100$. Because the peak spacing is considerably smaller the value $l^+ = 50$ is chosen to visualize the theoretical trend. Red bars thus represent $\frac{50\ u^*}{\nu}$.

8.1.1. Correlation of streak spacing and friction velocity

The modes of the fitted log-normal distributions of all the experiments that are accounted for in this work are shown in Figure 8.3. The error bars mark the 1σ confidence interval of the log-normal distribution which illustrates the variability of the obtained statistics but not the measurement error. The error bars of u^* represent the measurement errors and depend on the measurement technique.

It is remarkable that the measured streak spacings do not vary by more than 30 % even though the data was collected under several entirely different experimental conditions such as clean water surface, surfactant covered water surface, a cooled and heated water body resulting in warm and cool skin cases and additional mechanical waves. However, the data from the wind wave channel at WRL shows constantly slightly higher values of streak spacing in comparison to the other cases. Also the histograms of the spacing scatter far more (and have therefore a higher error) and show a broader distribution. Partly this can be explained by the additional surface waves along with resulting disturbances of the surface heat pattern. Additionally a considerably smaller heat flux leads to less prominent cold surface streak and may cause an overestimated spacing if small streaks cannot be detected.

The streak spacing does not seem to be influenced either by the presence of surfactants or by the presence of additional mechanical waves. Even though surfactants have the above mentioned effects on near surface turbulence and lead to a damping of turbulence [Soloviev et al., 2011], it does not seem to influence the spacing of the evolving streaks.

The expected lapse of streak spacings from experiments and simulations of low speed streaks near no-slip walls over u_* would be continuous, ($l^+ = lu_*/\nu = 100$). The distribution of streak spacings over u_*, that was obtained in this analysis shows a different behavior. At friction

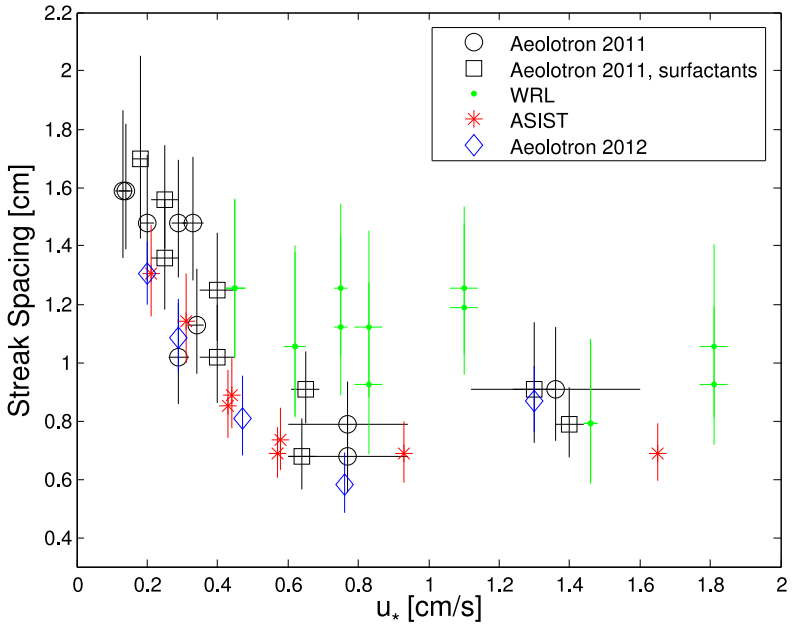

Figure 8.3.: Streak spacing against u^* obtained from data measured at the Aeolotron, Heidelberg (IR camera: Thermosensorik CMT 256) without (black circles) and with surfactants (black squares), at the Aeolotron, Heidelberg (IR camera: IRCAM Velox 327k M) (blue diamonds), at WRL (green dots), Sydney, and at the ASIST facility in Miami (red stars). Y-error bars mark 1σ intervals of the underlying log-normal distribution and represent a measure of the variability of the system. A linear fit describes the distribution reasonably well up to a friction velocity of $\sim 0.7\,\mathrm{cm/s}$. From then on the obtained streak spacings seem to be independent of u^*. The dotted line shows the trend for shear induced turbulence according to $lu^*/\nu = 100$.

velocities up to a value of 0.7 cm/s, there seems to be a clear trend of smaller spacings at larger u_* and in this regime the development could be described by a linear regression. So in regimes of small friction velocities there seems to be a clear link between the size of the turbulent structures and the tangential shear stress producing them.

This behavior changes at a friction velocity of approximately 0.7 cm/s. From this point on streak spacings remain approximately constant and are seemingly independent of u_*.

There seems to be a lower boundary for the size of the coherent turbulent structures as the spacing of the streaks is a direct measurement of the width of the shear induced turbulence and therefore also of the same scale as the shear layer itself [Hunt et al., 2011]. One possible explanation is the saturation of tangential stress at the water surface above a threshold friction velocity u_*.

There is also a lower boundary for the size of the structures that can still be detected. But similar values for measurements with infrared cameras with different spatial resolutions and therefore different lower detection boundaries, show that this is probably not the reason for the stagnating streak spacings.

Banner and Peirson [1998] found that the increase of tangential stress with wind speed is limited. The relation of tangential to total wind stress (τ_t/τ) has a trend towards a value of

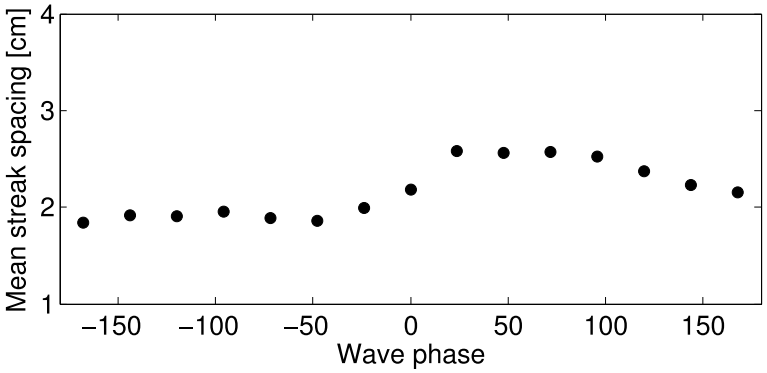

Figure 8.4.: Mean spacing along the wave phase, Incipient breaking case, $u^* = 1.11$ cm/s. The streak spacing was determined in line with the wave probe. Single points have been bin averaged and are plotted against wave phase.

0.3. With increasing wind stress an increasing part of the total wind stress is transformed into wave form drag while the tangential stress is even slightly decreasing [Banner and Peirson, 1998]. This effect might well be an explanation for the here observed stagnating streak spacing. The transition of streak spacing into the plateau corresponds to the by Banner and Peirson [1998] observed wind speed and the appearance of the first gravity waves.

Interestingly the stagnation point is reached at approximately the same u_* for all experimental conditions including different fetches and even experiments with surface slicks. In the cases with surface slicks, it should be noted that in all data points that are in the stagnating area, gravity waves were present at MSS values of the same magnitude (circa 70 %) as in the cases without slicks (compare Table 8.1).

There seems to be a slightly larger variation within the streak spacings obtained at UNSW with additional mechanical waves. This could well be the case because of variations in the shear stress coherent with the phase of the underlying mechanical waves.

8.1.2. Influence of wave conditions

It has been shown that the wave field has no (or very small) influence on the distribution of streak spacing. However, there seems to be a small variation of the streak spacing along the wave phase. The results are obtained from the data measured in a linear wind channel at the Water Research Laboratory (WRL) at the University of New South Wales (UNSW). The wave height was measured with a wave probe which was also visible in the infrared images. From the known position of the heated spot and the knowledge of the wave phase it was now possible to calculate the mean spacing at the position of the heated spot in one line of the image.

In Figure 8.4, an average of the obtained mean streak spacings is plotted against the wave phase. In the incipient breaking case with a u_* of 1.1 cm/s there is a small increase to larger streak spacings just behind the wave crest. A similar distribution could have been expected because of the crucial role that shear stress plays in the development of the small scale heat pattern. Peirson [1997] and Banner and Peirson [1998] found the tangential shear stress to decrease from the wave crest at 0° to nearly zero at circa +75°. This corresponds to the wave phase in which

the increase of streak spacing was observed. This is consistent with the assumption of the small scale turbulent structures being shear induced. In this regime of moderate wind speeds, a decreased shear stress leads to larger streak spacings for sufficiently small friction velocities.

8.2. Langmuir Circulation-induced cold streaks

Larger scale streaks with an extended lifespan evolve at higher friction velocities, compare Figure 7.3. As described earlier, their appearance is clearly linked to the onset of gravity waves. The detection of these larger scale streaks is performed on time-space images separately from the detection of the shear induced surface streaks discussed in the previous section (compare also Section 6). In Figure 7.3 space time images at two different wind speeds are shown with and without surfactants. Again it becomes evident that the development of the stable streaks progresses gradually and is substantially delayed in the case of a surfactant layer.

8.2.1. Influence of mechanical waves on Langmuir like turbulence

In the data set measured at Water Research Laboratory at UNSW the influence of mechanical surface waves at different wave conditions and wind speeds on micro-Langmuir circulations becomes evident.

Langmuir Circulation indicating cold streaks occur in all cases except for the strongest breaking case. They are clearly present in the capillary ripple cases. They are less distinct in the low wave cases but can clearly be seen in the incipient breaking cases and in the micro scale breaking case for lower ak values. In the micro scale breaking case with a value of $ak = 0.32$, there are no more stable circulations visible.

Mizuno [2011] observed similar behavior of Langmuir cells under the presence of mechanical waves. Langmuir circulations in a linear wind wave channel were destroyed by additional mechanical waves, thereby contradicting CL II Theory. The suggested explanation is, that the additional energy introduced by mechanical waves enhances the wave growth without leading to an enhanced wave breaking which would lead to a dissipation of the energy. Therefore, it is concluded in Mizuno [2011] an enhanced return flow leads to a collapse of the Langmuir vortices. This effect was found to appear at values of $ak = 0.1$. In these measurements, the dark streaks indicating stable Langmuir circulations persist until values of $ak = 0.32$.

8.2.2. Langmuir numbers and streak spacings

From the temporal profiles the streak spacings have been estimated in the cases in which the streak spacing was small enough to be captured by the image size.

The conditions during the measurements at WRL (monochromatic waves with a set frequency f, wave number k and amplitude a) allow a comparison with the LC stability theory developed by Leibovich and Paolucci [1981]. This is done in analogy to Melville et al. [1998]. The stability

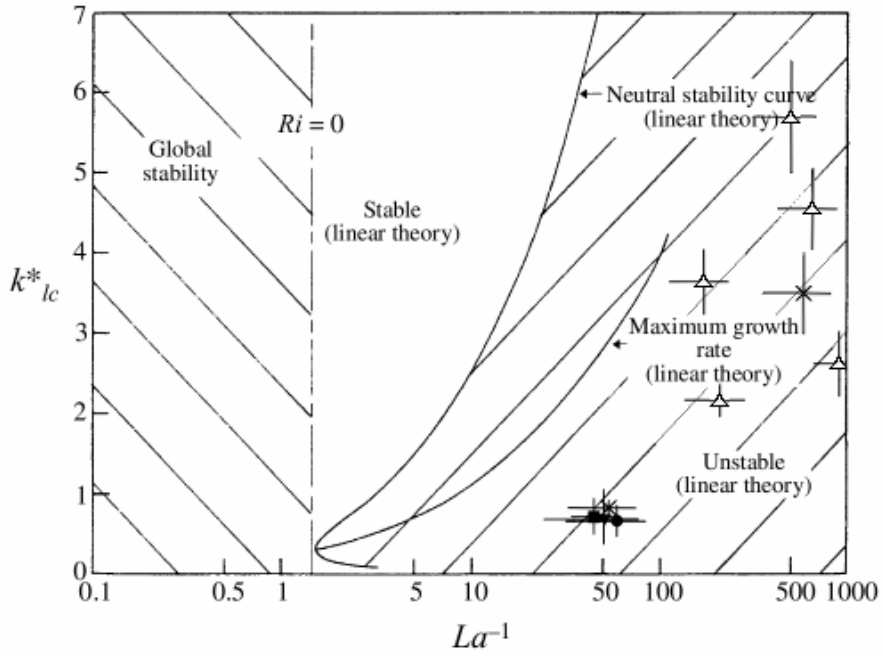

Figure 8.5.: $k^*_{\mathrm{LC}} = \frac{k_{\mathrm{LC}}}{k_{\mathrm{wave}}}$ against inverse Langmuir number La^{-1}. Neutral stability theory by Leibovich and Paolucci [1981] compared with the data obtained by Melville et al. [1998] and the data measured at WRL under the presence of mechanical waves (open triangles) and the data from aeolotron (crosses).

theory applies for a homogeneous stationary wave field with wind beginning at a certain time with constant stress.

The Langmuir number is calculated according to Equation 2.31.In analogy to Melville et al. [1998] the eddy viscosity is estimated from the shear layer thickness. As the shear induced turbulence scales with the shear layer thickness [Hunt et al., 2011], the scale obtained from the analysis of the small scale shear induced turbulence is used for the estimation of the eddy viscosity.

$$\nu_t = k u_* l_{\mathrm{S.I.T}} \tag{8.1}$$

with the von Karman constant $k = 0.4$, the spacing of the shear induced turbulence $l_{\mathrm{S.I.T}}$ and the friction velocity u_*.

Both Leibovich and Paolucci [1981] and Melville et al. [1998] presented a stability diagram of dimensionless wave numbers $k^*_{\mathrm{LC}} = k_{\mathrm{LC}}/k_{\mathrm{wave}}$ against inverse Langmuir numbers La^{-1}. Here k_{LC} is the "wave number" obtained from the spacing of Langmuir streaks and k_{wave} is the wave number of the mechanically generated waves. The inverse Langmuir number can be regarded in analogy to the Rayleigh number. The Rayleigh number describes the relationship between buoyancy and viscosity in the case of heat convection. Accordingly, La^{-1} describes the quotient of inertial and viscous forces in CL II theory.

Consequently, the flow is stable for very small La^{-1} and becomes unstable for larger La^{-1}. In Figure 8.5 the data points obtained here are compared to the global stability boundary that is found for constant Richardson numbers ($Ri = 0$) while varying Langmuir number La and wave

number k [Leibovich and Paolucci, 1981] and the values obtained by Melville et al. [1998]. The global stability boundary developed by Leibovich and Paolucci [1981] is derived from the time of the onset of instability. The measurement of Melville et al. [1998] are correspondingly made at the onset of Langmuir circulations. In contrast, the values obtained here originate from an equilibrium state with both, wave field and wind stress constant in time. A comparison still shows good agreement. The obtained values for La^{-1} are located in the unstable regime as expected.

The large error bars arise mainly from the inaccurate determination of the streak spacing. Wavelength for the data measured at the Aeolotron have been determined from the images of the CISG in the low wind speed case and for the case with a higher wind speed, from the new experimental measuring technique for the characteristics of gravity waves of Eisenhauer [2011]. Melville et al. [1998] measured growing La^{-1} numbers prior to the inception of Langmuir circulation thus the La^{-1} number measured here will presumably be larger than it was at the inception of LC.

Table 8.1.: Summary of the analyzed streak spacings and experimental conditions. U, u^*, MSS, Streak Spacing and Sigma are the wind speed in meters per second, the friction velocity in cm/s, the Mean Square Slope values, the streak spacing as the result of the analysis in cm and the standard deviation of of the distribution of the streak spacing also in cm, respectively. The measurement error of the friction velocity is 0.02 cm/s for low and intermediate wind speeds and 0.1 cm/s for the highest wind speed. Sigma can be seen as a measure of the variability of the log normal distributions of spacing.

Aeolotron, No surfactants				*Aeolotron, Surfactants (Triton X-100)*			
U	u_*	**Spacing**	**Sigma**	U	u_*	**Spacing**	**Sigma**
1,0	0,13	1,59	0,06	1,8	0,18	1,70	0,06
1,2	0,14	1,59	0,04	2,4	0,25	1,36	0,04
1,8	0,20	1,48	0,05	2,4	0,25	1,56	0,04
2,6	0,29	1,48	0,05	3,4	0,40	1,25	0,05
2,4	0,33	1,48	0,04	3,4	0,40	1,02	0,05
2,7	0,34	1,13	0,05	4,7	0,65	0,91	0,04
2,4	0,29	1,02	0,05	4,6	0,64	0,68	0,04
4,6	0,77	0,68	0,04	6,5	1,04	0,79	0,04
4,6	0,77	0,79	0,04	6,4	1,02	0,91	0,06
6,4	1,36	0,91	0,04				
ASIST, Miami				*WRL, Sydney*			
U	u_*	**Spacing**	**Sigma**	U	u_*	**Spacing**	**Sigma**
1,9	0,21	1,31	0,04	2,1	0,45	1,3	0,1
2,9	0,31	1,14	0,04	2,1	0,75	1,2	0,1
4,0	0,43	0,85	0,04	5,7	1,81	1,0	0,1
4,0	0,44	0,90	0,04	4,2	0,62	1,1	0,1
5,0	0,58	0,73	0,04	3,9	0,81	1,0	0,1
5,0	0,57	0,69	0,04	3,9	1,11	1,2	0,1
7,1	0,93	0,69	0,04	3,9	1,46	0,8	0,1
10,1	1,65	0,69	0,04				

*The streak spacing of the small scale turbulence results from the log-normal fits on the obtained distributions.

8.3. Summary

Two turbulence generating mechanisms have been identified to play a role in the generation of cold, streak shaped convergence zone that appear in the surface heat pattern. The small scale structures termed fish scales result from wind stress only and are therefore considered as shear induced turbulence. The larger scale cold surface streaks have been identified as Langmuir circulation induced as described by Caulliez [1998]; Melville et al. [1998]; Veron and Melville [2001].

The nature of this pattern changes with increasing wind stress and surface condition, though differently for shear induced turbulence(1) and LC(2).

(1): The small scale heat pattern is substantially dependent on wind speed, indicating that shear stress only is the generating mechanism. The analysis of the streak spacing yields a log-normal distribution. This is qualitatively consistent with the findings of Tsai et al. [2005] on numerical data and also to the work of Smith and Metzler [1983] and Nakagawa and Nezu [1981] on the spacing of low speed streaks near a no-slip wall thereby indicating the similarity of the causing process. In the regime of very low wind speeds streak spacing decreases linearly with wind speed and this behavior is the same as for low speed streaks near a no-slip wall. Surprisingly, above a friction velocity of ~ 0.7 cm/s the streak spacing seems to become relatively independent of wind stress. Considering that tangential stress is the driving factor and that the fraction of tangential stress has been reported to remain constant as more of the wind stress is transformed to wave form drag [Banner and Peirson, 1998] this could be an explanation for the stagnating streak spacing. Although, the turbulence in the shear layer is highly non-isotropic, a scale can be calculated in analogy to the smallest possible eddy size for isotropic turbulence, the Kolmogorov scale. We estimate the energy dissipation rate $\langle \epsilon \rangle = u^3/l$, with u the velocity and l the integral length scale. Because of the anisotropy we used the surface velocity in y-direction as u and the largest observed streak spacings as l. The result of the rough estimation is a length scale η of order $\mathcal{O}(0.1\,\mathrm{cm})$. This would also lead to a minimum cell size of anisotropic turbulence. The influence of viscosity does not become apparent in our result and the rough estimation of changes of smallest possible eddy sizes shows that an increase in temperature by 10 K results in a 20% change of the micro scales. As the variability of streak spacings is generally very high this is difficult to determine.

(2): Larger scale cold streaks in comparison are not as dependent on wind stress but their appearance and spacing is determined by the surface wave field thereby showing they are indeed Langmuir circulation, as described in [Caulliez, 1998; Melville et al., 1998; Veron and Melville, 2001]. The analysis of the streak spacing in comparison to wave field parameters allows a comparison to the data presented by [Melville et al., 1998; Veron and Melville, 2001] and the predictions of Leibovich and Paolucci [1981].

Even though the conditions were different (measurements were conducted not just after the onset of waves but in a fully developed wave field) our measurements match those of Melville

et al. [1998] very well for identical Langmuir numbers. Higher inverse Langmuir numbers lead to higher values of normalized Langmuir wave numbers and thereby follow the trend suggested of the neutral stability theory by Leibovich and Paolucci [1981].

In recent work by McKenna and McGillis [2004] and Veron et al. [2011] it has been shown that surface divergence has an enormous effect on surface heat and gas fluxes.

We conclude that the here presented method based on passive thermography and the subsequent analysis of streak spacing provides a valuable tool to assess features of near surface turbulence and gain insight into turbulent processes that are a controlling mechanism in air-sea gas exchange.

9. Introducing the concept of eddy superposition

One goal of this work is the classification of coherent turbulent structures and the quantification of its respective impact on transfer across the air-water boundary. Therefore, we need a conceptual model that firstly, comprises different scales of turbulence and secondly, provides a means to assess the impact on transport, e.g.,by estimating heat transport rates. Several conceptual models have been presented in Section 3 and all of them provide heat transfer rates. However, the challenge is to separate processes that act simultaneously, especially shear driven and small Langmuir Circulation.

The surface renewal model (Section 3.2), introduced by Higbie [1935] and Danckwerts [1951], is a simple but effective model. Renewal events are considered as statistical one dimensional events of single water parcels moving up to the surface. There have been attempts to compare the model output to processes of different scales by Schimpf et al. [1999a] by calculating different heat transfer rates on the same image but on different levels of the gaussian pyramid. Due to the basic assumption of statistical renewal events it is not possible to relate this back to a specific process.

Closer to what can be observed in thermographic data is the eddy renewal model (Section 3.4) [Fortescue and Pearson, 1967; Hara et al., 2007; Lamont and Scott, 1970]. The eddy renewal model assumes a water surface which is densely packed with stationary cells of rotating fluid and has been tested on infrared imagery by Hara et al. [2007]; Hung et al. [2011]. The major drawback, especially if applied to noisy infrared data, is that heat flux and bulk temperature are both drawn from a single fit along one eddy and additionally it comprises only one eddy size and assumes sinusoidal velocities.

Here, we will apply the concept of eddy renewal with the addition of allowing eddy superposition. From the surface heat pattern we have learned that even on small scales different turbulence generating mechanisms overlap, e.g.,the images show footprints of shear induced turbulence as well as larger scale footprints [Handler and Smith, 2011; Schnieders et al., 2013]. Their characteristics have been shown to match those of Langmuir circulation very closely [Schnieders et al., 2013].

The surface temperature pattern can thus be described if one assumes a superposition of larger scale and smaller scale eddies, i.e. shear induced turbulence and small Langmuir circulation, compare Figure 9.1. Algorithms to separate both processes have been suggested in Schnieders

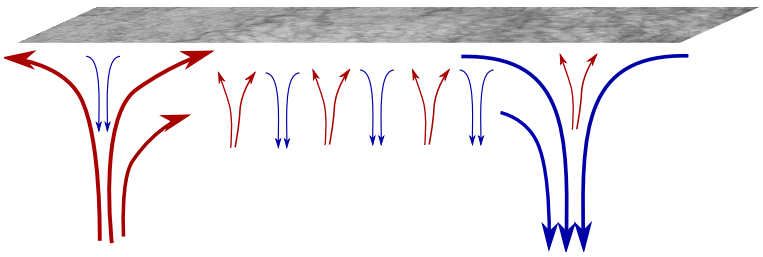

Figure 9.1.: Sub-surface eddies causing surface divergence and convergence on various scales. Based on the observation of the surface temperature pattern, eddies of two dominant scales can be identified. Instead of densely packed subsurface eddies, as in the traditional eddy renewal model [Hara et al., 2007], a superposition of eddies of different sizes is allowed. This enables to model temperature variation on different scales as observed in the infrared images, especially the combination of small scale shear induced eddies and larger scale Langmuir circulation induced eddies.

et al. [2013] and are described in more detail in section 6.

9.1. Heat flux estimates from passive Thermography

The estimation of heat transfer is crucial, firstly, to be able to assess the impact of a process and secondly, to test the accuracy of the conceptual model applied to describe the water surface. The here developed concept of eddy composition is a combination of the theory on which also the surface renewal model is based, compare Soloviev and Schlüssel [1996], and the eddy renewal model. From Equation 3.7 [Garbe et al., 2004]

$$k = \sqrt{\frac{\pi\ \kappa}{2}} \cdot \sqrt{\frac{\dot{T}}{\Delta T}} \tag{9.1}$$

a more robust approach to the estimation of a heat transfer rate is taken. The critical quantities dT/dt and $\Delta T = T_{\text{bulk}} - T_{\text{surface}}$ will be calculated based on the analysis techniques in Section 3. The general scheme is shown in Figure 9.2.

Starting from the original infrared data the first two major processing steps are undertaken independently and provide the segmentation of the surface temperature pattern from the random forest based classification and the surface velocity field from optic flow. These two quantities are crucial in the following processing steps. The segmentation provides two stencils to identify up- and down-welling regions on two scales and the surface velocity field acts as weighting field in the deviation of total derivatives, bulk temperature and transfer rate. One may note that the surface velocity field will inevitably be inaccurate on the smallest scales of shear induced eddies due to the aperture problem which prevents the velocity estimation across a small eddy. However, this cannot be resolved and in Section 5.4 it is shown that estimated cross wind velocities match those determined from active Thermography quite well.

The temperature gradient is taken from the warm upwelling area to the cold down-welling area and reflects the cooling rate of water parcels within the eddy. The total derivative of surface

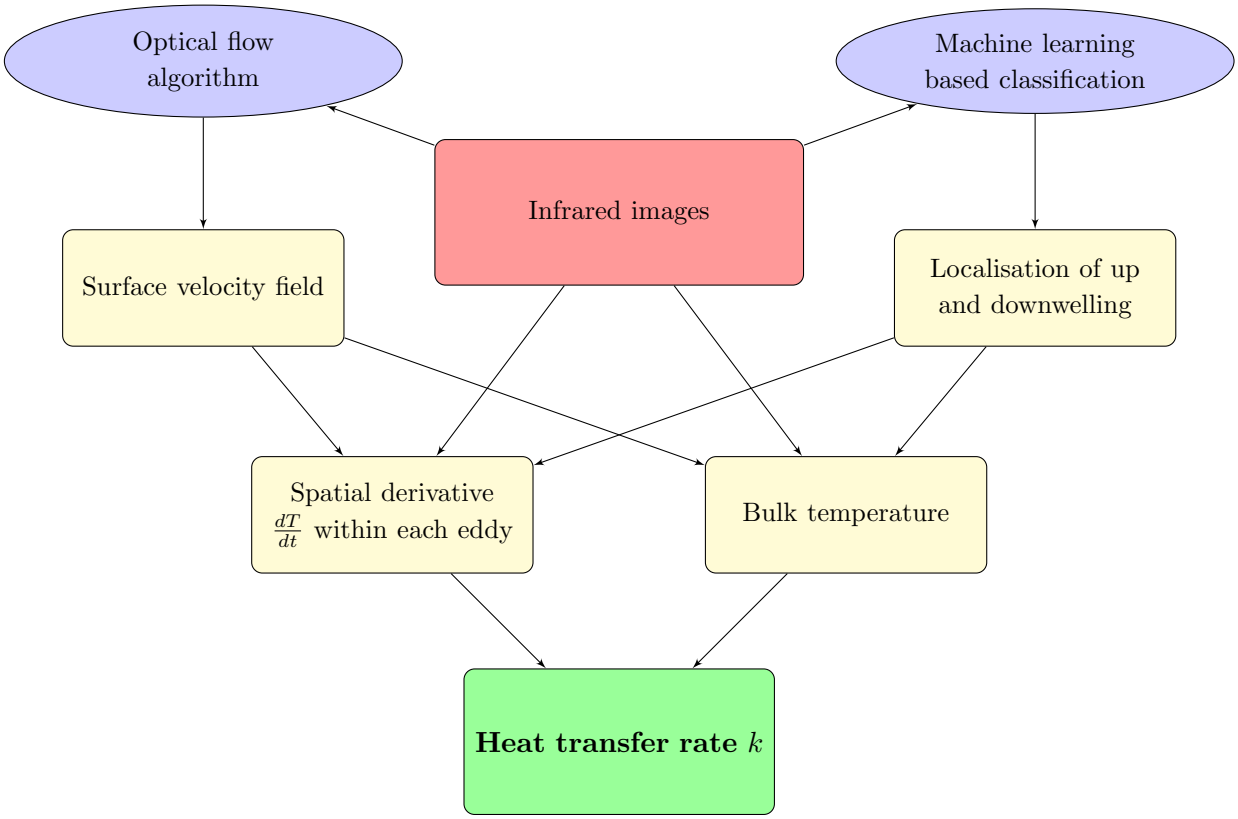

Figure 9.2.: Estimation of transfer velocities based on the concept of eddy renewal. Starting from a sequence of infrared images, a machine learning based classification provides the localization of up- and down-welling areas. Surface flow fields are provided through the optical flow estimation. From the surface velocity field and the temperature gradient from the infrared image, spatial derivatives are computed based on the localization of those eddies. The bulk temperature is estimated vie the classical eddy renewal model described in Hara et al. [2007]. From the spatial derivative and the bulk temperature the heat transfer rates is computed, averaged over each detected eddy.

temperature is:

$$\frac{dT}{dt} = \frac{\partial T}{\partial t} + u\,\frac{\partial T}{\partial x} + v\,\frac{\partial T}{\partial y} + w\,\frac{\partial T}{\partial z} \tag{9.2}$$

Assuming stationary eddies which are uniform in along wind direction and stationary in time the total derivative simplifies to:

$$\dot{T} = v\,\frac{\partial T}{\partial x} \tag{9.3}$$

The bulk temperature is estimated from the original eddy renewal model by Hara et al. [2007] based on average surface velocity and eddy stencil. This has been shown to provide very realistic estimates and average bulk temperature matches very well with the measured one.

Finally, heat transfer rates are estimated for the respective eddy based on the total derivative

and bulk temperature. All quantities are determined in a framework that is consistent with the conceptual model of composite eddies.

It is difficult to give precise measurement errors for some of the crucial quantities needed to calculate the heat transfer rate k. Nevertheless, it is instructive to perform an error propagation analysis to identify most important error sources and get an estimate of expectable errors, which can be found in the appendix A.2. It shows that the bottle neck quantity remains the surface temperature field, even though the deployed infrared camera (IRCAM Velox 327k M) has a very high sensitivity. However, the results depend heavily on the accuracy of model assumptions and systematic errors might be significantly higher than the statistical errors. Any result of estimated heat transfer rates are also a test of model assumptions and should not be treated as a measurement technique.

10. The impact of surface eddies on heat transfer

10.1. Heat flux estimates from surface eddies

In Chapter 8, characteristic scales and the distribution of turbulent eddy sizes have been determined for shear turbulence and small Langmuir circulations. Furthermore, the effect of increasing wind and surfactants on eddy sizes has been studied.

Temperature gradients provide a means to estimate the impact of a process on heat exchange. However, a more quantitative assessment of the impact of individual processes on transfer rates requires an estimation of the transfer velocity. The modified eddy renewal model described in Section 9 provides a means to determine heat transfer rates of individual surface eddies based on the surface temperature gradient and the estimated velocity field.

In the following section, a mechanistic approach is made to the explanation of increasing transfer rates with wind speed and the impact of surface waves. Here, the finding of the previous sections about predominant processes at the water surface and their reaction to changing surface condition will be combined to assess the impact of individual processes on heat transfer.

Heat exchange rates are estimated based on the eddy renewal model described in section 9. This means that all heat flux estimates are based on the assumption of circular eddies just below the water surface. Therefore, surface renewal events without a distinct streak like shape, such as the spilling region of microscale breaking waves are not considered.

In accordance with the concept of eddy superposition proposed in section 9 the two clearly distinguishable kinds of coherent turbulence will be treated independently in their impact on heat transfer rates.

10.1.1. Shear turbulence induced heat flux estimates

The analysis of the small scale surface heat pattern is performed as described in section 6. Figure 10.1 shows a comparison of the results for the small scale analysis and the original infrared images. In the lower image in Figure 10.1 calculated values for the heat transfer velocity k are shown for every pixel. Heat transfer rates are averaged across each streak. The spatial distribution of transfer velocity estimates resembles the original temperature pattern and indicates that in this case the temperature is a good tracer exchange rates on small scales. Coherent structures are clearly visible in the images of the heat transfer rates and reflect the footprints of

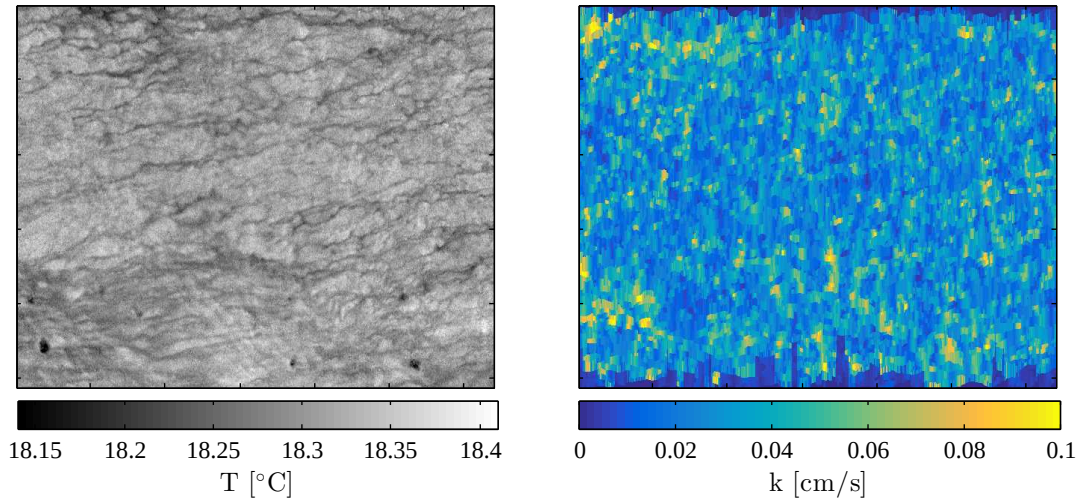

(a) IR, $u^* = 0.9$ cm/s

(b) k, $u^* = 0.9$ cm/s

Figure 10.1.: Left: Infrared image, Right: Estimated heat transfer velocities k averaged across each detected surface eddy in cm/s. This estimate is based on the segmentation of shear induced turbulence only. The spatial variation of heat transfer velocity estimates reflects the small scale surface temperature pattern but not larger scale temperature variation due to Langmuir circulation. This indicates that both processes have been separated successfully.

turbulence in the infrared image. While the small scale temperature pattern is clearly captured the larger scale cold streaks are not reflected in the heat flux estimation image. This shows that the chosen method is able to separate both turbulent processes and there is, if any, very small influence from larger scale temperature variations.

Figure 10.2 shows the relationship between turbulent cell size and heat transfer in more detail. Heat transfer rate, on the y-axis, is plotted against streak spacing, on the x-axis in the two dimensional histograms. The probability density is color coded. With increasing wind stress the form of the histograms changes. There are two dominant effects: The first is small a shift of the whole curve to higher heat transfer rates at the same turbulent cell size. This can be simply explained by higher surface velocities that obviously lead to higher transfer rates. The second effect is the already observed shift to smaller eddy sizes for higher wind speeds. As small streaks tend to have higher k values this leads to an overall slightly higher average heat flux. At the same time, the peak in the probability density function is far more pronounced in the higher wind speed cases. This means that for higher wind speed, turbulent cell sizes become far more homogeneous, i.e. equally sized eddies produce very similar values of heat transfer rates k.

Smaller scales and higher heat transfer rates occur at higher wind speed. This indicates that surface velocity is a key player in determining the total transfer, at least at low to moderate wind speeds and regarding shear induced turbulence. Not surprising, as in the scheme of eddy renewal higher velocities translate directly to smaller surface renewal times and therefore higher fluxes.

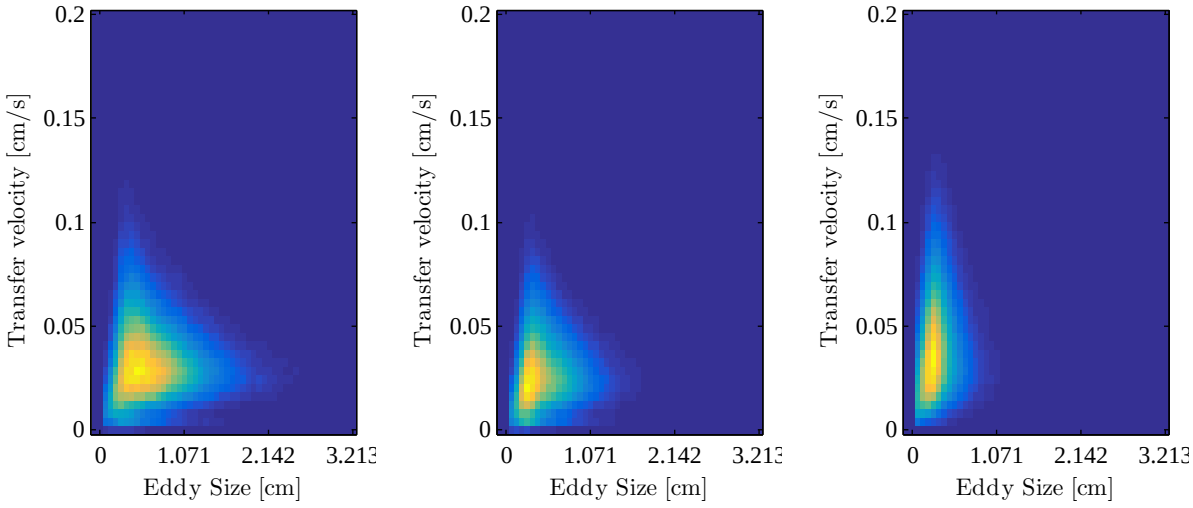

(a) $u^* = 0.4$ cm/s (b) $u^* = 0.9$ cm/s (c) $u^* = 1.8$ cm/s

Figure 10.2.: Two dimensional histograms of heat transfer velocity on the y-axis against eddy size on the x-axis based on the analysis of shear induced turbulence. Three different wind speeds are shown, the friction velocity increases from left image to right from 0.3 cm/s to 2.1 cm/s. The normalized probability density is color coded. At low wind stress the distribution is clearly broader and extends to larger eddy sizes while at higher wind stress the distribution is very narrow. This indicates that the surface temperature pattern exhibits small eddies of very homogeneous sizes caused by shear induced turbulence.

10.1.2. Shear wave coupled turbulence induced heat flux estimates

The estimation of heat fluxes from shear wave coupled turbulence is performed on time space images. An example image is shown in Figure 10.3. In the left image the original time-space infrared image is shown with the spatial coordinate on the y-axis of the image and the x-axis representing time. In the right image, estimated heat transfer velocities k are shown, averaged across each detected surface eddy in cm/s for large scale, shear wave coupled turbulence.

Due to the limited image size and the large spacing it is difficult to identify a pattern of streaks. Large gaps arise in rows in which only one or two cold streaks could be identified in the segmentation process. As heat flux estimates are always conducted between the central region of up- and down-welling areas all streaks at the margins are left out in the analysis as the central region can not be determined. This rises of course the question whether a bias to smaller streaks is introduced. In Figure 10.4 the distribution of spacings is shown and it becomes apparent that any cut off would happen at the far tails of the distribution, clearly outside a 3σ interval.

Figure 10.3 shows the relationship between turbulent cell size and heat transfer rates in form of a two-dimensional histogram for the larger scale turbulence. Friction velocities in the two upper figures are 0.64 cm/s and 1.3 cm/s from left to right. The lower figure shows a histogram of data from all wind speed conditions. High frequencies are cut of to show a broader range of eddy sizes and k values and to highlight the general shape of the distribution. It is interesting

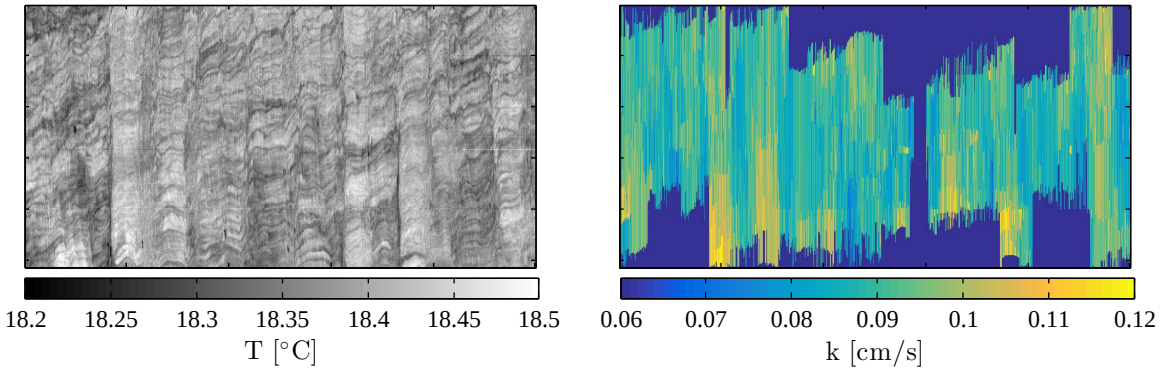

Figure 10.3.: Left: Time-space infrared image at a friction velocity $u^* = 0.74$ cm/s. Right: Estimated heat transfer velocities k, averaged across each detected surface eddy in cm/s for large scale, shear wave coupled turbulence. Due to the large streaks, large gaps are inevitable. No coherent pattern is visible, however, the localization and intensity of detected surface eddies is clearly reflected in the heat transfer velocity estimation image.

to note that heat flux values in relation to eddy sizes follow a relatively narrow curve thereby indicating that there is a close connection between those quantities that has a stronger impact than for example surface velocity. Comparing moderate to higher velocities in the upper two images it becomes evident that even though the curve seems to be relatively universal there is a shift of higher frequencies along that curve. At lower velocities a broader distribution follows a relatively narrow curve. With increasing wind stress the center of the frequency distribution moves up the curve to higher heat flux values broadening slightly in the process. This might indicate the higher variation in surface velocities at higher wind speeds.

The difference in the distributions of cell size and heat flux values between shear induced turbulence and wave shear coupled turbulence is striking. This may well be an indication of two entirely different generation mechanisms. While shear induced turbulence seems to originate from a more random process the roll vortices associated with larger scale cold streaks seem to be created by a far more organized process.

10.2. Impact of turbulence on heat transfer at increasing wind stress

The next figure 10.5 shows averaged heat transfer velocities over wind stress for the experiments 2014 in Aeolotron with and without the surfactant Triton X-100. The presented values are averages of 30 statistically independent images for every wind condition. The analysis was performed separately on small scale, shear induced and larger scale, Langmuir footprints (see Section 6) by separating both turbulent scales according to the life span of their footprints.

All estimates show a consistent behavior with increasing wind speeds. Lines have merely been added to enhance clarity and do not represent theoretic expectations, except for shear turbulence in shear and surfactant conditions where a linear fit describe the observed trend very

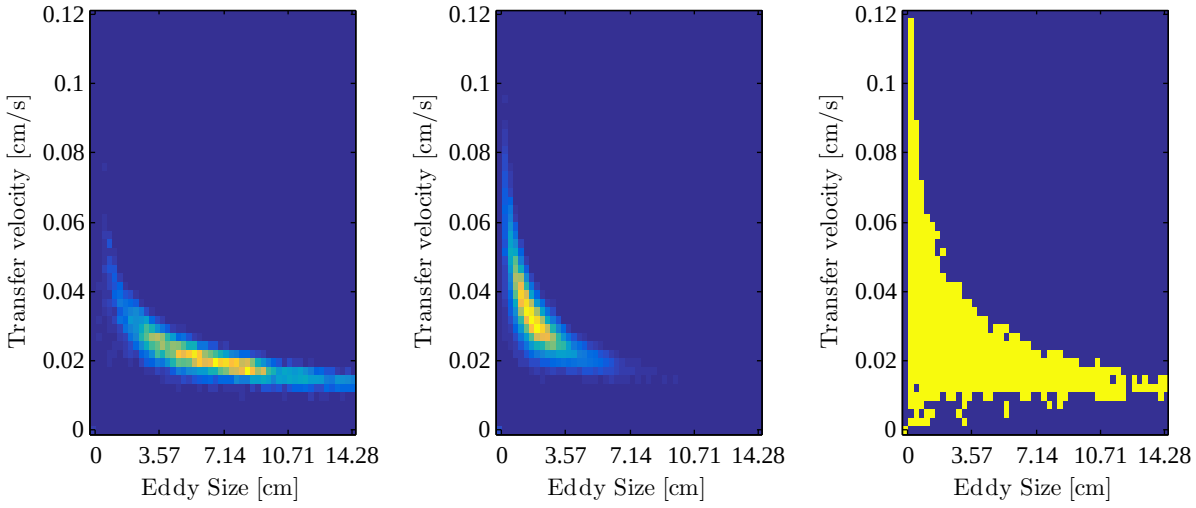

(a) $u^* = 0.6$ cm/s (b) $u^* = 1.3$ cm/s (c) all wind speeds

Figure 10.4.: Two dimensional histograms of heat transfer velocity on the y-axis against eddy size on the x-axis based on the analysis of shear-wave coupled turbulence. In the top row two different wind speeds are shown, the friction velocity increases from left image to right from 0.6 cm/s to 1.3 cm/s. The normalized probability density is color coded. The lower images shows the sum of the histograms of all measured wind conditions. Peak frequencies have been cut off to display the area of the distributions. A direct relation between heat transfer velocity and eddy size indicates the clearly non-random distribution of eddy sizes and points towards the different nature of shear-wave coupled turbulence compared to shear induced turbulence. From intermediate to higher wind stress the frequency distribution shifts from a maximum at larger spacings and lower k values to smaller eddy sizes and higher k values.

well. Transfer rates estimated from small scale turbulent structures (blue circles and crosses in Figure 10.5) show a slow linear increase with friction velocity. Interestingly, values calculated from a clean surface and those from a surfactant covered surface are nearly identical. This again strongly supports the hypothesis of the universal structure of shear induced turbulence discussed earlier.

Green circles and crosses describe transfer velocities from wave shear related turbulence for a clean and surfactant covered water surface respectively. The lowest wind speed at which a detection based on machine learning was possible marks the first data point. This means that at lower wind speeds formation might have been in the process but the footprints were not clear enough to be reliably detected. Therefore, there might still be a contribution of wave shear turbulence which cannot be determined here. For clarity, a zero value has been added at the lowest measured wind speed because in this regime no trace of Langmuir circulations had been detected. Therefore the assumption of a zero impact seems justified.

A relatively steep ascend of estimated heat transfer rates occurs around a friction velocity of $u^* \approx 1$ cm/s for the clean water case. This wind stress condition also marks the appearance of the first microscale breaking waves. Looking back to the frequency distribution of heat flux values in relation to turbulent cell size it is noticeable that the shift of high frequencies from the

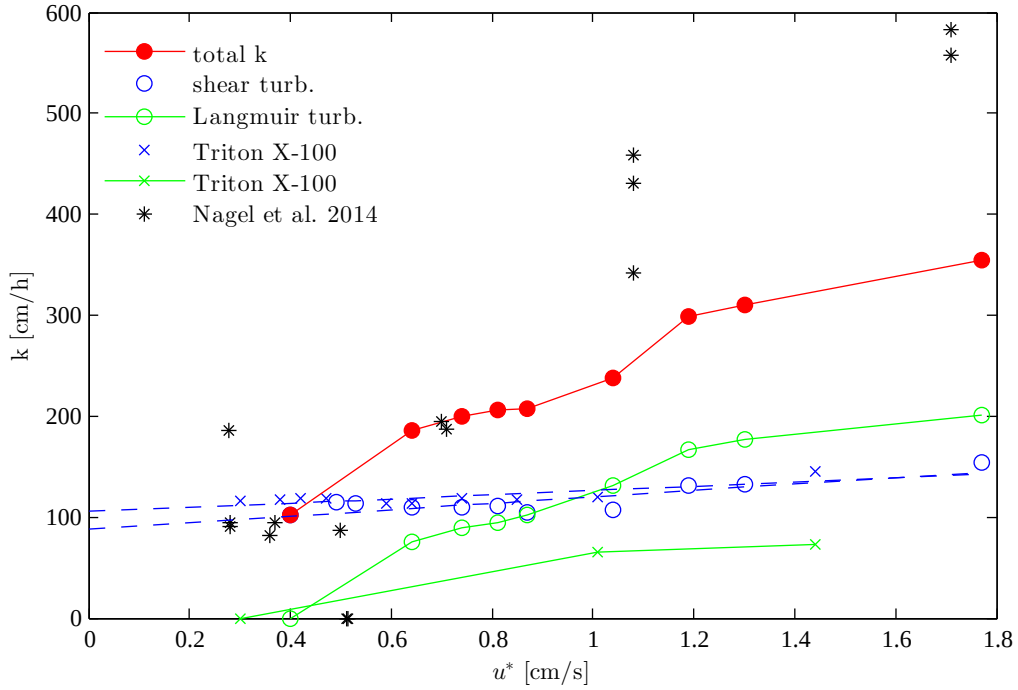

Figure 10.5.: Heat transfer velocities against water sided friction velocity u^*. Blue symbols indicate clean surface condition, cyan symbols indicate surfactant covered surface. Blue circles and triangles are averages of estimated transfer rates from small scale and larger scale turbulent structures respectively. Blue dots show total heat transfer rates (added small scale and larger scale values according to eddy superposition). Black stars are heat exchange rates from ACFT [Nagel et al., 2014] measured in the same facility under the same wind wave conditions. Cyan open circles and triangles depict transfer velocity estimates based on shear turbulence and Langmuir circulation, respectively. The fast non-linear increase of transfer rate estimates based on Langmuir turbulence is noteworthy. Langmuir circulation could only be detected at friction velocities above 0.5 cm/s, in the clean surface cases, and above 1 cm/s in surfactant cases, as below the detection of streaks was not possible, even though streaks might have been in formation. Therefore a small contribution might be present at lower wind speed, that is not shown here.

lower branch to higher heat flux values also happens at this condition, between $u^* = 0.9$ cm/s and $u^* = 1.3$ cm/s.

For the measurements with added Triton X-100 the first detectable large scale streaks appear at these stress values. The estimated heat transfer rates are overall lower than in the clean surface cases but especially at higher wind stress. The reason seems to lie in lower heat flux estimates from wave shear coupled turbulence. Why exactly heat flux values stay so low even when mean square slope values have reached nearly the same values is not quite clear but might be associated with the altered surface dynamics.

According to the concept of eddy superposition both scales together form the total impact of the surface turbulence pattern. Thus, blue dots in Figure 10.5 show the total estimated heat transfer rate for the clean surface case. As a comparison, black stars show heat transfer rates measured with the active controlled flux technique (ACFT) by Nagel et al. [2014] in the same facility under the same conditions.

Table 10.1.: Results of the analysis of the surface heat pattern, clean water case. In tables 10.1 and 10.2, u is the wind speed in meters per second as measured in the facility circa one meter above the water surface, u^* is the water sided friction velocity in centimeters per second, $\overline{u_s}$ is the averaged surface velocity in cross wind direction in centimeters per second, $\overline{T_b}$ and $\overline{T_s}$ are the averaged estimated bulk temperature and the average surface temperature respectively, $\overline{k_{small\ scale}}$, $\overline{k_{larger\ scale}}$ and $\overline{k_{total}}$ are heat transfer rates in centimeters per hour estimated from the small scale and larger scale turbulence and the total estimated heat transfer rate respectively. Heat transfer velocity estimates based on the detection of Langmuir circulation only starts at a wind speed of $u = 4.2$ m/s, as below the detection of streaks was not possible, even though streaks might have been in formation.

Clean water surface							
u	u^*	$\overline{u_s}$	$\overline{T_b}$	$\overline{T_s}$	$\overline{k_{\mathrm{shear}}}$	$\overline{k_{\mathrm{Langmuir}}}$	$\overline{k_{total}}$
2.4	0.40	3.4	19.09	18.73	102	-	102
3.2	0.49	4.3	18.96	18.65	114	-	114
3.5	0.53	4.7	18.91	18.61	114	-	114
4.2	0.64	5.7	18.87	18.52	110	76	186
4.8	0.74	6.7	18.88	18.47	110	89	199
5.1	0.81	7.3	18.81	18.36	111	95	206
5.4	0.87	7.8	18,88	18.38	105	102	207
6.0	1.04	8.9	18.70	18.19	107	131	237
6.5	1.19	10.1	18.60	18.22	132	167	299
7.0	1.30	11.3	18.53	18.17	133	178	310
8.3	1.77	14.6	18.52	18.08	154	201	355

At low wind speeds, heat transfer rates match reasonably well. With increasing wind stress a gap increases between values measured from ACFT and the here presented estimates based solely on footprints of coherent turbulence. This fits very well to earlier observations by for example Zappa et al. [2004] who found microscale breaking to be the dominant effect for transfer processes at moderate wind speeds. Zappa et al. [2004] suggests in this regime a contribution of micro scale breaking of 75 % to total transfer. Peirson et al. [2014] estimate the impact a little lower, to 50 % of the total transfer. This is approximately what the present analysis suggests, in the highest wind speed case the contribution of near surface turbulence amounts to approximately 60 % of the value determined from ACFT.

Error bars have been excluded in Figure 10.5. An example error analysis for a single eddy estimate is shown in the Appendix A.2. As the values in Figure 10.5 are derived from spatial and temporal averages, the statistical error on the estimated transfer rates is small. However, systematic error are difficult to quantify and arise from the model assumptions, streak detection and additional processes that are not accounted for.

Figure 10.6 highlights the ratio of the contribution to heat transfer by small scale, shear induced, turbulence and larger scale, wave shear coupled, turbulence. $k_{\mathrm{Langmuir}} - k_{\mathrm{shear}}$ against u^* shows a strictly positive trend. At lower friction velocities shear stress is clearly the dominant process. As friction increases at higher wind speeds larger scale turbulence becomes more important. The transition zone, which also exhibits a steeper ascend, is at approximately $u^* \approx 1$ cm/s. Finally, turbulence caused by wave wind coupling causes clearly higher transfer rates.

Table 10.2.: Results of the analysis of the surface heat pattern, surface slick condition. Heat transfer velocity estimates based on the detection of Langmuir circulation only starts at a wind speed of $u = 7.0$ m/s, as below the detection of streaks was not possible, even though streaks might have been in formation

	Triton X-100						
u	u^*	$\overline{u_s}$	$\overline{T_b}$	$\overline{T_s}$	$\overline{k_{\text{shear}}}$	$\overline{k_{\text{Langmuir}}}$	$\overline{k_{total}}$
2.4	0.30	2.1	19.57	19.23	116	-	116
3.2	0.38	2.3	19.56	19.21	117	-	117
3.5	0.42	2.4	19.42	19.08	119	-	119
4.2	0.47	2.7	19.60	19.23	118	-	118
4.8	0.59	2.9	19.64	19.24	113	-	113
5.4	0.64	3.2	19.65	19.22	114	-	114
6.0	0.74	3.8	19.70	19.27	118	-	118
6.5	0.85	4.1	19.74	19.28	117	-	117
7.0	1.01	5.3	19.76	19.29	120	66	186
8.3	1.44	8.4	19.80	19.30	145	72	217

10.3. Summary

The footprints of coherent turbulence appear in infrared images of the water surface. The analysis of those footprints provides a means to estimate heat transfer rates based solely on the impact of single turbulence producing processes. In this approach, image processing techniques have been combined with eddy renewal models and have produced heat flux estimates with a high spatial resolution. This provided for the first time a method to relate the scale and intensity of a surface eddy to its impact on heat transfer.

It has been shown that the adopted models result in realistic estimates of heat transfer rates and that the concept of superposed eddies seems to describe the state of the water surface reasonably well. Estimated transfer velocities based on shear induced or wave-shear coupled turbulence very likely represent the impact of one process only. Therefore, the combination of both results is legitimate and provides realistic values, compared to measurements in the same facility.

Shear turbulence and wave-shear coupled turbulence exhibit very different characteristics regarding size and estimated heat transfer rates. While the frequency distribution of eddy sizes and transfer rates of shear turbulence points towards a random process, wave-shear coupled turbulence seems to appear only on very distinct scales and associated transfer velocities.

The impact of surfactants is consistently reflected by the analysis. A change of the dynamics of the water surface by damping capillary waves directly translates into changes of the turbulent regime and lower estimates of transfer velocities. The comparison of surface turbulence at clean and surfactant covered water surfaces strongly indicates that at low wind speeds shear induced turbulence alone is responsible for a considerable fraction of the transport of heat across the air-sea interface. However, as wind stress increases wave shear coupled turbulence plays a major role in the transition zone and the combination of both turbulent structures produces very reasonable

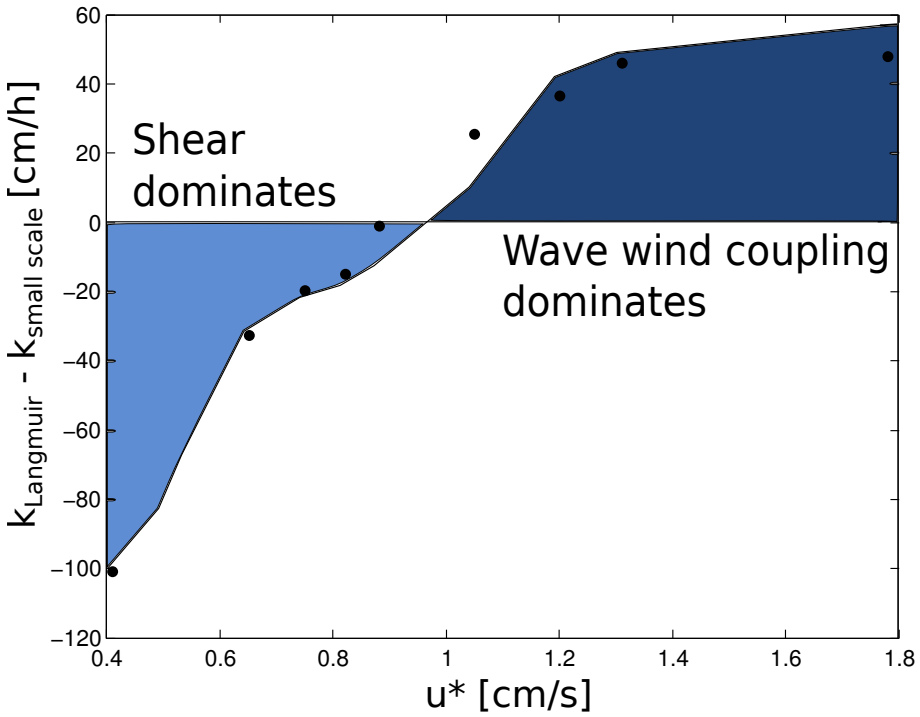

Figure 10.6.: Difference between estimated heat transfer rates from small scale and large scale turbulent structures is shown on the y-axis against friction velocity on the x-axis. The results are from Figure 10.5, clean surface conditions. At low friction velocities, negative values indicate that shear stress is clearly the dominant process. As friction increases at higher wind speeds larger scale turbulence becomes more important. The transition zone is at approximately $u^* = 1$ cm/s.

heat transfer velocities.

Finally, at even higher wind speeds turbulence cannot explain observed transfer rates any longer, as processes like micro scale breaking now dominate the total transport. The impact of surface turbulence in this regime has been estimated to be approximately 60 %.

11. Discussion

In this work, the impact of various mechanisms on the surface dynamics, its characteristic scale and the impact of surface eddies on heat transfer have been examined. From the analysis of the surface temperature pattern and derived quantities, such as surface velocity fields and estimated bulk temperatures, a number of turbulence producing processes have been identified to determine heat transfer rates at low to moderate wind speed. Turbulence producing mechanisms have been classified into the main groups of shear driven, wave shear coupled turbulence and directly related to microscale breaking waves, all of which cause footprints of characteristic shapes, sizes and life times in infrared images. With increasing wind stress, different turbulent mechanisms interact, depending on surface conditions and wave field. As a result, turbulent regimes develop and are replaced as the surface dynamics undergo a constant change. In the following sections, a description of the main turbulent regimes is given, based on the results of Chapters 7 - 10.

11.1. Turbulence producing mechanisms at the water surface

Shear induced turbulence

Shear induced turbulence creates a characteristic temperature pattern on the water surface, compare Figures 7.1 and 7.2. It causes the characteristic fish scale pattern in the infrared images [Handler et al., 2001; Tsai et al., 2005] and presumably small scale divergence and convergence along the observed cold streaks and plumes. However, shear turbulence did not appear in the estimated flow fields. Due to the aperture problem this motion cannot be detected in the optical flow based techniques employed in this thesis. Shear stress was confirmed to be the generating mechanism ([Kitaigorodskii, 1984] and Section 8.1.1) and shear induced turbulence was shown to be insensitive to changes in the surface wave field ([Schnieders et al., 2013] and Section 8.1.1). Shear induced turbulent cells are relatively small and decrease in size with increasing wind stress but only until a plateau is reached [Schnieders et al., 2013]. The detailed fundamental processes for this observation are currently unknown. Possible explanations include the partition of shear stress in tangential stress and wave form drag as described in Banner and Peirson [1998]; Peirson and Garcia [2008] or a minimum coherent cell size [Schnieders et al., 2013]. In previous studies a continuous decline had been suggested [Scott et al., 2008] but no systematic analysis of cell sizes has been conducted over a sufficiently wide range of wind speeds to compare to.

Eddy sizes exhibit a log-normal frequency distribution similar to those observed for low speed streaks near a no slip wall [Smith and Metzler, 1983]. Furthermore, the log-normal distribution

indicates random forces that cause the production of the cold streaks which are in some way proportional to the streak spacing. With increasing wind stress, the fish scale pattern exhibits coherent eddies with very homogeneous size and temperature gradients (compare Section 10.1.1 and Figure 10.2 and [Schnieders et al., 2014]) which might indicate that a lower limit of eddy sizes is reached. In accordance, the frequency distributions of streak spacings show decreasing variance, σ.

Langmuir circulations

The footprints of Langmuir circulations have been studied with respect to size and surface velocity variation. The spacing of the elongated convergent streaks matches those observed in studies of small scale Langmuir circulations very well [Caulliez, 1998; Melville et al., 1998; Schnieders et al., 2013; Veron and Melville, 2001]. It also matches the predictions from neutral stability theory to describe Langmuir circulations ([Leibovich and Paolucci, 1981; Schnieders et al., 2013] and Figure 8.5). A further analysis of the spacings of Langmuir induced cold surface streaks showed that Langmuir cell sizes directly depend on the wave field and exhibit far less variation than shear turbulence.

The evolution of high-speed streaks, i.e. higher surface velocities within convergence zones, was observed for the first time in infrared imagery and confirms the findings from previous studies using tracer particles or bubbles ([Gemmrich and Hasse, 1992; Kukulka et al., 2009; Smith, 1989] and Section Figure 7.8). The resulting roll vortices are very stable on the order of seconds, and the overturning process is relatively slow. Streak like surface divergence areas can be visualized from surface flow fields, if short timescale movements are canceled out by averaging over a longer period. Those convergence areas coincide with cold and warm areas in infrared images and confirm the down-welling and upwelling process, respectively. The evolution of Langmuir circulation is marked by the appearance of defined convergence that coincides with distinct cold streaks. The correlation of high surface temperatures and convergence, i.e. the upwelling area, is broader and weaker. This corresponds well to the finding of distinct narrow convergence and broader divergence of Langmuir circulations by Chini [2008].

Microscale breaking

Microscale breaking waves cause a considerable amount of turbulence. The main characteristic feature is their spilling region [Banner and Peirson, 1998; Peirson and Garcia, 2008; Peirson et al., 2014; Zappa et al., 2001] with a characteristic convergence zone at the toe and the following subduction and exhilaration of surface velocities [Peirson et al., 2014; Schnieders, 2011]. The exhilaration of surface velocities to wave phase speed has been observed and described previously and could be confirmed here (compare Figure 7.7).

Roll vortices on the back side of microscale breaking waves have been described by Handler et al. [2012]. Here, those vortices have been observed to differ considerably in size and life

time from Langmuir circulations. Thus, intensity and resulting surface divergence are a distinct feature of the surface flow field. Similar streaks were observed also in conditions with mechanical waves only, without any wind stress. This indicates that the Craik Leibovich mechanism [Leibovich and Paolucci, 1981] responsible for the formation of Langmuir circulations does not explain those streaks. As those streaks have only been observed at the lee side of microscale breaking waves, it is classified as microscale breaking related.

11.2. Characterization of turbulent regimes

With growing wind stress the dominant turbulent features change and so does the surface dynamics. Table 11.1 shows an overview of the main regimes that evolve successively with increasing wind stress. In the upper part of the table the regimes are divided as observed in clean surface conditions. In the "surfactants" row, arrows indicate the shift of the observed regimes relative to the friction velocity. Surfactants mainly reduce surface roughness and therefore delay wave growth. Thus, the major effect is that all wave related regimes are entered at higher friction velocities but still in the same order and with very similar footprints in infrared images and velocity fields. The most prominent effect becomes visible at relatively low friction velocities, as shear stress is far more dominant if wave growth is delayed. Reynolds numbers increase with increasing wind stress and therefore increasing surface velocities throughout this range of wind speeds. The flow is clearly turbulent already at relatively low wind speeds.

The observed turbulent regimes can be separated into four parts: The first part at low friction velocities with $u^* < 0.4$ cm/s is dominated by *free convection*. The surface Richardson number as defined by Soloviev and Schlüssel [1994] is clearly above the critical value of $Rf_{cr} = 1.5 \cdot 10^{-4}$, which means that convection is driven by the heat flux at the water surface and dominates over shear driven turbulence. No surface waves are visible, yet. The surface heat pattern consists of a pattern of up and down-welling areas that is characteristic of free convection but slightly sheared due to wind stress. The pattern itself looks very similar to the familiar shear induced fish scales but the high surface Richardson number clearly shows that a strong total heat flux causes free convection which is the dominant process here. In the presence of a surface slick the total heat flux is slightly lower and the next regime is entered at a slightly lower friction velocity of $u^* = 0.3$ cm/s instead of $u^* = 0.4$ cm/s as in the clean surface case.

At increasing wind stress, the turbulent state enters the *shear dominated regime*. In the infrared images the fish scale pattern dominates, which is characteristic of shear induced turbulence. The velocity field is dominated by small capillary ripples. Furthermore, the beginning of the formation of high speed streaks is visible. Those areas of higher velocity coincide with the development of large scale cold streaks, visible in the infrared images. This regime can be considerably extended up to friction velocities of about ≈ 1 cm/s if a surface slick dampens capillary waves, instead of ≈ 0.5 cm/s in a clean surface case.

At higher wind stress and friction velocities, around $u^* = 1$ cm/s in clean surface conditions,

Table 11.1.: Summary of the results from Chapters 7-10. Turbulence producing mechanism at the water surface are organized into distinct turbulent regimes that evolve with increasing wind stress. This concept incorporates all observed features of the temperature pattern and estimated flow field and also allows to illustrate the impact of surfactants on the previously defined regimes. The regimes are named after the dominant turbulent process, which is the process with the strongest impact on heat transfer velocities, even though most processes can be observed simultaneously.

	Free convection	**Shear dominated**	**Transition zone**	**Microscale breaking**
involved turbulent mechanism	free convection	shear turbulence, formation of Langmuir vortices	small Langmuir circulation, shear turbulence (plateau area)	wave breaking, roll vortices, Langmuirs, shear (often subducted)
IR images	Reilly Bénard cells	characteristic fish scales, not very pronounced large scale streaks	large scale cold streaks, very stable, small fish scales	spilling of microscale breaking waves, large scale streaks, small homogeneous fish scales
velocity field / divergence	aperture problem	capillary ripples in velocity field and divergence	capillary ripples, mean divergence shows large scale high speed streaks	breaking characteristics, streaky convergence zones
Reynolds number	2000	2500	3500	5000
Surface Richardson number	10^{-3}	10^{-5}	10^{-6}	10^{-7}
Wave height	≈ 0	1 cm	6 cm	15 cm
Surfactants	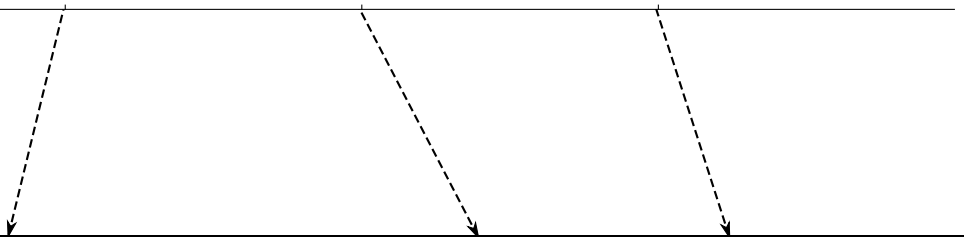			
Friction velocity u^* [cm/s]	0	0.4	1	1.5

the dynamics of the water surface has changed. Therefore, this regime is called *transition zone*. Small gravity waves form and the first microscale breaking events are clearly visible in the infrared images, although it is not the defining feature. Focusing on the characteristic turbulent mechanisms, both shear turbulence and small Langmuir circulations are equally important. Here, the scales of shear turbulence enter the plateau area as seen in Figure 8.3. At the same time, very pronounced cold surface streaks, which show all characteristics of Langmuir circulation, are a distinct feature of the surface heat pattern. The surface velocity field is, however, far more modulated by growing waves, also indicating that a large fraction of the shear stress is transformed to wave form drag and, thus, tangential stress does not grow equally [Peirson and Garcia, 2008]. Furthermore, surface divergence caused from small Langmuir circulations becomes clearly visible in surface divergence images if averaged over a time interval. Surfactants delay the transition from shear dominated to Langmuir dominated phase and further to microscale breaking. This means that the impact of surface slick on the water surface leads to the most pronounced changes in the interaction of surface processes at this *transition zone* at intermediate wind speeds.

At even higher wind stress *microscale breaking* waves become the defining feature of the water surface [Peirson et al., 2014; Zappa et al., 2001] and dominate the infrared images and the velocity field. In the infrared images, stable Langmuir caused cold streaks are still visible, even though they sometimes seem to collapse due to wave breaking. Also the fish scale pattern is still visible, though frequently subducted by the spilling region of microscale breaking waves.

In the next section the implications on transfer rates will be explored based on the previously defined regimes and identified surface processes.

11.3. Impact of small scale surface turbulence on heat exchange rates in changing surface conditions

Commonly employed parameterizations of heat and gas transfer rates, e.g., wind speed and mean square slope, are subject to large variations. None of the commonly employed parameters explains all deviations from predicted transfer rates, especially if additional factors like surface film or limited fetch alter the fluid dynamics of the surface. Therefore, in this work, a mechanistic approach has been chosen. The impact of individual processes on heat transfer rates is investigated. The results help to explain under which conditions certain parameterizations are expected to give accurate results or cannot parameterize the dominant processes, thereby being able to predict deviations from current parameterizations.

The infrared images of the water surface and the derived surface flow fields can identify dominant processes. Gradients in the temperature pattern correlate to a certain degree with transfer velocities. However, to infer reliable estimates of the transfer velocity a conceptual model is needed. In this work, the concept of eddy renewal has been adapted to the characteristic turbulent regimes as observed from the thermographic data. Resulting transfer velocity estimates

have been shown to be realistic if compared to direct measurements.

The central remaining question is, if the study of near surface turbulence can provide predictions on the impact on exchange rates if the state of the sea surface is changing? Starting from the process and not the parameters and taking the regimes defined in Section 11.1, the picture that emerges is the following:

Shear dominated regime

At low wind stress, shear induced turbulence is the main contributor to enhanced transfer rates. Estimated heat exchange rates based on the fish scale temperature pattern can explain the total measured heat flux (compare Section 10.2).

As shear turbulence directly depends on shear stress, the friction velocity, u^*, is a natural choice to scale transfer rates in this regime. Here, a linear relationship between estimated transfer velocities and friction velocity was found. If the water surface is covered by surfactants, the onset of waves is delayed (see Table 4.2). This causes an extension of the shear dominated regime in the surfactant cases. As a result, the linear relationship between friction velocity and wind stress persists until the first waves form on the water surface. According to Kiefhaber [2014], in the presence of surfactants, transfer rates at low wind stress are independent of mean square slope and therefore the wave field. This is confirmed here, as in this regime, wave independent wind stress is the dominant driver of exchange rates.

A comparison with directly measured heat transfer rates via the active controlled flux technique measured by Nagel et al. [2014] as proposed by Jähne et al. [1989] in the same laboratory and under very similar wind-wave conditions showed an overall good agreement.

Values at low wind speeds seem high compared to current parameterizations and field measurements, however, local variations of wind speed in the laboratory are described in Bopp [2014] and suggest higher wind stress at the location of the infrared camera. Another possible reason why transfer rates in the laboratory can be higher than expected compared to field measurements might be an additional enhancement due to free convection. Even though the surface Richardson number is below the threshold, a (small) additional enhancement seems likely.

Transition regime

This regime is characterized by a transition from dominant shear turbulence to Langmuir circulations as the most pronounced feature of the surface temperature pattern. The implication for exchange is a significant non-linear increase in heat transfer rates due to Langmuir circulations in contrast to the linear increase of transfer rates due to shear turbulence. Clearly detectable Langmuir circulation induced footprints appear at friction velocities of $u^* \approx 0.6$ cm/s for a clean surface. Therefore, the associated increase of transfer velocities is estimated to take place at the same friction velocity. However, the detection threshold is a critical value and a (small) contribution of Langmuir circulations, which are in the process of formation, at lower wind stress

cannot be excluded.

If the water surface is covered by the surfactant Triton X-100, first visible Langmuir footprints start appearing at higher friction velocities of $u^* \approx 1$ cm/s. Thus, also the increase of transfer velocities due to Langmuir circulations happens later and has been estimated to be weaker than in the clean surface case. A possible explanation is that surface films have the property to dampen convergent flow. This might explain why the convergence regions of Langmuir circulation appear to be weaker which also translates to lower transfer rates. As a result, surfactants have a most pronounced effect in this regime and contribute to considerably lower transfer rates in this range of wind speeds.

As the characteristics of Langmuir circulation induced roll vortices depend on shear stress and waves, parameterizations with wind speed or mean square slope might be expected to give good results. Mean square slope has been shown to be a good parameter in this regime [Jähne et al., 1984] and provides good results [Frew et al., 2004; Krall, 2013]. The explanation may be that for a clean water surface Langmuir circulation are directly related to the onset of capillary waves [Veron and Melville, 2001]. Kiefhaber [2014] pointed out that MSS provides generally a good parameterization, at low wind speeds and in the presence of surfactants, however, its reliability decreases.

In this regime, heat transfer rates based on a combination of shear turbulence and Langmuir circulation match measured transfer rates by Nagel et al. [2014] reasonably well (compare Section 10.2). This means that at intermediate wind speeds, exchange can be considered as mediated by a combination of shear turbulence and small Langmuir circulations.

Microscale breaking regime

In this regime, turbulence introduced by microscale breaking waves clearly dominates the dynamics of the water surface. Heat transfer rates estimated from turbulent structures alone make only about 50 % and less of the total transfer for increasing wind speeds of the measured transfer rate. This is in good agreement with the findings of Zappa et al. [2002] and Peirson et al. [2014], who found microscale breaking to be the dominant factor for transfer across the air water boundary at moderate wind stress.

The intensity of Langmuir circulations decreases as frequent microscale breaking seems to destroy the stable vortices on these scales (this effect has previously been described by Mizuno [2011]).

Instead, roll vortices appear at the lee side of breaking waves [Handler et al., 2012] that differ in their characteristics from Langmuir circulations by their spacing but also by their stability. These roll vortices induce high cross wind surface velocities and leave footprints in the divergence images that have the same magnitude as the spilling process.

Impact of surfactants

One of the challenges is the accurate parameterization of exchange rates in the presence of surfactants. This surface state occurs frequently in the ocean, especially in areas with high biological activity, and is therefore also highly interesting with respect to the exchange of biologically produced gases like Dimethylsulfate (DMS) [Liss et al., 2014].

The mechanistic approach chosen in this work indicates that the turbulent state of the water surface is altered significantly in the presence of surfactants. The shear dominated regime extends to considerably higher wind stress as the surfactants dampens surface waves and, therefore, the onset of Langmuir circulations. The impact of shear turbulence on heat exchange seems to grow linearly with increasing friction velocity. By contrast, the transition regime is characterized by a fast non-linear increase of estimated transfer velocities due to the onset of Langmuir circulations. This in turn means that any delay of the transition regime translates into a delayed increase of transfer rates and therefore lower overall values. As a result, this study suggests that the strongest impact of surfactants on transfer rates is observed at intermediate wind stress. Commonly described reduction of transfer rates in the presence of surfactants in gas transfer measurements [Krall, 2013; Kräuter, 2011] can be explained by this mechanism.

11.4. Implication for larger scales and the field

The ultimate goal of all laboratory measurements is to derive processes and mechanisms that can be transfered to the open ocean and thereby help to understand the more complicated environment in field conditions. The characteristics of the small scale structures, namely shear induced turbulence and small Langmuir circulations, have been tested under various different wind-wave conditions in different laboratories. Both, shear induced turbulence and Langmuir circulations, have been shown to have a universal scaling of turbulent cell sizes, which is independent of the geometry of the channel.

At low to very low wind speed, wind stress and small gravity waves are the main driving forces of enhanced transfer velocities. Therefore, it can be expected that the water surface of the ocean is dominated by the same regimes as defined in this work based on laboratory measurements at low wind stress, e.g., within a wind speed range that has been labeled shear dominated regime and the transition zone. This means that also in the open ocean shear induced turbulence can be expected to be the main driver for enhanced exchange rates at very low wind speeds. If surfactants are present on the water surface, e.g., in areas with high biological activity, this regime is extended. This finding could help incorporating slick covered ocean areas into predictions of gas exchange by assuming a linear increase in gas exchange instead of a faster increase of the transfer rates predicted by the wind speed parameterizations for a clean surface.

However, as the transition zone is characterized by Langmuir circulations and growing gravity waves, it is undergoing continuous change as the wind increases. At the open ocean, Langmuir circulations with far bigger spacings and lengths develop, depending on wave conditions. As

in the laboratory all processes are limited by the geometry of the facility, the wave field is significantly different from the one in the open ocean. While small scale Langmuir circulations are small enough not to be influenced by the width of the channel, all scales of the order of the channel width and above can naturally not be studied in the laboratory.

In this study, it has been found that Langmuir circulation cause distinct surface convergence zones which lead to the down-welling of fluids. In the field and on larger scales, this leads to mixed layer deepening [Li and Garret, 1997]. Belcher et al. [2012] point out that this important effect is not accurately represented in most climate models. Measurement of the convergence could provide important information on the down-welling strengths and provide a parameterization of the mixing process to improve climate models.

In this work, it has been shown that Langmuir circulations are an important driver of increased transfer rates at increasing wind stress before microscale breaking becomes the dominant feature. Langmuir circulations appear on a wide range of scales in the ocean and form an important feature of the top layer of the surface ocean (like mixed layer deepening, high speed streaks, influence of cross wind currents) and play a crucial role in air-sea interaction processes. However, little is known about the dominant scales over the full range of observed spacings. The remaining question is, what effect do Langmuir circulations of various scales have on heat and gas transfer rates and which scales contribute most to enhanced transfer rates? The cell size of Langmuir circulations depends strongly on environmental conditions such as wind speed and wave field.

Langmuir circulations have been observed in airborne measurements leading to image sizes of up to several kilometers by Marmorino et al. [2005, 2007, 2009] and Zappa et al. [2004]. Here, the information from cold streaks caused by Langmuir Circulation have been used to estimate the depth of the surface mixed layer.

So far there have been no measurement campaigns that cover both small scale structures and large scale structures within one study. A comparison of strength and occurrence of different sizes of Langmuir circulations is therefore still missing. The study of intermediate scaled Langmuir circulations would provide a link between small scale measurements as described here and large scale satellite images and facilitates the interpretation of widely available satellite images and the inference of subsurface temperatures.

12. Conclusion and Outlook

12.1. Conclusion

Within this work, processes enhancing air-sea transfer velocities have been investigated with respect to their characteristic features and impact on exchange. A special focus has been on low to moderate wind speeds with and without surface active material reducing surface roughness. Measurements were conducted in the controlled environment of the laboratory and data from different laboratory facilities were evaluated in a range of different wind wave conditions.

Passive Thermography has been shown very well suited for the mechanistic analysis of surface processes as the footprints of the underlying turbulence are displayed in infrared images. The visualization of surface convergence and divergence allows for the derivation of detailed information about the dynamic state of the water surface with a high spatial and temporal resolution provided by high-end infrared cameras.

The analysis of the infrared images sequences was conducted based on image processing techniques such as motion estimation and classification of the surface temperature pattern. For the accurate estimation of surface flow fields existing optical flow based algorithms were adapted to infrared images of the water surface. The classification of the surface heat pattern was conducted based on machine learning with the software tool Ilastik [Sommer et al., 2011].

Three main findings of this work are:

Identification of dominant turbulent regimes

Turbulence producing mechanisms have been classified into the main groups of shear driven, wave shear coupled turbulence and directly related to microscale breaking waves, all of which cause footprints of characteristic shapes, sizes and life times in infrared images. The identification of dominant turbulent regimes is based on the results of the analysis of the infrared images and the resultant flow field, with surface divergence estimates, the classification of the surface temperature pattern and the estimation of bulk temperatures.

With increasing wind stress depending on the total heat flux, the first wind-driven turbulent regime is dominated by *shear turbulence*. This regime extend up to friction velocities of $\approx$ 0.6 cm/s in the clean surface cases. If surfactants suppress capillary waves, this regime extends further to $\approx$ 1 cm/s. In this regime the transfer rate is estimated to increase slowly and linearly with wind stress.

As wind stress increases and the first small gravity waves form, small *Langmuir circulations*

are a dominated feature of the water surface. Associated with this transition in the turbulent regime is a non-linear increase of heat transfer rates. In the presence of surfactants this regime is considerably delayed with respect to wind stress and also the overall impact on transfer seems to be weaker.

At moderate wind speed and friction velocities of above ≈ 1.2 cm/s, *microscale breaking* waves dominate the surface dynamics. Constant microscale breaking weakens Langmuir circulations. In this regime, turbulent processes associated with microscale breaking are responsible for the major part of enhanced transfer rates, at least in the studied laboratory data.

Definition of characteristic features of turbulent processes

The spacing of cold streaks at the water surface is suggested as a practical feature to describe the size of turbulent structures. As the spacing is determined independently for small scale, shear induced, and large scale, wind wave coupled, turbulence, it also provides a means to distinguish both processes. For shear induced turbulence, the analysis of the spacing yields a decreasing turbulent cell size until a minimum is reached. This plateau area starts at intermediate wind stress and coincides with growing gravity waves. The frequency distribution exhibits log-normal behavior throughout all wind speeds. Langmuir footprints, in contrast, appear on one dominant eddy size that directly depends on wind wave conditions.

The eddy renewal model describes the water surface as densely packed with surface eddies. In this work the conceptual model has been extended with the addition of eddy superposition. The surface temperature pattern can thus be described assuming a superposition of larger scale and smaller scale eddies. This concept was shown to adequately represent processes at the water surface in low to moderate wind stress.

Impact of individual processes on air-sea transfer under varying surface conditions

The estimation of the impact of individual processes on air-sea transfer rates has been a main focus in this work. For the first time, a method is presented to relate the scale and intensity of a surface eddy to its impact on heat transfer.

- Shear induced turbulence cannot be neglected and is a major contributor to enhanced transfer rates at low wind stress. Its relevance increases if the surface is covered by surfactants as the onset of waves is delayed. Transfer rates associated with shear induced turbulence are shown to be linearly dependent on wind stress.
- Langmuir circulations play a major role at intermediate wind stress, when the spacing of shear induced turbulence has entered a plateau area and cause a significant increase of transfer rates.
- Microscale breaking is a dominant contributor at moderate wind stress and is responsible for approximately 50% and more of the transfer rate.

12.2. Outlook

Future goals in the exploration of turbulence producing mechanism at the water surface include three main goals: The better fluid dynamical understanding of surface processes, the investigation of the comparability of heat and gas exchange and the transition of a mechanistic approach to larger scales and field measurements.

A further analysis of the turbulent structures at the air-sea interface would clearly benefit from three dimensional velocity fields. This would especially complement the here applied eddy renewal model and could give a closer insight into the mechanisms that drive surface eddies. Furthermore, only the knowledge of three dimensional velocity fields allows the calculation of critical quantities like kinetic energy dissipation rate.

Heat exchange has been shown previously to be closely related to gas transfer, e.g., [Nagel et al., 2014]. Techniques visualizing gas transfer, as for example proposed by Kräuter et al. [2014], provide a direct comparison of individual turbulent structures in heat and gas transfer. This comparison allows an evaluation of the different impact of individual processes on heat and gas exchange.

Finally, to allow the findings about small scale turbulent processes to be incorporated into global models the step to larger scales and field measurements is crucial.

Exploring ocean turbulence with an octocopter

Thermography on an octocopter is an ideally suited method to study the surface heat pattern on a variety of scales in the ocean with a higher resolution than possible with air planes but without the limited footprint of a camera on board a ship.

In a joint project with the science education association SeaNetworks e.V based at the Alfred-Wegener-Institute for polar and marine research in Bremerhaven an octocopter is currently being built. One goal of this collaboration is to detect Langmuir circulations of various sizes and thus relate scale and intensity of the circulation to environmental parameters such as wind stress and wave field. Additionally, this project aims to contribute to education in science.

The overall objective of this project is to obtain a quantitative understanding of how submesoscale near surface turbulence enhances exchange rates between the atmosphere and the ocean. It is our goal to identify the scales on which wave current coupled turbulence, Langmuir circulations, appear and more important which scales have the biggest impact on surface flux of heat and gas. This will help to determine the relevant scales of ocean turbulence to explain the high spatial variability in air-sea interaction processes. Relating this finding to the prevailing surface conditions will be an opportunity to parameterize the impact of near surface turbulence on heat and gas transfer rates based on a mechanistic understanding of involved processes.

Bibliography

W. Alpers. The damping of ocean waves by surface films: A new look at an old problem. *Journal of Geophysical Research*, 94(C5):6251–6265, 1989.

P. Anandan. A computational framework and an algorithm for the measurement of visual motion. *International Journal of Computer Vision*, 2(3):283–310, 1989.

E. Arnaud, E. Mémin, R. Sosa, and G. Artana. A fluid motion estimator for schlieren image velocimetry. In *Computer Vision-ECCV 2006*, pages 198–210. Springer Berlin Heidelberg., 2006.

W. Asher. The sea-surface microlayer and its effect on global air-sea gas transfer. In *The Sea Surface and Global Change. 1st ed. Cambridge*, pages 251–286. Cambridge University Press, 1997.

W. E. Asher, A. T. Jessup, and M. A. Atmane. Oceanic application of the active controlled flux technique for measuring air-sea transfer velocities of heat and gases. *J. Geophys. Res.*, 109: C08S12, 2004.

M. A. Atmane, W. Asher, and A. T. Jessup. On the use of the active infrared technique to infer heat and gas transfer velocities at the air-water free surface. *J. Geophys. Res.*, 109:C08S14, 2004.

G. Aubert, R. Deriche, and P. Kornprobst. Computing optical flow via variational techniques. *SIAM Journal on Applied Mathematics*, 60:156–182, 1999.

S. Banerjee. Turbulence structure and transport mechanisms at interfaces. In *Ninth International Heat Transfer Conference, Keynote Lectures*, volume 1, pages 395–418. Hemisphere Press., 1990.

S. Banerjee, D. Lakehal, and M. Fulgosi. Surface divergence models for scalar exchange between turbulent streams. *International Journal of Multiphase Flow*, 30:963–977, 2004.

S. Banerjee, D. S. Scott, and E. Rhodes. Mass transfer to falling wavy liquid films in turbulent flow. *Industrial & Engineering Chemistry Fundamentals*, 7:22–27, 1968.

M. L. Banner and W. L. Peirson. Tangential stress beneath wind-driven airwater interfaces. *J. Fluid Mech.*, 364:115–145, 1998.

M. L. Banner and O. M. Phillips. On the incipient breaking of small-scale waves. *J. Fluid Mech.*, 65:647–656, 1974.

S. E. Belcher, A. L. M. Grant, K. E. Hanley, B. Fox-Kemper, L. Van Roekel, P. P. Sullivan, W. G. Large, A. Brown, A. Hines, D. Calvert, A. Rutgersson, H. Pettersson, J.-R. Bidlot, P. A. E. M. Janssen, and J. A. Polton. A global perspective on Langmuir turbulence in the ocean surface boundary layer. *Geophys. Res. Lett.*, 39(18):L18605, 2012.

M. J. Black and A. D. Jepson. Estimating optical flow in segmented images using variable-order parametric models with local deformations. *Pattern Analysis and Machine Intelligence*, 18(10):972–986, 1996.

M. Bopp. Messung der Schubspannungsgeschwindigkeit am Heidelberger Aeolotron mittels der Impulsbilanzmethode. Master's thesis, University of Heidelberg, 2011.

M. Bopp. Luft- und wasserseitige strömungsverhältnisse im ringförmigen heidelberger wind-wellen-kanal (aeolotron). Masterarbeit, Institut für Umwelphysik, Univeristät Heidelberg, Germany, 2014.

L. Breimann. Random forests. *Machine Learning*, 45:5–32, 2001.

T. Brox. *From pixels to regions: partial differential equations in image analysis*. PhD thesis, Faculty of Mathematics and Computer Science, Saarland University, Germany, 2005.

T. Brox, A. Bruhn, N. Papenberg, and J. Weickert. High accuracy optical flow estimation based on a theory for warping. In T. Pajdla and J. Matas, editors, *Proc. of the 8th ECCV*, volume 3024, pages 25–36, 2004.

A. Bruhn, J. Weickert, and Schnörr. Lucas/Kanade meets Horn/Schunck: Combining local and global optic flow methods. *International Journal of Computer Vision*, 61(3):211–231, 2005.

B. Buxton and H. Buxton. Computation of optic flow from the motion of edges in image sequences. *Image and Vision Computing*, 2:59–75, 1984.

C. Cassisa. Local vs global energy minimization methods: application to stereo matching. In *Progress in Informatics and Computing*, 2010.

G. Caulliez. The generation of the first visible wind waves. *Physics of Fluids*, 10(4):757–759, 1998.

G. Caulliez, R. Dupont, and V. Shrira. Turbulence generation in the wind-driven subsurface water flow. In C. S. Garbe, R. A. Handler, and B. Jähne, editors, *Transport at the Air Sea Interface — Measurements, Models and Parameterizations*, chapter 7, pages 103–117. Springer-Verlag, 2007.

S. I. Chernyshenko and M. F. Baig. The mechanism of streak formation in near-wall turbulence. *J. Fluid Mech.*, 544:99–131, 2005.

C. Chickadel, S. A. Talke, A. R. Horner-Devine, and A. T. Jessup. Infrared-based measurements of velocity, turbulent kinetic energy, and dissipation at the water surface in a tidal river. *Geoscience and Remote Sensing Letters*, 8(5):849–853, 2011.

G. P. Chini. Strongly nonlinear Langmuir circulation and Rayleigh-Bénard convection. *J. Fluid Mech.*, 614:39–65, 2008.

T. Corpetti, D. Heitz, G. Arroyo, E. Memin, and A. Santa-Cruz. Fluid experimental flow estimation based on an optical-flow scheme. *Experiments in fluids*, 40(1):80–97, 2006.

T. Corpetti, M. Etienne, and P. Perez. Dense estimation of fluid flows. *IEEE Transactions on Pattern Analysis and Machine Intelligence*, 24(3), 2002.

P. M. Cox, R. A. Betts, C. D. Jones, S. A. Spall, and I. J. Totterdell. Acceleration of global warming due to carbon-cycle feedbacks in a coupled climate model. *Nature*, 408(6809):184–187, 2000.

A. D. D. Craik and S. Leibovich. A rational model for Langmuir circulations. *J. Fluid Mech.*, Volume 73:401–426, 1976.

A. Criminisi, J. Shotton, and E. Konukogl. Decision forests: A unified framework for classification, regression, density estimation, manifold learning and semi-supervised learning. *Foundations and Trends in Computer Graphics and Vision*, 7(2–3):81–227, 2012.

G. T. Csanady. Momentum flux in breaking wavelets. *J. Geophysical Research-Oceans*, 95: 13289–13299, 1990.

P. V. Danckwerts. Significance of a liquid-film coefficients in gas absorption. *Ind. Eng. Chem.*, 43:1460–1467, 1951.

R. G. Dean. *Water Wave Mechanics for Engineers and Scientists*. World Scientific, Singapore, 1991.

D. Eisenhauer. Aufbau eines Messsystems zur Amplitudenmessung von Schwerewellen im Aeolotron. Master's thesis, University of Heidelberg, 2011.

R. A. Feely, C. L. Sabine, K. Lee, W. Berelson, J. Kleypas, V. J. Fabry, and F. J. Millero. Impact of anthropogenic CO2 on the CaCO3 system in the oceans. *Science*, 305(5682):362–366, 2004.

J. M. Fitzpatrick. The existence of geometrical density-image transformations corresponding to object motion. *Computer Vision, Graphics, and Image Processing*, 44(2):155–174, 1988.

D. J. Fleet and A. D. Jepson. Computation of component image velocity from local phase information. *International Journal of Computer Vision*, 5(1):77–104, 1990.

G. E. Fortescue and J. R. A. Pearson. On gas absorption into a turbulent liquid. *Chemical Engineering Science*, 22:1163–1176, 1967.

N. Frew, E. Bock, U. Schimpf, T. Hara, H. Haussecker, J. Edson, W. McGillis, R. Nelson, S. McKenna, B. Uz, and B. Jähne. Air-sea gas transfer: Its dependence on wind stress, small-scale roughness, and surface films. *Journal Of Geophysical Research-Oceans*, 109:C08S17, 2004.

T. Fujita and H. Grandoso. Split of a thunderstorm into anticyclonic and cyclonic storms and their motion as determined from numerical model experiments. *Journal of the Atmospheric Sciences*, 25(3):416–439, 1968.

C. S. Garbe. *Measuring Heat Exchange Processes at the Air–Water Interface from Thermographic Image Sequence Analysis*. Dissertation, IWR, Fakultät für Physik und Astronomie, Univ. Heidelberg, Heidelberg, Germany, 2001.

C. S. Garbe, H. Haussecker, and B. Jähne. Measuring the sea surface heat flux and probability distribution of surface renewal events. In E. Saltzman, M. Donelan, W. Drennan, and R. Wanninkhof, editors, *Gas Transfer at Water Surfaces*, volume 127 of *Geophysical Monograph*, pages 109–114. American Geophysical Union, 2002.

C. S. Garbe, U. Schimpf, and B. Jähne. A surface renewal model to analyze infrared image sequences of the ocean surface for the study of air-sea heat and gas exchange. *Journal of Geophysical Research-Oceans*, 109(C8):1–18, 2004.

C. S. Garbe, A. Rutgersson, J. Boutin, B. Delille, C. W. Fairall, N. Gruber, J. Hare, D. Ho, M. Johnson, G. de Leeuw, P. Nightingale, H. Pettersson, J. Piskozub, E. Sahlee, W. Tsai, B. Ward, D. K. Woolf, and C. Zappa. Transfer across the air-sea interface. In P. S. Liss and M. T. Johnson, editors, *Ocean-Atmosphere Interactions of Gases and Particles*, pages 55–112. Springer, 2014.

J. Gemmrich and L. Hasse. Small-scale surface streaming under natural conditions as effective in air-sea gas exchange. *Tellus*, 44B:150–159, 1992.

H. Grassl. The dependence of the measured cool skin of the ocean on wind stress and total heat flux. *Boundary-Layer Meteorology*, 10:465–474, 1976.

M. Gutsche. Surface velocity measurements at the aeolotron by means of active thermography. Master's thesis, Universität Heidelberg, 2014.

R. A. Handler and Q. Zhang. Direct numerical simulations of a sheared interface at low wind speeds with applications to infrared remote sensing. *Selected Topics in Applied Earth Observations and Remote Sensing, IEEE*, 6(3):1086–1091, 2013.

R. A. Handler, G. B. Smith, and R. I. Leighton. The thermal structure of an air–water interface at low wind speeds. volume 53, pages 233–244. 2001.

R. A. Handler, I. Savelyev, and M. Lindsay. Infrared imagery of streak formation in a breaking wave. *Physics of Fluids*, 24:121701, 2012.

R. A. Handler and G. B. Smith. Statistics of the temperature and its derivatives at the surface of a wind-driven air-water interface. *Journal of Geophysical Research*, 116:C06021, 2011.

T. Hara, E. VanInwegen, J. Wendelbo, C. S. Garbe, U. Schimpf, B. Jähne, and N. Frew. Estimation of air-sea gas and heat fluxes from infrared imagery based on near surface turbulence models. In C. S. Garbe, R. A. Handler, and B. Jähne, editors, *Transport at the Air Sea Interface — Measurements, Models and Parameterizations*. Springer-Verlag, 2007.

T. Hastie, R. Tibshirani, and J. Friedman. *The Elements of Statistical Learning*. Springer, 2009.

H. Haussecker, S. Reinelt, and B. Jähne. Heat as a proxy tracer for gas exchange measurements in the field: principles and technical realization. In B. Jähne and E. C. Monahan, editors, *Air–Water Gas Transfer: Selected Papers from the Third International Symposium on Air–Water Gas Transfer*, pages 405–413, Heidelberg, 1995. AEON Verlag & Studio Hanau.

H. Haussecker, U. Schimpf, C. S. Garbe, and B. Jähne. Physics from IR image sequences: Quantitative analysis of transport models and parameters of air-sea gas transfer. In E. Saltzman, M. Donelan, W. Drennan, and R. Wanninkhof, editors, *Gas Transfer at Water Surfaces*, volume 127 of *Geophysical Monograph*, pages 103–108. American Geophysical Union, 2002.

H. W. Haussecker and D. J. Fleet. Computing optical flow with physical models of brightness variation. *Pattern Analysis and Machine Intelligence*, 23(6):661–673, 2001.

H. Haussecker and H. Spies. Motion. In B. Jähne, P. Geissler, and H. Haussecker, editors, *Handbook of Computer Vision and Applications*, volume 2: Signal Processing and Pattern Recognition, chapter 13, pages 309–396. Academic Press, 1999.

P. Heas, E. Memin, N. Papadakis, and A. Szantai. Layered estimation of atmospheric mesoscale dynamics from satellite imagery. *Geoscience and Remote Sensing*, 45(12):4087–4104, 2007.

I. Herlina and G. H. Jirka. Experiments on gas transfer at the air–water interface induced by oscillating grid turbulence. *J. Fluid. Mech.*, 594:183–208, 2008.

R. Higbie. The rate of absorption of a pure gas into a still liquid during short periods of exposure. *Trans. Am. Inst. Chem. Eng.*, 31:365–389, 1935.

D. T. Ho, R. Wanninkhof, P. Schlosser, D. S. Ullman, D. Hebert, and K. F. Sullivan. Toward a universal relationship between wind speed and gas exchange: Gas transfer velocities measured with 3he/sf6 during the southern ocean gas exchange experiment. *Journal of Geophysical Research*, 116, 2011.

B. K. P. Horn and B. Schunk. Determining optical flow. *Artificial Intelligence*, 17:185–204, 1981.

J. Horn. Hochaufgelöste optische wellenhöhenmessung am aeolotron mit laser-induzierter fluoreszenz. Master's thesis, Bachelorarbeit, Institut für Umweltphysik, Fakultät für Physik und Astronomie, 2013.

H. Hühnerfuss. Basic physicochemical principles of monomolecular sea slicks and crude oil spills. In *Marine Surface Films*, pages 21–35. Springer, 2006.

L.-P. Hung, C. S. Garbe, and W.-T. Tsai. Validation of eddy-renewal model by numerical simulation. In S. Komori, W. McGillis, and R. Krose, editors, *Gas Transfer at Water Surfaces 2010*, pages 165–176. Kyoto Univ. Press, 2011.

J. Hunt, S. Belcher, D. Stretch, S. Sajjadi, and J. Clegg. Turbulence and wave dynamics across gas-liquid interfaces. In *Gas Transfer at Water Surfaces 2010*. Komori, S. and McGillis, W. and Kurose, R., 2011.

IPCC. *IPCC, 2013: Summary for Policymakers, in Climate Change 2013: The Physical Science Basis. Contribution of Working Group I to the Fifth Assessment Report of the Intergovernmental Panel on Climate Change*. Cambridge University Press, Cambridge, United Kingdom and New York, NY, USA., 2013.

B. Jähne. *Digitale Bildverarbeitung*. Springer, 2005.

B. Jähne and H. Haussecker. Air-water gas exchange. *Annu. Rev. Fluid Mech.*, 30:443–468, 1998.

B. Jähne, W. Huber, A. Dutzi, T. Wais, and J. Ilmberger. Wind/wave-tunnel experiments on the schmidt number and wave field dependence of air-water gas exchange. In W. Brutsaert and G. H. Jirka, editors, *Gas transfer at water surfaces*, pages 303–309, Hingham, MA, 1984. Reidel.

B. Jähne, P. Libner, R. Fischer, T. Billen, and E. J. Plate. Investigating the transfer process across the free aqueous boundary layer by the controlled flux method. *Tellus*, 41B(2):177–195, 1989.

A. T. Jessup and K. R. Phadnis. Measurement of the geometric and kinematic properties of microscale breaking waves from infrared imagery using a piv algorithm. *Measurement Science and Technology*, 16(10):1961 ff, 2005.

A. T. Jessup, C. J. Zappa, et al. Infrared remote sensing of breaking waves. *Nature*, 385:52–55, 1997.

D. Kiefhaber. *Optical Measurement of Short Wind Waves — from the Laboratory to the Field.* Dissertation, Institut für Umweltphysik, Fakultät für Physik und Astronomie, Univ. Heidelberg, 2014.

S. A. Kitaigorodskii. On the fluid dynamical theory of turbulent gas transfer across an air-sea interface in the presence of breaking wind-waves. *Journal of Physical Oceanography*, 14: 960–972, 1984.

A. N. Kolmogorov. The local structure of turbulence in compressible turbulence for very large Reynolds numbers. *Compt.Rend.Akad.Nauk SSSR*, 30:301, 1941.

S. Komori, Y. Murakami, and H. Ueda. The relationship between surface-renewal and bursting motions in an open-channel flow. *Journal of Fluid Mechanics*, 203:103–123, 1989.

K. E. Krall. *Laboratory Investigations of Air-Sea Gas Transfer under a Wide Range of Water Surface Conditions.* Dissertation, Institut für Umweltphysik, Fakultät für Physik und Astronomie, Univ. Heidelberg, 2013.

C. Kräuter, D. Trofimova, D. Kiefhaber, N. Krah, and B. Jähne. High resolution 2-d fluorescence imaging of the mass boundary layer thickness at free water surfaces. *J. Europ. Opt. Soc. Rap. Public.*, 9:14016, 2014.

C. Kräuter. Aufteilung des transferwiderstands zwischen luft und wasser beim austausch flüchtiger substanzen mittlerer löslichkeit zwischen ozean und atmosphäre. Diplomarbeit, Institut für Umweltphysik, Fakultät für Physik und Astronomie, Univ. Heidelberg, 2011.

V. N. Kudryavtsev and A. V. Soloviev. On the thermal state of the ocean surface. *Izvestiya / Atmospheric and Oceanic Physics*, 17:1065–1071, 1981.

T. Kukulka, A. Plueddemann, J. Trowbridge, and S. P.P. Significance of langmuir circulation in upper ocean mixing: Comparison of observations and simulations. *Geophysical Research Letters*, 36:L10603, 2009.

P. K. Kundu. *Fluid Mechanics.* Academic Press, Elsevier, San Diego, CA, 4th edition, 2008.

J. C. Lamont and J. C. Scott. An eddy cell model of mass transfer into the surface of a turbulent liquid. *AIChE Journal*, 16:513–519, 1970.

Langmuir. Surface motion of water induced by wind. *Science*, 87:119–124, 1938.

C. Le Quéré, C. Rodenbeck, E. Buitenhuis, T. Conway, R. Langenfelds, A. Gomez, C. Labsuchagne, M. Ramonet, T. Nakazawa, N. Metzl, N. Gillett, and M. Heimann. Saturation of the southern ocean CO2 sink due to recent climate change. *Science*, 316(5832):1735–1738, 2007.

C. Le Quéré, G. P. Peters, R. J. Andres, R. M. Andrew, T. A. Boden, P. Ciais, and S. ... Zaehle. Global carbon budget 2013. *Earth System Science Data*, 6(1):235–263, 2014.

J. A. Leese, C. S. Novak, and B. B. Clark. An automated technique for obtaining cloud motion from geosynchronous satellite data using cross correlation. *Journal of applied meteorology*, 10(1):118–132, 1971.

S. Leibovich. The form and dynamics of Langmuir circulations. *Annual Review Fluid Mechanics*, 15:391–427, 1983.

S. Leibovich and S. Paolucci. The instability of the ocean to Langmuir circulations. *J. Fluid Mech.*, 102:141–167, 1981.

M. Li and C. Garret. Mixed layer deepening due to langmuir circulation. *J. Phys. Oceanography*, 27:121–132, 1997.

P. S. Liss and P. G. Slater. Flux of gases across the air-sea interface. *Nature*, 247:181–184, 1974.

P. S. Liss, C. A. Marandino, E. E. Dahl, D. Helmig, E. J. Hintsa, C. Hughes, M. T. Johnson, R. M. Moore, J. M. C. Plane, B. Quack, H. B. Singh, J. Stefels, R. von Glasow, and J. Williams. Short-lived trace gases in the surface ocean and the atmosphere. In P. S. Liss and M. T. Johnson, editors, *Ocean-Atmosphere Interactions of Gases and Particles*, pages 1–54. Springer, 2014.

P. Liss. Gas transfer: Experiments and geochemical implications. In P. Liss and W. Slinn, editors, *Air-Sea Exchange of Gases and Particles*, pages 241–298. Springer, 1983.

C. Liu, J. Yuen, and A. Torralba. Nonparametric scene parsing: Label transfer via dense scene alignment. In *Computer Vision and Pattern Recognition, 2009.*, 2009.

M. S. Longuet-Higgins. The generation of capillary waves by steep gravity waves. *J. Fluid Mech.*, 16:138–159, 1963.

B. D. Lucas and T. Kanade. An iterative image registration technique with an application to stereo vision. *IJCAI*, 81:674–679, 1981.

J. Lucassen. Longitudinal capillary waves. part 1. - theory. *Transactions of the Faraday Society*, 64:2221–2229, 1968.

G. Marmorino, G. Smith, and G. Lindemann. Infrared imagery of large-aspect-ratio langmuir circulation. *Continental Shelf Research*, 25:1–6, 2005.

G. Marmorino, J. Toporkov, G. Smith, M. Sletten, D. Perkovic, K. Frasier, and K. Judd. Ocean mixed-layer depth and current variation estimated from imagery of surfactant streaks. *IEEE Geoscience remote sensing*, 4:364–367, 2007.

G. Marmorino, G. Smith, J. Toporkov, M. Sletten, D. Perkovic, and S. Frasier. Airborne imagery of ocean mixed-layer convective patterns. *Deep-Sea Research*, 56:435–441, 2009.

M. J. McCready, E. Vassiliadou, and T. J. Hanratty. Computer simulation of turbulent mass transfer at a mobile interface. *AIChE Journal*, 32:1108–1115, 1986.

S. P. McKenna and W. R. McGillis. The role of free-surface turbulence and surfactants in air-water gas transfer. *Int. J. Heat Mass Transfer*, 47:539–553, 2004.

W. K. Melville, R. Shear, and F. Veron. Laboratory measurements of the generation and evolution of Langmuir circulations. *J. Fluid Mech.*, 364:31–58, 1998.

E. Mémin and P. Perez. Robust discontinuity-preserving model for estimating optical flow. In *Pattern Recognition, International Conference*, 1996.

W. P. Menzel. Cloud tracking with satellite imagery: From the pioneering work of ted fujita to the present. *Bulletin of the American Meteorological Society*, 82(1):33–47, 2001.

M. Mizuno. Effects of the mechanical wave propagating in the wind direction on currents and stress across the air-water interface. In *Gas Transfer at Water Surfaces 2010*. Kyoto University Press, 2011.

L. Nagel, K. E. Krall, and J. B. Comparative heat and gas exchange measurements in the heidelberg aeolotron, a large annular wind-wave tank. *Ocean Sci. Discuss.*, 11:1691–1718, 2014.

H. Nakagawa and I. Nezu. Structure of space-time correlation of bursting phenomena in an open-channel flow. *J. Fluid Mech.*, 104:1–43, 1981.

J. C. Orr, V. J. Fabry, O. Aumont, L. Bopp, S. C. Doney, R. A. Feely, and A. ... Yool. Anthropogenic ocean acidification over the twenty-first century and its impact on calcifying organisms. *Nature*, 437(7059):681–686, 2005.

N. Papenberg, A. Bruhn, T. Brox, S. Didas, and J. Weickert. Highly accurate optic flow computation with theoretically justified warping. *International Journal of Computer Vision*, 67(2): 141–158, 2006.

W. L. Peirson. Measurement of surface velocities and shears at a wavy air-water interface using particle image velocimetry. *Exp. Fluids*, 23:427–437, 1997.

W. L. Peirson and M. L. Banner. Aqueous surface layer flows induced by microscale breaking wind waves. *J. Fluid Mech.*, 479:1–38, 2003.

W. L. Peirson and A. W. Garcia. On the wind-induced growth of slow water waves of finite steepness. *Journal of Fluid Mechanics*, 608(-1):243–274, 2008.

W. Peirson, J. W. Walker, and B. M. L. On the microphysical behaviour of wind-forced water surfaces and consequent re-aeration . *Journal of Fluid Mechanics*, 743:pp 399–447, 2014.

C. J. Popp. *Untersuchung von Austauschprozessen an der Wasseroberfläche aus Infrarot-Bildsequenzen mittels frequenzmodulierter Wärmeeinstrahlung.* Dissertation, Institut für Umweltphysik, Fakultät für Physik und Astronomie, Univ. Heidelberg, 2006.

L. Prandtl. *Führer druch die Strömungslehre.* Vieweg, 9 edition, 1990.

M. Raffel, C. E. Willert, S. T. Wereley, and J. Kompenhans. *Physical and Technical Background.* Springer, 2007.

M. Rashidi and S. Banerjee. The effect of boundary conditions and shear rate on streak formation and breakdown in turbulent channel flows. *Phys. Fluids*, 2:1827–1838, 1990.

M. Rashidi, G. Hetsroni, and S. Banerjee. Particle-turbulence interaction in a boundary layer. *International Journal of Multiphase Flow*, 16(6):935–949, 1990.

R. Rocholz, S. Wanner, U. Schimpf, and B. Jähne. Combined visualization of wind waves and water surface temperature. In *Gas Transfer at Water Surfaces 2010.* Kyoto University Press, 2011.

W. Roedel. *Physik unserer Umwelt: die Atmosphäre.* Springer-Verlag, 3 edition, 2000.

M. Salter, R. Upstill-Goddard, P. Nightingale, S. Archer, B. Blomquist, D. Ho, B. Huebert, P. Schlosser, and M. Yang. Impact of an artificial surfactant release on air-sea gas fluxes during deep ocean gas exchange experiment ii. *J. Geophysical Research*, 116:1–9, 2011.

M. Sanjou, I. Nezu, and Y. Akiya. PIV measurements of Langmuir circulation generated by wind-induced water waves. In *Gas Transfer at Water Surfaces 2010.* Kyoto University Press, 2011.

U. Schimpf. *Untersuchung des Gasaustausches und der Mikroturbulenz an der Meeresoberfläche mittels Thermographie.* Dissertation, Institut für Umweltphysik, Fakultät für Physik und Astronomie, Univ. Heidelberg, Heidelberg, Germany, 2000.

U. Schimpf, H. Haussecker, and B. Jähne. Studies of air-sea gas transfer and micro turbulence at the ocean surface using passive thermography. In M. L. Banner, editor, *The Wind-Driven Air-Sea Interface: Electromagnetic and Acoustic Sensing, Wave Dynamics and Turbulent Fluxes*, Sydney, Australia, 1999a.

U. Schimpf, C. Garbe, and B. Jähne. Investigation of transport processes across the sea surface microlayer by infrared imagery. *J. Geophysical Research*, 109(C8):C08S13, 2004.

U. Schimpf, H. Haussecker, and B. Jähne. Thermography for small-scale air-sea interaction. In B. Jähne, P. Geissler, and H. Haussecker, editors, *Handbook of Computer Vision and Applications*, volume 3: Systems and Applications, chapter 35, pages 751–762. Academic Press, 1999b.

J. Schnieders. Investigation of momentum transfer across the air-sea interface by means of active and passive thermography. Master's thesis, University of Heidelberg, 2011.

J. Schnieders, C. S. Garbe, W. L. Peirson, G. Smith, and Z. C. J. Analyzing the footprints of near-surface aqueous turbulence: An image processing-based approach. *J. Geophysical Research*, 118:1–15, 2013.

J. Schnieders, C. S. Garbe, and B. Jäehne. Estimating heat transfer rates from surface eddies - the impact of turbulent scales on heat transfer. In preparation, 2014.

J. C. Scott. An optical probe for measuring water wave slopes. *Journal of Physics E Scientific Instruments*, 7:747–749, 1974.

N. V. Scott, H. R.A., and G. B. Smith. Wavelet analysis of the surface temperature field at an air-water interface subject to moderate wind stress. *Int. J. Heat and Fluid Flow*, 29:1103 –1112, 2008.

K. Siddiqui and M. Loewen. Characteristics of the wind drift layer and microscale breaking waves. *Journal of Fluid Mechanics*, 573:417–456, 2007.

C. R. Smith and S. Metzler. The characteristics of low-speed streaks in the near-wall region of a turbulent boundary layer. *J. Fluid Mech.*, 129:27–54, 1983.

G. B. Smith, R. A. Handler, and N. Scott. Observations of the structure of the surface temperature field at an air-water interface for stable and unstable cases. In C. S. Garbe, R. A. Handler, and B. Jähne, editors, *Transport at the Air Sea Interface — Measurements, Models and Parameterizations*. Springer-Verlag, 2007.

J. A. Smith. Doppler sonar and surface waves: Range and resolution. *J. Atmos. Oceanic Technol.*, 9:49–163, 1989.

. SOLAS Scientific Steering Committee, International Project Office. "solas extension proposalâ, international project office, 2015, 2015.

A. Soloviev, S. Matt, M. Gilman, H. Hühnerfuss, B. Haus, D. Jeong, I. Savelyev, and M. Donelan. Modification of turbulence at the air-sea interface due to the presence of surfactants and implications for gas exchange. Part I: Laboratory experiment. In *Gas Transfer at Water Surfaces 2010*. Kyoto University Press, 2011.

A. V. Soloviev and P. Schlüssel. Parameterization of the cool skin of the ocean and of the air–ocean gas transfer on the basis of modelling surface renewal. *J. Phys. Oceanogr.*, 24: 1339–1346, 1994.

A. V. Soloviev and P. Schlüssel. Evolution of cool skin and direct air-sea gas transfer coefficient during daytime. *Boundary-Layer Meteorology*, 77:45–68, 1996.

C. Sommer, C. Straehle, U. Koethe, and F. A. Hamprecht. ilastik: Interactive learning and segmentation toolkit. In *8th IEEE International Symposium on Biomedical Imaging (ISBI 2011)*, 2011.

F. Steinbrucker, T. Pock, and D. Cremers. Large displacement optical flow computation withoutwarping. *12th International Conference on Computer Vision*, pages 1609–1614, 2009.

G. G. Stokes. On the theory of oscillatory waves. *Trans. Camb. Philos. Soc.*, 8:441–455, 1847.

D. Sun, S. Roth, J. P. Lewis, and M. J. Black. Learning optical flow. In *Computer Vision-ECCV 2008*, pages 83–97. Springer Berlin Heidelberg., 2008.

D. Sun, S. Roth, and M. J. Black. Secrets of optical flow estimation and their principles. In *Conference on Computer Vision and Pattern Recognition (CVPR), 2010*, 2010.

D. Suter. Motion estimation and vector splines. In *Proceedings of the IEEE Computer Society Conference on Computer Vision and Pattern Recognition*, pages 939–942, 1994.

S. A. Thorpe. Langmuir circulation. *Annu. Rev. Fluid Mech.*, 79:36–55, 2004.

S. A. Thorpe. *An Introduction to Ocean Turbulence.* Cambridge, UK: Cambridge University Press., 2007.

C. Tropea, A. L. Yarin, and J. F. Foss. *Springer handbook of experimental fluid mechanics.* Springer, 2007.

W.-T. Tsai. Using numerical simulation to help understand transport processes at the air-sea interface, 2007.

W.-T. Tsai, S.-M. Chen, and C.-H. Moeng. A numerical study on the evolution and structure of a stress-driven free-surface turbulent shear flow. *J. Fluid Mech.*, 545:163–192, 2005.

W.-T. Tsai, S.-M. Chen, G.-H. Lu, and C. Garbe. Characteristics of interfacial signatures on a wind-driven gravity-capillary wave. *J. Geophys. Res.*, 118:1715–1735, 2013.

D. E. Turney and S. Banerjee. Air-water gas transfer and near-surface motions. *J. Fluid Mech.*, 733:588–624, 2013.

D. E. Turney, W. C. Smith, and S. Banerjee. A measure of near-surface fluid motions that predicts air-water gas transfer in a wide range of conditions. *Geophys. Res. Lett.*, 32(4): L04607, 2005.

F. Veron and K. Melville. Experiments on the stability and transition of wind-driven water surfaces. *J. Fluid Mech.*, 446:25–65, 2001.

F. Veron, W. K. Melville, and L. Lenain. The effects of small-scale turbulence on air-sea heat flux. *Journal of Physical Oceanography*, 41(1):205–220, 2011.

F. Veron, W. K. Melville, and L. Lenain. Wave-coherent air-sea heat flux. *Journal of Physical Oceanography*, 38(4):788–802, 2008.

R. Wanninkhof. Relationship between wind speed and gas exchange over the ocean. *J. Geophys. Res.*, 97:7373–7382, 1992.

R. Wanninkhof, G.-H. Park, D. B. Chelton, and C. M. Risien. Impact of small-scale variability on air-sea co_2 fluxes. In *Gas Transfer at Water Surfaces 2010*. Kyoto University Press, 2011.

R. Wanninkhof, W. E. Asher, D. T. Ho, C. Sweeney, and W. R. McGillis. Advances in quantifying air-sea gas exchange and environmental forcing. *Annu. Rev. Mar. Sci.*, 1:213–244, 2009.

J. Weickert. *Anisotropic diffusion in image processing*. Stuttgart: Teubner, 1998.

J. Weickert and C. Schnörr. A theoretical framework for convex regularizers in pde-based computation of image motion. *International Journal of Computer Vision*, 45:245–264, 2001.

W. G. Whitman. The two-film theory of gas absorption. *Chemical and Metallurgical Engineering*, 29(4):146–148, 1923.

J. Wills, S. Agarwal, and S. Belongie. A feature-based approach for dense segmentation and estimation of large disparity motion. *International Journal of Computer Vision*, 68:125–143, 2006.

O. Wurl and J. Obbard. A review of pollutants in the sea-surface microlayer (sml): a unique habitat for marine organisms. *Marine Pollution Bulletin*, 48:1016–1030, 2004.

Z. F. Xu, B. C. Khoo, and K. Carpenter. Mass transfer across the turbulent gas-water interface. *AIChE Journal*, 52(10):3363–3374, 2006.

C. J. Zappa, W. E. Asher, and A. T. Jessup. Microscale wave breaking and air-water gas transfer. *Journal of Geophysical Research-Oceans*, 106(C5):9385–9391, 2001.

C. J. Zappa, W. E. Asher, A. T. Jessup, J. Klinke, and S. R. Long. Effect of microscale wave breaking on air-water gas transfer. In E. Saltzman, M. Donelan, W. Drennan, and R. Wanninkhof, editors, *Gas Transfer at Water Surfaces*, volume 127 of *Geophysical Monograph*, pages 23–29. American Geophysical Union, 2002.

C. J. Zappa, W. E. Asher, and A. T. Jessup. Microbreaking and the enhancement of air-water transfer velocity. *Journal of Geophysical Research-Oceans*, 109:C08S16, 2004.

C. J. Zappa, W. R. McGillis, P. A. Raymond, J. B. Edson, E. J. Hintsa, H. J. Zemmelink, J. W. H. Dacey, and D. T. Ho. Environmental turbulent mixing controls on the air-water gas exchange in marine and aquatic systems. *Geophys. Res. Lett.*, 34:L10601, 2007.

A. Appendix

A.1. Technical Data of used Infrared Cameras

Table A.1.: Employed infrared cameras.

Infrared Camera	Thermo-sensorik, CMT 256	IRcam, Velox 327k
Chip	CMT*, cooled	CMT, cooled
wave length range [μm]	3.4 - 5.1	3.4 - 5
number of pixels	256x256	640x512
pixel pitch [μm]	32	24
maximum framerate [Hz] (full image)	880	207
maximum framerate [Hz] (partial image)	880	820
integration time [s]	0.05 - 12.75	0.01 - 1.2
NETD [mK]	20	20
A/D resolution [bit]	14	14

*CMT: Cadmium-Mercury-Telluride.

A.2. Error analysis, k-estimation

It is difficult to give precise measurement errors for some of the crucial quantities needed to calculate the heat transfer rate k. Part of the uncertainty lies in the accuracy of the model assumptions, for example in the case of the estimated bulk temperature T_b. Moreover, it is not possible to give an absolute error of the velocity estimates based on the optical flow algorithm as the ground truth is unknown. Nevertheless, it is instructive to perform an error propagation analysis to identify most important error sources and get an estimate of expectable errors. Starting from equation 3.7,

$$k = \sqrt{\frac{\pi\kappa}{2}} \cdot \sqrt{\frac{v \, \frac{\Delta T_s}{\Delta x}}{T_b - T_s}}, \tag{A.1}$$

the absolute error Δk of the heat transfer rate k is given by:

$$\Delta k = \left|\frac{\partial k}{\partial T_s}\right| \Delta T_s + \left|\frac{\partial k}{\partial T_b}\right| \Delta T_b + \left|\frac{\partial k}{\partial \Delta x}\right| \Delta\Delta x + \left|\frac{\partial k}{\partial v}\right| \Delta v. \tag{A.2}$$

An exemplary error analysis for one case with a wind speed $u = 3.5$ m/s and estimated heat transfer velocity $k = 0.7$ cm/s for small scale turbulence is shown:

$$\begin{aligned} T_s &= (18.49 \pm 0.02)^\circ\text{C}, & \Delta x &= (0.4 \pm 0.02)\text{cm}, \\ T_b &= (18.88 \pm 0.06)^\circ\text{C}, & v &= (6.7 \pm 0.5)\text{cm/s}, \end{aligned}$$

Here, the error estimate for bulk temperature is derived from the histogram in figure 7.13 and therefore an error of the mean. This does not include possible errors resulting from the accuracy of the conceptual model. However, independent estimates of bulk temperatures from the surface renewal model from a thermometer measuring bulk temperature (see Table 4.2) differed by less than 10 %. The given error for the surface velocity is a worst case error. Accuracy tests of surface velocities with known flow fields have shown the relative error to be much lower. The value for Δx is the mean size of surface eddies, the error corresponds to the spatial resolution.

$$\begin{aligned} \Delta k &\approx 1 \cdot \Delta T_s + 0.06 \cdot \Delta T_b + 0.06 \cdot \Delta\Delta x + 0.003 \cdot \Delta v \\ &\approx \underbrace{0.02}_{\Delta T_s} + \underbrace{0.004}_{\Delta T_b} + \underbrace{0.004}_{\Delta x} + \underbrace{0.001}_{\Delta v} \approx 0.03 \end{aligned}$$

Thus, the most important quantity remains the surface temperature field, even though the deployed infrared camera (IRCAM Velox 327k M) has a very high sensitivity. The estimated error is for a single k estimate and is of the order of 50 %. This is high for a single value but even averaging over a small area leads to a small statistical error (thus errorbars in Figure 10.5 are too small to plot). However, the results depend heavily on the accuracy of model assumptions and systematic errors might be significantly higher than the statistical errors.

Danksagung

Ich möchte mich bei PD Dr. Christoph Garbe bedanken, der mir diese Arbeit ermöglicht hat, für seine Ermutigung, Unterstützung und Beratung und für unzählige Diskussionen und Vorschläge. Herrn Prof. Dr. Kurt Roth möchte ich für seine freundliche Bereitschaft zur Zweitbegutachtung der Arbeit danken, die auch noch in die Weihnachtszeit fällt.

Außerdem gilt mein großer Dank Prof. Dr. Bernd Jähne für die Sicherung der Finanzierung der letzten Phase dieser Arbeit, Diskussionen und Vorschläge und die Möglichkeit Messungen am Wind-Wellen-Kanal durchzufühen. Mein großer Dank gilt dabei allen Mitgliedern der Aeolotron-Gruppe, die mich jederzeit bereitwillig unterstüzt haben. Danke an Dr. Leila Nagel, die stets zur Stelle war um Details zu besprechen und Feedback zu geben und bei einer Messung zu helfen, Christine Kräuter für ein jederzeit offenes Ohr, hilfreiche Diskussionen und einer schönen Zeit bei gemeinsamen Konferenzen, Dr. Günther Balschbach und Dr. Kerstin Krall für die tatkräftige Hilfe bei der Installation der Wärmepumpe sowie allerlei technischer Unterstützung und Max Bopp, Jakob Kunz, Marcel Gutsche und Wolfgang Mischler für die tatkräftige Unterstützung rund um die Messungen am Windkanal.

Vielen Dank allen Menschen im dritten Stock der Speyerer Straße für alle Mittags- und Kaffeepausen. Besonderer Dank gilt Julian Stapf, Tobias Binder und Marcel Gutsche für die schöne Atmosphäre im gemeinsamen Büro. Mein Dank gilt auch Tanja Kohl und Karin Kruljac für die Unterstützung bei administrativen Aufgaben.

Mein besonderer Dank gilt meiner Mutter Margret und Tomma, die immer an mich geglaubt haben, mir Mut gemacht haben und jederzeit für mich da waren und sich große Mühe gegeben haben mein Promotionsthema korrekt erklären zu lernen. Besonders möchte ich Andreas danken für die vielen schönen Stunden, seine Geduld und Unterstützung, während der ganzen Zeit und besonders in den letzten Wochen und am allermeisten für seine Liebe.